

# Characterization of II-VI Semiconductor Nanostructures by Low Wavenumber Raman- and Four-Wave-Mixing Spectroscopy

## Dissertation

zur Erlangung des  
naturwissenschaftlichen Doktorgrades  
der Bayerischen Julius-Maximilians-Universität Würzburg

vorgelegt von

**Krisztina Babocsi**

aus

Tasnad, Rumänien

Würzburg 2005

Eingereicht am: .....

bei der Fakultät für Chemie und Farmazie

1. Gutachter: .....

2. Gutachter: .....

der Dissertation

1. Prüfer: .....

2. Prüfer: .....

3. Prüfer: .....

des Öffentlichen Promotionskolloquiums

Tag des Öffentlichen Promotionskolloquiums:.....

Doktorurkunde ausgehändigt am: .....

*To my Family*



# *Abstract*

*This work focuses on the study of optical and electronic properties of quantum confined semiconductor nanocrystals. A full characterization of quasi-zero dimensional semiconductor nanoparticles embedded in a glass matrix is well achieved by applying both linear and nonlinear spectroscopy techniques. Low wavenumber Raman spectroscopy has been proved to be an appropriate tool to determine the most important parameters like the size of the nanocrystals and the nanoparticle's size distribution inside the dielectric matrix. Moreover, the chemical composition of the nanocrystals was obtained applying resonance Raman techniques. Further properties of such quantum confined systems related to the electronic structure, the nanocrystals' symmetry and its dependence on the crystal growth conditions were successfully determined by means of four-wave-mixing and pump-probe spectroscopy. Four-wave-mixing in the framework of transient grating experiments was applied in order to complete the picture of complex relaxation processes in quantum confined systems.*



# Contents

<b>1</b>	<b>Introduction</b>	<b>1</b>
<b>2</b>	<b>Semiconductors: Basic Concepts</b>	<b>7</b>
2.1	Growth Processes . . . . .	8
2.2	Crystallographic Structure of II-VI Semiconductor Quantum Dots . .	8
2.3	Energy States . . . . .	12
2.3.1	One Electron-Hole Pair States . . . . .	12
2.3.2	Two Electron-Hole Pairs . . . . .	19
2.3.3	Interaction of Many Particles . . . . .	22
<b>3</b>	<b>Low Wavenumber Raman Spectroscopy on CdSSe Quantum Dots</b>	<b>25</b>
<b>4</b>	<b>Four-Wave-Mixing Spectroscopy</b>	<b>37</b>
4.1	Theoretical Model . . . . .	38
4.1.1	Perturbation Theory . . . . .	40
4.1.2	Induced Polarization . . . . .	42
4.2	Femtosecond Spectroscopy . . . . .	43
4.2.1	First Order Polarization . . . . .	44
4.2.2	Second Order Polarization . . . . .	45
4.2.3	Third Order Polarization . . . . .	48
<b>5</b>	<b>Experimental Setup</b>	<b>55</b>
5.1	Femtosecond Laser Pulses: Generation and Characterization . . . . .	56

5.2	Phase Matching Condition . . . . .	61
<b>6</b>	<b>Biexciton and Spin Dephasing Effects</b>	<b>65</b>
6.1	Exciton–Exciton Coupling in CdSSe Quantum Dots . . . . .	66
6.2	Spin Dephasing in 3D Confined Systems . . . . .	77
<b>7</b>	<b>Degree of Asymmetry of Nanoparticles Embedded in Dielectric Matrix</b>	<b>82</b>
7.1	Influence of Growth Conditions . . . . .	83
7.2	Size Dependence of Exciton Lifetime . . . . .	99
7.3	Energy Relaxation Mechanisms from Higher Excited States . . . . .	110
<b>8</b>	<b>Conclusions – Zusammenfassung</b>	<b>119</b>
8.1	Conclusions . . . . .	119
8.2	Zusammenfassung . . . . .	126
	<b>Bibliography</b>	<b>133</b>
<b>9</b>	<b>Acknowledgements</b>	<b>143</b>



# Abbreviations and Symbols

DFWM	degenerate four-wave-mixing
DTS	differential transmission signal
e-h	electron-hole
EHP	electron-hole pair
EMA	effective mass approximation
eq.	equation
fs	femtosecond
FWHM	full width half maximum
FWM	four-wave-mixing
HH	heavy hole
IR	infra red
LH	light hole
LCAO	linear combination of atomic orbitals
NIO	non-interacting oscillators
PL	photoluminescence
PPT	pump-probe transmission
ps	picosecond

## Abbreviations

---

QD	quantum dot
QW	quantum well
SO	spin-orbit
TI-FWM	time-integrated four-wave-mixing
TR-FWM	time-resolved four-wave-mixing
VWM	vier-Wellen-Mischung
X	exciton
X-X	biexciton
ZI-VWM	Zeitintegrierte vier-Wellen-Mischung
$\mu\text{s}$	microsecond

# 1 Introduction

Bulk crystalline semiconductors started a new era in the development of science and technology. Their optical and electronic properties constitute the basis of an entire industry including electronics, telecommunications, microprocessors, computers and many other components of modern technology. Further innovation was brought by reducing the semiconductor's spatial dimensions, leading to huge enhancement in their optical nonlinearities due to confinement of carriers. Industry requirement for miniaturization demanded artificial preparation of quantum wells (QW) and quantum wires with carriers confined in one and two directions of the cartesian space, respectively, encouraging further efforts of scientist to reduce the dimensions even more. Confinement of carriers in all 3 spatial dimensions was achieved in the semiconductor quantum dots (QDs). The spatial extension of semiconductor QDs ranges on a nanometer scale and is comparable to the exciton Bohr radius of the bulk.

Such nanocrystals with electrons and holes confined in all three spatial dimensions raised high interest in the last decade [1–6] and show a wide application range from spintronics to quantum computation [7] based on the ability to control and maintain spin coherence over a practical length and time scale. Three dimensionally confined excitons are interesting not only because of their highly enhanced nonlinearities but also because they are known as prototypical systems for investigating the physics of quantum confinement. Semiconductor QDs are considered as a new form of matter,

which due to their discrete energy structure have been called "artificial atoms" and can be manipulated to create QD molecules or can be used as dopants in order to form a supermolecule. Hence, the periodic table of elements could be extended with "artificial elements".

This work is focused on the study of II-VI QDs embedded in a glass matrix. Nanocrystals formed in inorganic host present the advantage of being impervious to ambient changes up to high temperatures. At the same time one has to confront the disadvantage that such QDs are not accessible to surface modifications, while the main contribution to the optical processes is brought by surface states and associated defects. The presence of the glass matrix does not allow changes in the QD's structure once the growth process is closed. However, the thermodynamical stability of such nanoparticles provides satisfactory applications.

The electronic and optical properties of nanocrystals depend strongly on their spatial dimensions and composition. Thus another way to control the physics of quantum confined systems is achieved by controlling their dimension. This is easily done by appropriate selection of the heat treatment conditions (duration and temperature). Heat treatment of QDs embedded in a dielectric matrix by rapidly quenching from melts yield a wide range of nanocrystal sizes, the precipitation in a very viscous medium affording the control of nucleation rates and growth of colloids.

The samples investigated in this work are commercially available  $CdS_xSe_{1-x}$  QDs embedded in a glass matrix provided by Schott Inc., known as very efficient optical filters. Their cut-off wavelength depends both on the chemical composition (the fraction  $x$  of  $S$  atoms in the nanocrystal) and on the QD's size. In the case of the investigated samples these parameters both vary from one sample to another. Moreover, this study includes not only as-received glasses but also a category of heat treated QDs with the aim to determine the "perfect conditions" to grow high quality QDs.

Linear and nonlinear spectroscopy techniques are applied in order to investigate the physics of these confined systems. The aim of this study is a full characterization

---

of the nanocrystals. It will be shown that linear and nonlinear spectroscopy techniques under adequate polarization geometries are complementary tools and provide invaluable information about the size, chemical composition, shape and asymmetry of the QDs. Moreover, the exciton fine structure and ultrafast relaxation processes will be determined.

The basic concepts of semiconductor nanocrystals are reviewed in chapter 2. In the first part, the growth process and its influence on the crystallographic properties of the QDs are discussed. A brief overview of the fine energy structure of QDs and the confinement induced degeneracy of the energy bands are presented.

The key-parameters of various as-received  $CdS_xSe_{1-x}$  nanocrystals embedded in dielectric matrix are determined in chapter 3. The most efficient non-destructive method suitable for such investigations is the low wavenumber Raman spectroscopy. The special experimental setup enables one to record the spectra very close to the Rayleigh line and therefore evidencing acoustic phonons, which are often masked by strong luminescence and unconformity of the experimental equipment. Special care is taken to the linear polarization of the laser beams, which allows the selection of the acoustic vibrational modes. The low wavenumber Raman technique is applied in off-resonance scattering regime. The off-resonance Raman measurements provided the QD's mean size and the size distribution inside the inhomogeneous broadening.

A complete picture of the QDs presented above can be achieved by applying complementary techniques. Femtosecond four-wave-mixing spectroscopy is successfully applied in the study of ultrafast processes taking place in confined systems. Chapter 4 contains a brief description of a theoretical model based on the treatment of the third order nonlinear polarization in the framework of density matrix formalism. This model is successfully used for an interpretation and description of nonlinear processes in confined ensembles and is completed by a schematic representations of the interaction processes between carriers.

Chapter 5 is entirely dedicated to a detailed description of the experimental setup used to perform the pump-probe transmission (PPT) and the four-wave-mixing

(FWM) experiments, both involving femtosecond (fs) laser pulses. In the first part, the attention is focused on the generation and characterization of femtosecond laser pulses. The setup illustrated in this chapter presents major advantages such as tunability of the wavelength over the whole visible range, individual control of the time sequence of the pulses and ability to choose different beam geometries. Moreover, the polarization of the femtosecond pulses can be individually selected, thus making different dynamical processes accessible.

One of the as-received samples studied in chapter 3, namely OG550 is further investigated by means of ultrafast spectroscopy techniques, the results being summarized in chapter 6. Femtosecond FWM and PPT spectroscopy involving circularly polarized laser pulses are applied in the study of energetic and optical properties of confined excitons. It is shown that the relaxation of polarization selection rules is due to a strong exciton-exciton coupling inside the same QD thus proving the existence of biexciton structures. Another reason for the relaxation of selection rules constitutes the contribution of the inhomogeneous spin dephasing of excitons due to a random exchange splitting of the lowest optically active exciton state  $J = 1$  as consequence of the lowering of the QD symmetry. Therefore the FWM spectroscopy is proven to be an appropriate tool in the investigation of the internal and crystal shape asymmetry of QDs.

This idea is extended in chapter 7, where heat treated CdSe nanocrystals embedded in dielectric matrix are extensively investigated. The attention is focused on the influence of the heat treatment conditions (duration and temperature) on the crystal shape and consequently on the fine energy structure of the nanocrystals. It will be shown that samples containing nanoparticles of the same size, but grown under different conditions (different time intervals and/or temperatures) exhibit different exciton spin dephasing times and thus different symmetry. As a conclusion, a qualitative study of the dependence of the QD's asymmetry on the QD's size and heat treatment duration will be presented.

A major part of this work is dedicated to the exciton relaxation processes in quan-

---

tum dots. In the last part of chapter 7 it will be shown, that the exciton relaxation is a complex mechanism. As a consequence of optical excitation, the electrons and holes can follow different paths in their way back to the ground state. The decay times are ranging on a ps time scale and include both Auger processes and scattering on surface defects. It will be proved that Auger autoionization plays a decisive role in the relaxation of carriers in 3D confined systems. The capture of electrons in deep traps in the dielectric matrix slows down significantly the relaxation process. Chapter 7 also discusses relaxation processes from higher lying exciton states, where Auger-like thermalization, Auger autoionization and capture of carriers in surface traps have to be considered for the study of the excited exciton behavior. Consequently it will be demonstrated that the electron-hole interaction is the decisive factor responsible for the carrier relaxation and that phonon mediated processes are strongly suppressed in quasi zero dimensional particles. Thus the phonon bottleneck, which is a well-known phenomenon in bulk semiconductors is definitely broken in nanoparticle ensembles.

Although there are excellent publications from numerous scientist in this domain [1–6], the physics of quantum confinement is still not entirely understood. This work represents a further step and gives an idea for the direction of improvement in QD's fabrication techniques in order to obtain high quality QDs. It presents the complex relaxation mechanisms of quantum confined carriers on a subatomic scale, thus achieving a description of nonlinear properties of nanosized particles. Moreover, it proves that by application of both linear- (low wavenumber Raman scattering) and nonlinear spectroscopy (fs-FWM) a complete characterization of quantum confined systems can be achieved.





## 2 Semiconductors: Basic Concepts

*Artificially obtained semiconductor structures with reduced dimensions present a large variety of new interesting properties in comparison to the bulk material and open new ways in the engineering of semiconductors. By simple combination of two semiconductor materials of different band-gap energies –quantum well– a spatial confinement of carrier motion in the direction of the growth axis is obtained. Further decrease of dimensions to one-dimensional –quantum wires– and quasi-zero dimensional –quantum dots– structures leads to large enhancement of their optical nonlinearities. Confinement of carriers in all 3 spatial directions consequently involves a redistribution of the energy in well-separated atomic-like energy levels. Moreover, quantum dots are known as prototypes in the physics of quantum confinement.*

*This chapter gives a brief review of the basic properties of II-VI semiconductor nanocrystals. In the first part of this section the growth methods and their influence on the crystallographic and energy structure are described. The lifting of degeneracy due to confinement effects, the one-electron–hole pair and two-electron–hole pair states are discussed.*

## 2.1 Growth Processes

The samples studied in this work are commercially available optical filter glasses provided by *Schott Inc.* The optical properties of such filters are determined by the semiconductor crystals embedded in the matrix.

The crystal diameter and its chemical composition are the most important parameters which determine the spectral position of the absorption edge and therefore the color and the cut-off wavelength of the glass filter. Both crystal dimensions and composition can be controlled during the synthesis process by varying parameters like temperature and/or duration of growth process.

The glass and semiconductor components are melted together at 1250–1400°C in order to obtain a supersaturated solution of semiconductor ions. Very small crystallites are separated from this supersaturated solution and form so called nucleation centers, to whom further semiconductor ions are supposed to migrate during this step of the synthesis. The nucleation process is followed by a diffusion process, taking place at 500–800°C, temperature range lying above the glass transition but below the melting point.

The size of the nanoparticles can be controlled by selecting the appropriate duration of the growth process [8–10]. The size distribution of QDs in the sample is best described by a Gaussian distribution [11, 12].

## 2.2 Crystallographic Structure of II-VI Semiconductor Quantum Dots

In industry, the most frequently used II-VI semiconductor nanostructures are zinc- and cadmium chalcogenides. Such materials present large energy gaps and crystallize in two main structures: the cubic zinc blend and the hexagonal wurtzite structure, both illustrated schematically in figure 2.1.

Both zinc blend and wurtzite structures show tetrahedral coordination, i.e. each

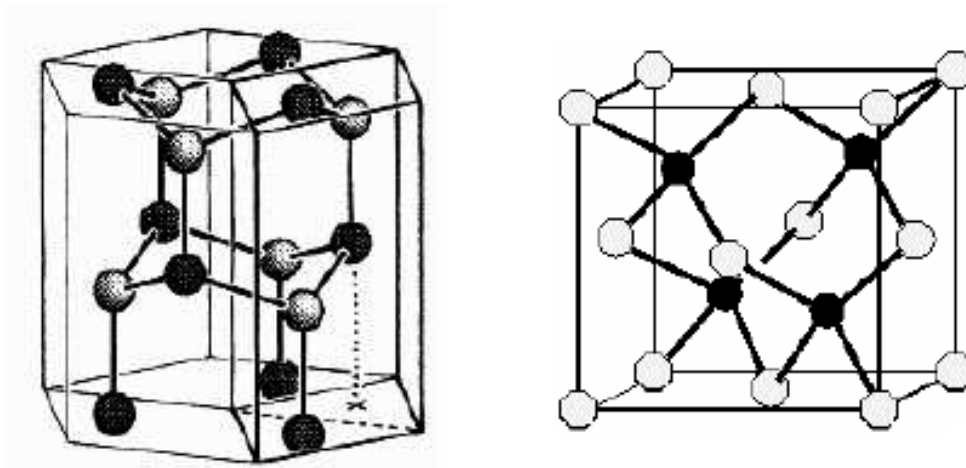


**Fig. 2.1:** The crystallographic structure of II-VI semiconductors. Black spheres are cations and can be Zn, Cd or Hg atoms, whereas white spheres are anions represented by S, Se or Te atoms. On the left: hexagonal wurtzite structure. On the right: cubic zinc blend structure .

Cd atom is surrounded by 4 S, respectively Se atoms and vice versa. The bulk usually crystallizes in wurtzite structure, whereas in the case of nanocrystals these two structures coexist. Their ratio can be controlled through appropriate selection (control of temperature) of growth conditions [13,14]. The symmetry characteristics of the most frequently used QDs are summarized in table 2.1.

Another important parameter for the characterization of the crystallographic structure of II-VI quantum dots is the lattice constant. Table 2.2 contains information about the lattice constants of the two structures described above for the most commonly used bulk semiconductors [13].

The crystallographic structure of mixed semiconductor nanocrystals i.e.  $CdS_xSe_{1-x}$  is also determined by the preparation conditions, depending on the (stable) crystallographic structure of the compounds CdS and CdSe. For this case, parameters like the lattice constant  $a$  or the QD's diameter can be calculated using a linear interpolation of the components (Vegardschen rule).

*Gandais et al.* [15] showed a nicely discernable crystal structure of nanocrystals

**Table 2.1:** Crystallographic Structure of II-VI Semiconductors [13]

	zinc blend	wurtzite
<b>Group of symmetry</b>	$C_6$	$T_d$
<b>Nr. atoms/primitive cell</b>	4	2
<b>Stable structures</b>	ZnS, CdS, CdSe	ZnS, ZnSe, ZnTe, CdTe
<b>Metastable Structure</b>	ZnSe, ZnTe, CdTe	CdS, CdSe

**Table 2.2:** The Lattice Constant  $a$  in  $10^{-10}$  m of II-VI Semiconductors [13]. The numerical values in brackets indicate the lattice constant of the metastable structure.

	wurtzite	zinc blend
<b>ZnSe</b>	(4.01)	5.669
<b>CdS</b>	4.137	(5.838)
<b>CdSe</b>	4.298	(6.084)
<b>CdTe</b>	(4.57)	6.481

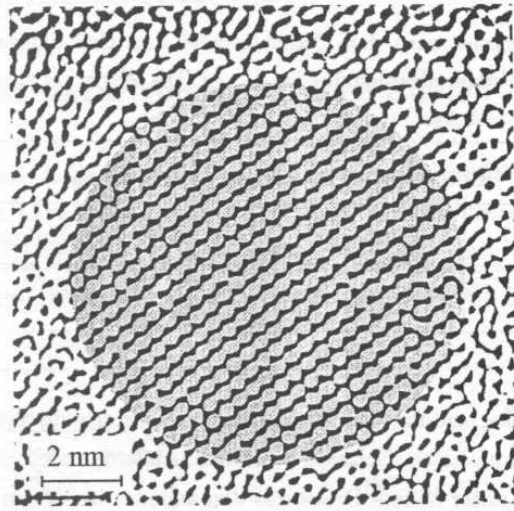


**Fig. 2.2:** HRTEM picture of a single  $CdS_xSe_{1-x}$  QD embedded in a glass matrix [15]. The refraction pattern of the QD is emphasized by grey deposition.

hosted by the commercially available Schott filter glass RG630 (where the number next to the letters stays for the cut-off wavelength of the filter glass). Figure 2.2 displays the picture of a single nanocrystal recorded by high resolution transmission electron microscopy (HRTEM) [15]. The studies on II-VI semiconductor nanostructures by the group of Gandais [15] showed that small crystals present a spherical structure, whereas big crystals ( $> 10$  nm) display a hexagonal prism structure. They also proved that II-VI nanostructures embedded in a glass matrix crystallize mainly in wurtzite structure.

This work contains studies on crystals of low dimensionality with diameters not exceeding 10 nm. Although the spherical form for the case of small particles can be considered as a good approximation, it will be shown in chapters 6 and 7, that small deviations from the spherical symmetry lead to considerable changes in the electronic and optical properties of such nanostructures.

## 2.3 Energy States

The energy band structure forms the basis of understanding the most optical properties of semiconductors. The conditions for a nanocrystal to be considered as a quantum dot are related to their spatial dimensions. Considering the exciton Bohr radius  $a_B$  three different confinement regimes can be distinguished:

1. *weak confinement regime*:  $R > a_B$ ,

The radius  $R$  of the nanocrystals is bigger than the exciton Bohr radius  $a_B$  of the bulk.

2. *intermediate confinement*:  $a_{B,h} < R < a_{B,e}$ ,

In this case the dimension  $R$  of the nanocrystal lies between the Bohr radius of the electrons  $a_{B,e}$  and the Bohr radius of the hole  $a_{B,h}$ .

3. *strong confinement regime*:  $a < R < a_B$ ,

The carriers are strongly confined if their radius  $R$  lies in the interval defined by the lattice constant  $a$  and the exciton Bohr radius  $a_B$  of the bulk.

The three-dimensional quantum confinement of carriers is analogous to the quantum mechanical problem of the motion of a particle in a box with infinitely high potential barriers. In the following, the influence of models going beyond simple quantum mechanics on properties like selection rules, wave functions and energy states themselves is briefly presented.

### 2.3.1 One Electron-Hole Pair States

The samples studied within this work lie in the strong confinement regime defined above. Although the QD's dimensions are smaller than the exciton Bohr radius, they exceed the lattice constant and the crystalline structure of the bulk is preserved. In order to describe the effect of quantum confinement, the effective mass approximation (EMA) [16–18] was proved to be a good approach. The results obtained from

alternative calculation methods as LCAO (linear combination of atomic orbitals) or tight-binding approximation coincide well with the results given by the EMA for nanocrystals showing strong confinement [19–27].

The energy states in semiconductors are given by the semiconductor Bloch equations, which result from the stationary Schrödinger equation of an electron in a spatially periodic potential:

$$\hat{H}\Psi(r) = \left[ -\frac{\hbar^2}{2m}\nabla^2 + V(r) \right] \Psi(r) = E\Psi(r). \quad (2.1)$$

The potential  $V(\vec{r})$  is a periodic potential, with a period equal to that of the underlying Bravais lattice for all lattice vectors  $\vec{R}$ . In the following, the vector signs of the position vector  $\vec{r}$  and  $\vec{R}$  are omitted for simplification.

$$V(r) = V(r + R). \quad (2.2)$$

The eigenstates  $\Psi$  (eq. 2.1) are envelope functions composed of the plane wave  $e^{ikr}$  and the periodical function  $u_{\nu,k}(r)$  having the period of the Bravais lattice and are described by the Bloch theorem:

$$\Psi_{\nu,k}(r) = e^{ikr} u_{\nu,k}(r), \quad (2.3)$$

where

$$u_{\nu,k}(r) = u_{\nu,k}(r + R), \quad (2.4)$$

$\nu$  being the band index and  $k$  the wave vector reduced to the first Brillouin zone.

Thus the energy eigenvalues  $E$  in the effective mass and parabolic band approximation are given by:

$$E(k) = \frac{\hbar^2 k^2}{2m}, \quad (2.5)$$

where  $m$  is the effective mass of the electron or the hole, respectively.

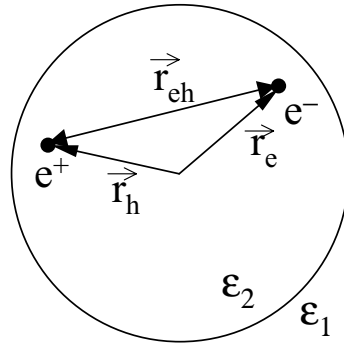


**Fig. 2.3:** The motion of an electron with associated position vector  $\vec{r}_e$  and of the hole with associated position vector  $\vec{r}_h$  inside a sphere with a dielectric constant  $\epsilon_2$ , whereas  $\epsilon_1$  is the dielectric constant of the medium outside the sphere. The sphere with infinite potential barriers symbolizes the QD embedded in a host material with dielectric constant  $\epsilon_1$ .

Considering the electron-hole states inside a spherical QD of a radius  $R$  as being surrounded by an infinitely high potential barrier represented by the dielectric matrix (figure 2.3), the eigenstates  $\Psi$  can be expanded in products of a new envelope function  $\psi$  and the periodic part of the Bloch function  $u_{\nu,k}$ :

$$\Psi(r) = \psi(r)u(r). \quad (2.6)$$

Here, the band index  $\nu$  and the wave vector  $k$  were ignored for simplicity.

Considering parabolic bands and neglecting the Coulomb interaction, the Hamiltonian for the new envelope function  $\psi(r)$  is:

$$\hat{H} = -\frac{\hbar^2}{2m_e} \nabla_e^2 - \frac{\hbar^2}{2m_h} \nabla_h^2 + V_e(r_e) + V_h(r_h) \quad (2.7)$$

with the confinement potential:

$$V_i(r_i) = \begin{cases} 0 & \text{for } r_i < R \\ \infty & \text{for } r_i > R \end{cases}, \quad (2.8)$$

where the indices  $i=e,h$  stay for electron and hole, respectively.



If the interaction between electrons and holes is negligible, the envelope function can be written as a product of separate contributions of the electron and hole, respectively

$$\psi(r_e, r_h) = \phi_e(r_e) \cdot \phi_h(r_h). \quad (2.9)$$

Thus separating the motion of the electron from the motion of the hole, the solution of the Schrödinger equation (eq. 2.7, eq. 2.8 and eq. 2.9) is given by

$$\phi_{nlm}^i(r) = Y_{lm} \sqrt{\frac{2}{R^3}} \frac{J_l(\chi_{nl} \frac{r}{R})}{J_{l+1}(\chi_{nl})}, \quad (2.10)$$

where the quantum numbers  $n = 1, 2, 3, \dots$  (main quantum number),  $l = 0, 1, 2, \dots$  (orbital quantum number) and  $-l \leq m \leq l$  (magnetic quantum number) are introduced.  $Y_{lm}$  are the spherical harmonics and  $J_l$  the spherical Bessel functions. The energy values are calculated taking into account the boundary conditions at the QD-matrix interface  $r = R$ , where the wave function of the particle  $i$  ( $i$  stays for electron and hole, respectively) vanishes:

$$J_l \left( \chi_{nl} \frac{r}{R} \right) \Big|_{R=r} = 0. \quad (2.11)$$

Introducing the values of the spherical Bessel and harmonic functions [28] the energy values are determined as:

$$E_{nl}^{e,h} = \frac{\hbar^2}{2m_{e,h}} \frac{\chi_{nl}^2}{R^2} \quad (2.12)$$

and taking into account the boundary condition eq. 2.11, the lowest energy state in a quantum dot is

$$E_{10}^{e,h} = \frac{\hbar^2}{2m_i} \frac{\pi^2}{R^2}. \quad (2.13)$$

For the lowest confined electron-hole pair (1EHP) state an increase of the transition energy  $\Delta E$  with respect to the bulk band gap is obtained:

$$\Delta E = \frac{\hbar^2 \pi^2}{2\mu R^2}, \quad (2.14)$$

where  $\mu = \frac{m_e m_h}{m_e + m_h}$  is the reduced effective mass of the electron-hole pair.

The Coulomb interaction, which in bulk represents the reason for the existence of excitons, plays an important role in characterizing the electron-hole interaction. The Hamilton operator describing the electron-hole interaction is given by:

$$\hat{H} = -\frac{\hbar^2 \nabla_e^2}{2m_e} - \frac{\hbar^2 \nabla_h^2}{2m_h} - \frac{e^2}{\epsilon_2 |r_e - r_h|} + V_e(r_e) + V_h(r_h). \quad (2.15)$$

The Coulomb potential, which depends on the distance between the electron and the hole, introduces a break in the symmetry and makes the separation of eq. 2.15 in coordinates of relative and center-of-mass motion of the electron-hole pair difficult. By applying the perturbation theory [29], the lowest excited state energy results into:

$$E_{10} = \frac{\hbar^2 \pi^2}{2R^2} \left[ \frac{1}{m_e} + \frac{1}{m_h} \right] - \frac{1.8e^2}{\epsilon_2 R}. \quad (2.16)$$

Further improvements of this model can be obtained considering a realistic semiconductor band structure. For II-VI semiconductors such as CdS, CdSe, ZnSe, etc. and most III-V compounds, the conduction band is determined by  $s$ -orbitals of the metal ion, whereas the valence band has a more complicated structure, originating in  $p$ -orbitals of S, Se or other elements of group VI or V, respectively.

The conduction band can be approximated by parabolic bands with only 2-fold spin degeneracy at  $k = 0$  due to its origin in  $s$ -type orbitals, whereas the non-parabolicity of the valence bands lifts the degeneracy. In figure 2.4 the bulk bands for both zinc-blende and wurtzite-type crystallin structures are shown. In zinc-blende structures belonging to  $T_d$  group symmetry, the  $p$ -type character of the atomic orbitals leads to a six-fold degenerated valence band at  $k = 0$  without taking into account the spin-orbit coupling. The spin-orbit coupling reduces the valence

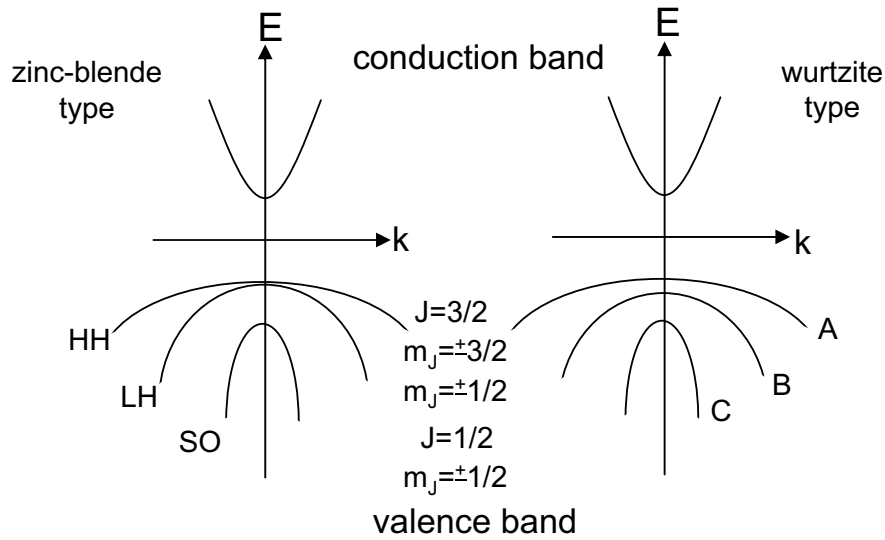


**Fig. 2.4:** Band structure of zinc-blende and wurtzite type semiconductors. Detailed description – see text.

band degeneracy and the band can be described by the total angular momentum  $J$ , representing the sum of the orbital angular momentum and spin angular momentum.

The four-fold degenerate valence band with a total angular momentum  $J = 3/2$  ( $m_J = \pm 3/2; \pm 1/2$ ) and the two-fold degenerate valence band with  $J = 1/2$  ( $m_J = \pm 1/2$ ) are created by the combination of the orbital momentum 1 and the angular momentum  $1/2$  of the spin. The split in energy of these two states with  $J = 3/2$  and  $J = 1/2$  at  $k = 0$  (at  $\Gamma$  point of the Brillouin zone) is determined by the spin-orbit coupling. The concepts of "heavy hole" (HH) and "light hole" (LH) subbands denote the two uppermost valence bands and the term "spin-orbit split-off band" (SO) stays for the lowest valence band.

In wurtzite-type crystals, the crystal field introduces a small perturbation of the  $T_d$  symmetry leading to a lifting in degeneracy at  $k = 0$  of the two uppermost valence bands. The result consists in three valence bands, labelled A, B, and C, respectively.

Analogous to the bulk exciton, the energetically lowest exciton level is an eightfold degenerate ( $1S_{3/2}, 1s_e$ ) electron-hole pair state. The electron is an  $s$ -type electron

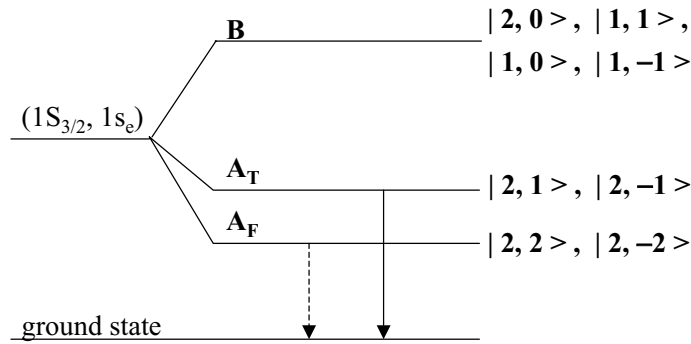


**Fig. 2.5:** Simplified illustration of lifting of degeneracy of the one electron-hole pair state  $(1S_{3/2}, 1s_e)$  due to non-sphericity of QDs, crystal field and exchange interaction. The states are labelled by the corresponding "ket-vectors"  $|N, N_m\rangle$ , composed by the total pair angular momentum  $N$  and its projections  $N_m$  [4].

arising from the lowest conduction band and is characterized only by its spin quantum number  $s = 1/2$  with the projections  $m_s = \pm 1/2$ . The hole, arising from the uppermost valence band is described by the total angular momentum  $F = 3/2$  with the projections  $m_F = \pm 3/2, \pm 1/2$ . Here,  $F = L + J$  is the total angular momentum resulting from the mixing of  $s$  and  $d$ -type valence bands,  $L$  is the orbital angular momentum of the wave function due to confinement effects and  $J$  is the angular momentum of the Bloch component of the wave function [28]. In order to characterize the electron-hole pair state, the total pair angular quantum momentum  $N = F + s$  is introduced [3] with the projections  $N_m$ . The eightfold degeneracy of the lowest exciton state is given by all possible combinations  $|N, N_m\rangle = |F, s, m_F, m_s\rangle$ .

The energetically lowest  $(1S_{3/2}, 1s_e)$  exciton state can be further split due to the crystal field (i.e. wurtzite structure) or deviation from the spherical shape of the QDs [4] into two groups of states, labelled **A** and **B** (figure 2.5). For very small nanocrystals (with a radius smaller than 1.5 nm) showing relevant deviation from the spherical shape, the energy states labelled **B** undergo further significant splitting. For QDs with dimensions exceeding 1.5 nm but still in the strong confinement regime

showing almost-spherical symmetry, the energy levels belonging to group **A** and group **B** are well-separated by tens of meV. The exchange interaction leads to further splitting of the group **A** energy states into two pair-states given by the projections  $N_m = \pm 1$  and  $\pm 2$  of the total pair angular momentum  $N = 2$ . The lowest pair state with  $N_m = \pm 2$  is labelled  $A_F$ , while the immediately higher lying energy state with  $N_m = \pm 1$  is labelled  $A_T$ . Transitions from the ground state to  $A_F$  are forbidden because light with an angular momentum 1 couples to states with  $N_m = \pm 2$  only in higher orders of perturbation theory. Thus the dipole forbidden  $A_F$  state shows only weak absorption, but the emission after relaxation from energetically higher levels is certainly possible. The lowest optically active pair state is  $A_T$  with  $N_m = \pm 1$ , which couples strongly to the radiation field. However, it is important to note that the energetically lowest lying optically active state  $A_T$  is not the energetically lowest lying exciton state, the latter being represented by  $A_F$ . This remark plays a very important role in the understanding of the relaxation processes in confined systems, discussed in the following chapters.

### 2.3.2 Two Electron-Hole Pairs

Excitation of several electron–hole pairs in quantum confined systems leads to interaction of charge carriers. The possible interactions appear between two electrons, two holes, and one electron and one hole, respectively. The corresponding Hamiltonian operator is given by:

$$\hat{H} = \hat{H}_e + \hat{H}_h + V_{ee} + V_{hh} + V_{eh} + \delta V(\epsilon_1, \epsilon_2, r_e, r_h) + V_{e,h}^{conf}, \quad (2.17)$$

where  $\hat{H}_e$  and  $\hat{H}_h$  represent the kinetic energies of electrons and holes, respectively,  $V_{ee}$ ,  $V_{hh}$  and  $V_{eh}$  are the Coulomb interaction terms for the electron–electron, hole–hole and electron–hole interactions with the background dielectric constant of the bulk material,  $\delta V(\epsilon_1, \epsilon_2, r_e, r_h)$  is the correction to the Coulomb potential due to the differences in the dielectric constants of the semiconductor and the glass host, and

$V_{e,h}$  stays for the barrier potential [30,31].

The spatial confinement of excitons involves the mixing of their wave functions. The mixing of wave functions of two excitons close to each other results either in a symmetric or in an anti-symmetric combination. The symmetric combination forms the bound state of the excitonic molecule (biexciton) with lower energy, whereas the anti-symmetric state is not bound.

Bound pair states can be created only if the Coulomb interaction between carriers is taken into account. Ignoring the Coulomb potential, from eq. 2.17 degenerate one- and two-pair states are obtained and the binding energy results to be zero  $\delta E_2 = 0$ . The stability of the two-electron-hole-pair states is given by a positive binding energy:

$$\delta E_2 = 2E_1 - E_2, \quad (2.18)$$

where  $E_1$  and  $E_2$  are the ground state energies corresponding to the one- and two-pair states, respectively. In QDs however,  $E_2$  is not a correct eigenenergy, the dissociation of biexcitons in free electrons and holes being prevented by the confining barriers. Thus eq. 2.17 represents only a first approximation. The Schrödinger equation derived from eq. 2.17 was solved by various groups [30–34]. The theoretical calculations showed that, in comparison to the bulk, the binding energy of biexcitons in nanocrystals is larger and both ground- and excited two-pair states can be observed in optical spectra. Confinement effects lead to the disappearance of typical bulk continuum states and to changes in the selection rules thus allowing transitions to excited two-pair states, which in bulk semiconductors are forbidden. A scheme of optical transitions in QDs [28] considering both one- and two-pair states is illustrated in figure 2.6.

Combination of carriers situated on different levels of conduction- (electrons) and valence band (holes) develops into a whole ensemble of one-pair states (excitons). Thus beside the lowest exciton state ( $1S_{3/2}, 1s_e$ ), a series of combinations between

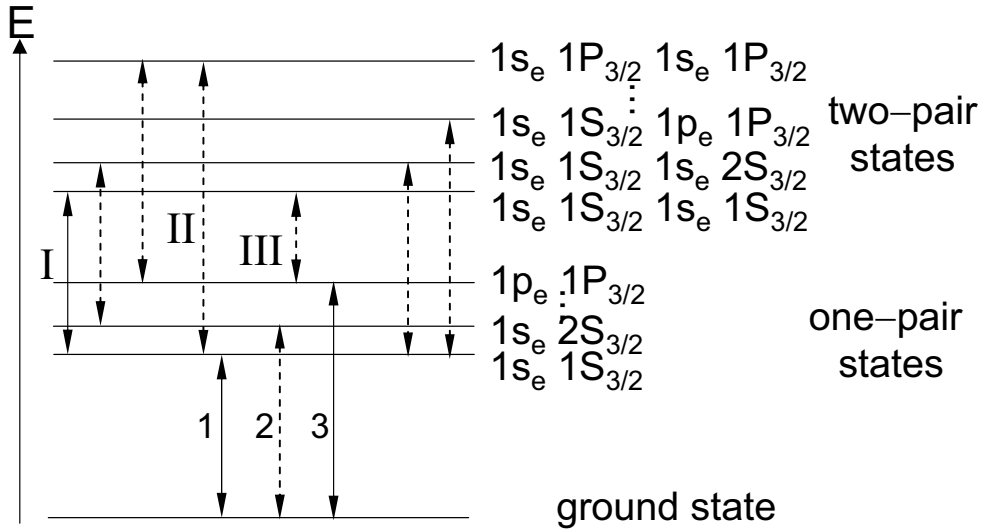


**Fig. 2.6:** Optical transitions in QDs for a two-particle system. The energy levels for one- and two-pair states are illustrated. For details – see text.

electrons and holes populating excited states appear. Further, such exciton states involving carriers in both ground and excited states can also interact with each other. Thus, beside the lowest two-pair (biexciton) state combining carriers in the ground state ( $1S_{3/2}, 1s_e, 1S_{3/2}, 1s_e$ ), a multitude of biexciton states involving carriers in excited states is created (i. e. ( $1S_{3/2}, 1s_e, 2S_{3/2}, 1s_e$ )).

The relaxation of selection rules due to Coulomb interaction is responsible for the optical transitions. The strongest biexciton transition (I) is situated energetically below the lowest exciton resonance (1) and is separated from the latter by the biexciton binding energy. The transitions involving excited states of carriers are weaker than (I) and both can be observed: transition (II) appears energetically higher, whereas (III) lies energetically below the lowest one-pair transition (see figure 2.6).

Additional Coulomb forces described by the term  $\delta V(\epsilon_1, \epsilon_2, r_e, r_h)$  in eq. 2.17 contribute to the binding energy of biexciton states. Thus, surface polarization induced by the difference in the dielectric constants of the host material  $\epsilon_1$  and the semiconductor  $\epsilon_2$  also contributes to the stabilization of biexciton states and

calculations [30] proved that the stability of biexcitons increases with an increasing ratio  $\epsilon_2/\epsilon_1$ .

### 2.3.3 Interaction of Many Particles

In a first approximation, Efros and Efros [16] considered the weak confined model in order to describe electron-hole pair states in large QDs. This model is valid only in bigger QDs (having larger diameter with respect to the exciton Bohr radius) and the confinement effects don't influence the relative coordinates of electrons and holes. Thus the particle in an infinite box problem (high potential barriers) can be reduced to a quantized center-of-mass motion.

The number of energy states and the distance between them is determined by the height of the potential barrier, which scales inversely proportional to the square of the QD's radius  $1/R^2$ . Therefore, in the weak confinement regime, the separation between the energy states tends to disappear leading to a rapidly increasing number of states per unit energy. However, approaching these energy levels doesn't yield a continuum of states like in the bulk. In contrast to the bulk, the exciton and biexciton states in semiconductor nanocrystals embedded in glass matrix are well separated and clearly distinguishable in form of Lorentzian line shape in optical absorption spectra. This line shape arises from the underlying series of confined overlapping energy levels [35]. Here, the two-level model, often used to describe small QDs is no longer valid and the nonlinear optical behavior of QDs in weak confinement regime is described by the many-particle system and its possible interactions.

The system of "many-particles" refers here to "many-excitons" accumulated in one quantum state. Here Pauli's principle is no longer obeyed, because excitons and biexcitons are bosons with integer quantum numbers, in contrast to electrons and holes which are fermions. Unbound and bound pair states (excitons and biexcitons) are created via exchange and polarization interactions. The population of



the energy states follow Bose-Einstein statistics, the optical transitions being connected to changes in the occupation number larger than one. Also considering the exciton–exciton interaction, which leads to homogeneous broadening, boson statistics explain well the blue shift (with respect to the bulk) of the exciton line shapes in the absorption spectra [36]. However, for a complete understanding of confinement induced blue shift of exciton levels other phenomena such as changing in the occupation number of the lowest exciton states or higher pair transitions also have to be taken into account [28].

Although the simple two-level system provides valuable information in characterization of relaxation dynamics in QDs with discrete level structure, the correct understanding of optical properties of bulk semiconductors requires a many-body formalism.



### 3 Low Wavenumber Raman Spectroscopy on CdSSe Quantum Dots

*Raman spectroscopy is one of the best nondestructive techniques providing information about the structure and the electronic vibrational states in confined systems. In this chapter off-resonant low wavenumber Raman spectroscopy is applied in order to investigate energetic and optical properties of  $CdS_xSe_{1-x}$  quantum dots embedded in a glass matrix.*

*In bulk semiconductors, the acoustic phonons show very low intensity and therefore their presence haven't been evidenced yet. However, in quantum confined systems 3D confinement of electrons and holes leads to modifications in the energy distribution and to a large enhancement of the intensity of acoustic vibrational modes. Moreover, their wavenumber depends inversely proportional on the QD's size. In this chapter the attention is focused on the contribution of the homogeneous broadening of the symmetric vibrational mode. Key-properties of the samples like QD's size and the size distribution inside the inhomogeneous broadening of the nanocrystals is estimated by means of Raman spectroscopy under off-resonant scattering conditions. Special care was taken to the polarization of the laser beam, making vibrations of different symmetry available to monitor.*

Here, a systematic study of the low wavenumber Raman (LWR) scattering of confined acoustical modes in  $CdS_xSe_{1-x}$  QDs of various size and chemical composition will be presented. The samples are commercially available Schott filter glasses, namely GG495, OG515, OG530, OG550, OG570 and RG590, where the numbers next to the letters indicate the cut-off wavelength of the glass, which depends both on the QD's size and on their chemical composition (the fraction  $x$  of S atoms). The chemical composition of the nanocrystals was determined in resonance Raman scattering regime by the group of Dr. M. Ivanda at the Ruder Boskovic Institute, Zagreb, Croatia and do not constitute a subject of this study [37].

This section focuses on the off-resonant excitation of the samples presented above. The off-resonance regime is achieved by employing the krypton ion laser line at 647 nm for the Raman excitation process. The spectra were recorded with a Spex 1403 double monochromator equipped with a multichannel detection system (CCD camera Photometrics RDS 900). The  $90^\circ$  scattering geometry was used to record Raman spectra very close to the Rayleigh line ( $\approx 4 \text{ cm}^{-1}$ ). The excitation power density of  $400 \text{ W/cm}^2$  was focused on the sample using a cylindrical lens, therefore taking special care to avoid local heating of the glass. The samples were kept at room temperature and before recording the Raman spectra, they were exposed for an hour to the same laser power. Such an exposure leads to photodarkening of the samples and consequently to a more favorable detection of the Raman scattered light, due to a strong decrease in the photoluminescence, which usually masks the weak Raman signal. Linearly polarized laser light was used for excitation and the Raman spectra were recorded under two polarization configuration: VV polarization geometry meaning that the excitation light is vertically polarized and the scattered light also analyzed vertically, and HV polarization geometry considering that the excitation light is horizontally polarized and the scattered light is vertically analyzed with respect to the scattering plane.

In a first approximation, the QDs are free, homogeneous and perfectly symmetric spheres. The spectra of acoustical vibrations of such a free spherical nanoparticle

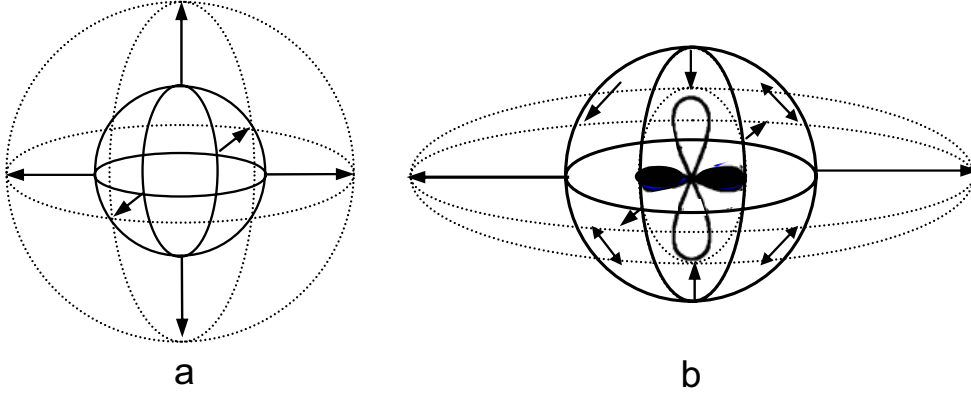


**Fig. 3.1:** Acoustic vibrational modes of a free, homogeneous, elastic sphere: a. spheroidal mode – breathing mode labelled  $l=0$ , active only in VV polarization geometry; b. torsional mode – quadrupolar mode labelled  $l=2$ , active in both VV and HV polarization geometries.

contains two types of vibrational modes: spheroidal and torsional ones as shown in figure 3.1 *a* and *b*, respectively [38].

The modes are classified according to the symmetry group of a sphere by the indices  $l$  and  $m$ , in analogy to the harmonic functions  $Y_{lm}$ . The values  $l$  measure the number of wavelengths along a circle on the surface. A third index  $p=1,2,\dots,n$  labels the sequence of the eigenmodes in increasing order of wave number and radial vector, for a fixed angular shape  $(l,m)$ . However, for a spherical particle only the spheroidal modes labelled  $l = 0$  (symmetric) and  $l = 2$  (quadrupolar) are Raman active [39]. The wavenumbers  $\tilde{\nu}$  of these modes, i.e. the lowest energy of the  $l = 0, 2$  sequences, depend inversely proportional to the diameter  $D$  of the nanoparticles:

$$\tilde{\nu} = \frac{S_l v}{cD}, \quad (3.1)$$

where  $v$  is an average value for the longitudinal and transversal sound velocity, calculated taking into account the orientation of the crystal axis,  $c$  is the light velocity and  $S_l$  is a dimensionless coefficient depending on the angular momentum  $l$ , on the harmonic number  $n$  and on the ratio between the longitudinal and transversal

sound velocities  $v_L/v_T$  [38].

For the studies presented in the following, the sound velocities valid in bulk materials were used, i.e. in CdS  $v_L = 4250$  m/s and  $v_T = 1860$  m/s and in CdSe  $v_L = 3690$  m/s and  $v_T = 1620$  m/s, respectively [40], calculated taking into account different crystalline directions (1,5,7 for  $v_L$  and 2,3,4,5,6 for  $v_T$ , respectively). Thus the proportionality constants  $S_0 = 0.84$  and  $S_2 = 0.91$  were determined, which have the same values for both CdS and CdSe ensembles and don't depend on the type of material. For simplification, all constants can be included in a single value, marked  $\beta$  and eq. 3.1 can be thus rewritten as:

$$D = \frac{\beta}{\nu}. \quad (3.2)$$

The numerical values of  $\beta$  were determined individually:

1. for the symmetric vibrations
  - in CdS  $\beta = 1.29 \times 10^{-5}$  and
  - in CdSe  $\beta = 1.12 \times 10^{-5}$
2. for the quadrupolar vibrations
  - in CdS  $\beta = 0.52 \times 10^{-5}$  and
  - in CdSe  $\beta = 0.46 \times 10^{-5}$  .

Further, the off-resonantly excited acoustic vibrational modes will be analyzed in the framework of a theoretical model. The Raman scattering intensity on a system with spatially confined vibrations is generally described by the Shuker-Gammon relation [41]:

$$I(\nu, T) = \frac{n(\nu, T) + 1}{\nu} C(\nu) g(\nu), \quad (3.3)$$

---

where  $C(\nu)$  is the light-to-vibration coupling coefficient,  $g(\nu)$  is the density of vibrational states,  $T$  the temperature and  $n(\nu, T) + 1$  is the Bose-Einstein occupation factor for the Stokes component. Under off-resonance conditions, the light-to-vibration coupling coefficient is proportional to the particle diameter [38]  $C(\nu) \sim D$  and the density of vibrational states  $g(\nu)$  is given by the number  $N(D)$  of particles vibrating with the frequency  $\nu$ . Therefore, the corresponding relation  $g(\beta/\nu) \sim N(D)$  yields the particle size distribution  $N(D)$  as a function of the density of the symmetric and quadrupolar modes. The distribution of the particle size  $N(D)$  as a function of the diameter of the vibrating particle is best described by a log-normal distribution:

$$N(D) = \frac{e^{-0.5[\ln u/\sigma]^2}}{d\sigma\sqrt{\pi/2}}, \quad (3.4)$$

where  $u = D/D_0$  and  $\sigma$  is the distribution width.

For off-resonance conditions the main contribution to the Raman signal comes from particles with diameters larger than the average diameter of the QDs in the sample ( $D > D_0$ ) and therefore the whole spectrum of nanocrystals' sizes can be included. The intensity of the Raman signal in off-resonance scattering conditions is therefore given by the integral:

$$I(\nu, E_{exc}) \sim \frac{n(\nu) + 1}{\nu} \int C(\nu, D)N(D)dD. \quad (3.5)$$

Figure 3.2 shows the theoretically determined Raman spectra for the studied samples applying eq. 3.5 and the log-normal distribution eq. 3.4 for different distribution widths  $\sigma$ . The calculations were performed based on the approach of Montagna and Dusi [38] for the Raman spectra recorded under VV polarization geometry of the symmetric vibrational modes, using the following parameters:  $v_L = 5960$  m/s,  $v_T = 3790$  m/s for the sound velocities,  $\rho = 2.3$  g/cm<sup>3</sup> for the density of the silica glass, and  $\rho_{CdS} = 4.87$  g/cm<sup>3</sup> and  $\rho_{CdSe} = 5.66$  g/cm<sup>3</sup> for the density of CdS and CdSe, respectively. The resulting spectra show the homogeneous broadening of the vibrational modes, caused by the interaction of the nanoparticles with the surround-

ing medium. The narrow spectrum of a free particle is also presented in figure 3.2 for comparison. Thus the effect of the surrounding glass matrix on the vibrational modes is evident. The inset in figure 3.2 shows the influence of the distribution width  $\sigma$  on the symmetric mode peak  $\nu_M$  and on the normalized full width at half maximum of the symmetric mode  $\Gamma_{FWHM}/\nu_M$ .

Figures 3.3 and 3.4 show the low wavenumber Raman spectra in VV and HV polarization geometries, respectively, recorded under off-resonance scattering conditions. The shift of the position (in wavenumbers) of the acoustic vibrations of  $CdS_xSe_{1-x}$  QDs on the particle's size is clearly distinguishable. In the polarized VV spectra, both types of modes, symmetric ( $l = 0$ ) and quadrupolar ( $l = 2$ ) are observable. Besides the symmetric surface mode labelled  $p = 1$ , the symmetric inner modes  $p = 2, 3$  are clearly observable in the spectra (figure 3.3). The quadrupolar vibrational mode is depolarized and therefore only this mode appears in the HV polarized Raman spectra (figure 3.4). For the quadrupolar mode, no higher harmonics (inner modes with  $p > 1$ ) can be observed. The absence of the inner modes in the Raman spectra agrees with the theoretical calculations, which predict almost one order of magnitude lower Raman intensity of the inner modes [38].

In order to analyze the spectra shown in figures 3.3 and 3.4 several steps have to be taken into account. These include the extraction of the background given by the "boson-peak" and by the quasielastic scattering peak "QS". The "boson-peak" is a broad feature, common for most glasses, having its maximum near  $50 \text{ cm}^{-1}$ , whereas the low energy quasielastic scattering peak "QS" appears below  $30 \text{ cm}^{-1}$ . The acoustic vibrations are superimposed onto these two features, which make their detection more difficult. In order to remove the contribution of the low wavenumber quasielastic scattering, the HV polarized spectra were divided by the depolarization ratio of QS, whose numerical value, measured for the samples under discussion, is  $\rho_{QS} = 5/9$ . The resulting spectra were then subtracted from the VV polarized Raman spectra. It has to be noted, that the quadrupolar  $l = 2$  mode is depolarized and, therefore its contribution is mainly cancelled by applying this



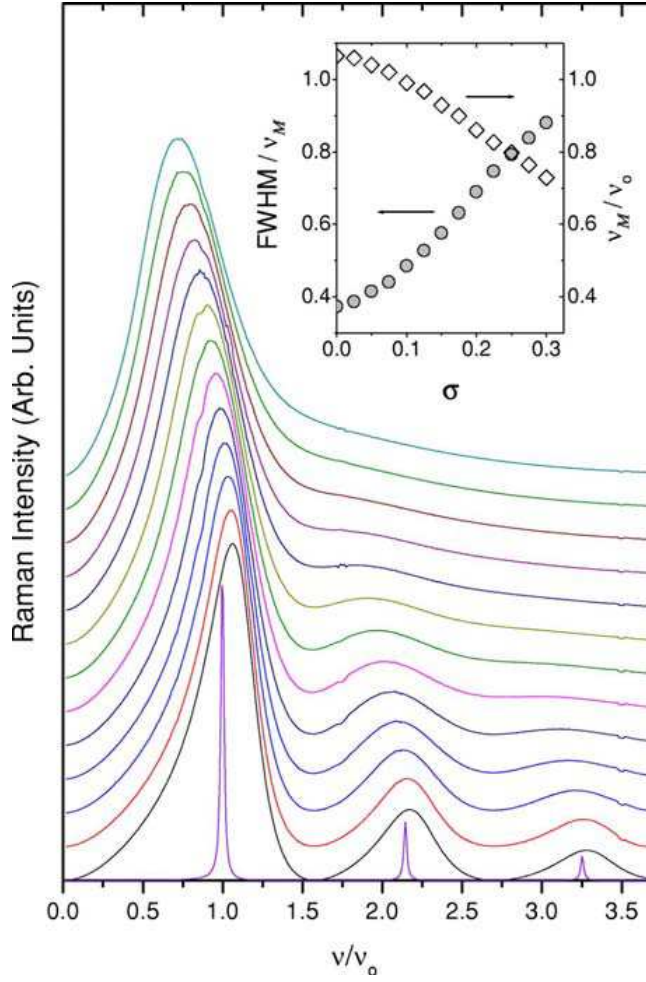


**Fig. 3.2:** The effects of the particle size distribution width  $\sigma$  on the surface  $p = 1$  and on the symmetric inner modes  $p = 2, 3, \dots$ . The first narrow spectrum represents the calculations for the free particle. The other spectra from bottom to top are homogeneously and inhomogeneously broadened spectra, with  $\sigma$  increasing from 0 to 0.3 in steps of 0.025. The peak wave numbers  $\nu_M$  were normalized to the maximum of the symmetric mode  $\nu_0$  of the free particle. The inset shows the influence of the distribution width  $\sigma$  on the symmetric mode peak  $\nu_M$  and on the normalized full width half maximum of the symmetric mode  $\Gamma_{FWHM}/\nu_M$ .

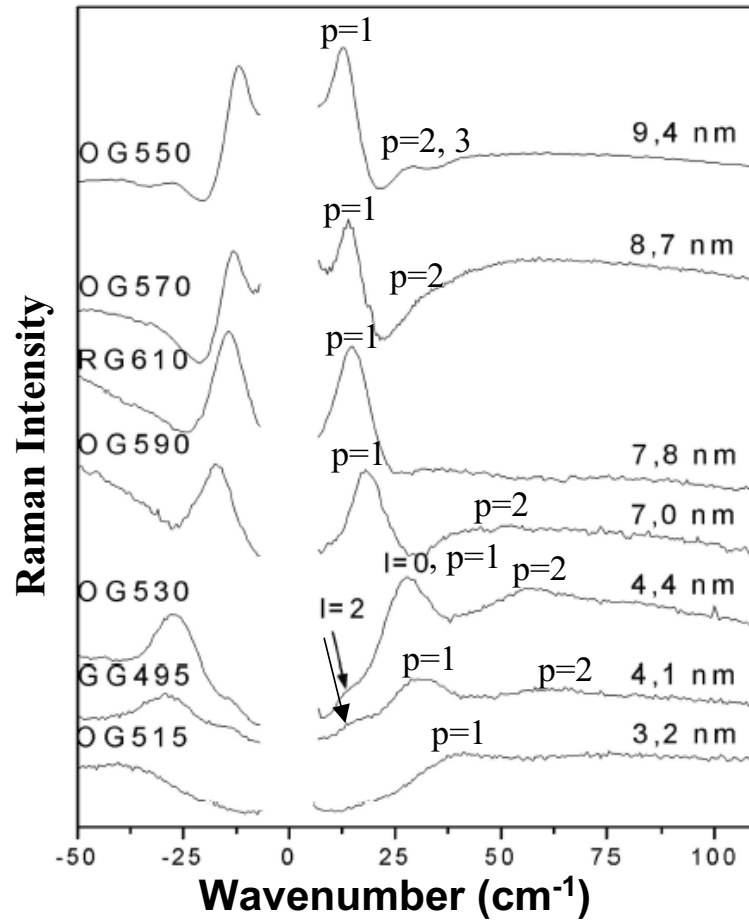


**Fig. 3.3:** Low wavenumber Raman spectra of  $CdS_xSe_{1-x}$  particles of different sizes, recorded in VV polarization geometry. The  $p$  sequence of the  $l = 0$  symmetric acoustic vibrational modes is labelled. For smaller particles, contained in OG530, OG515 and GG495 filter glasses, the  $l = 2$  modes are also visible.

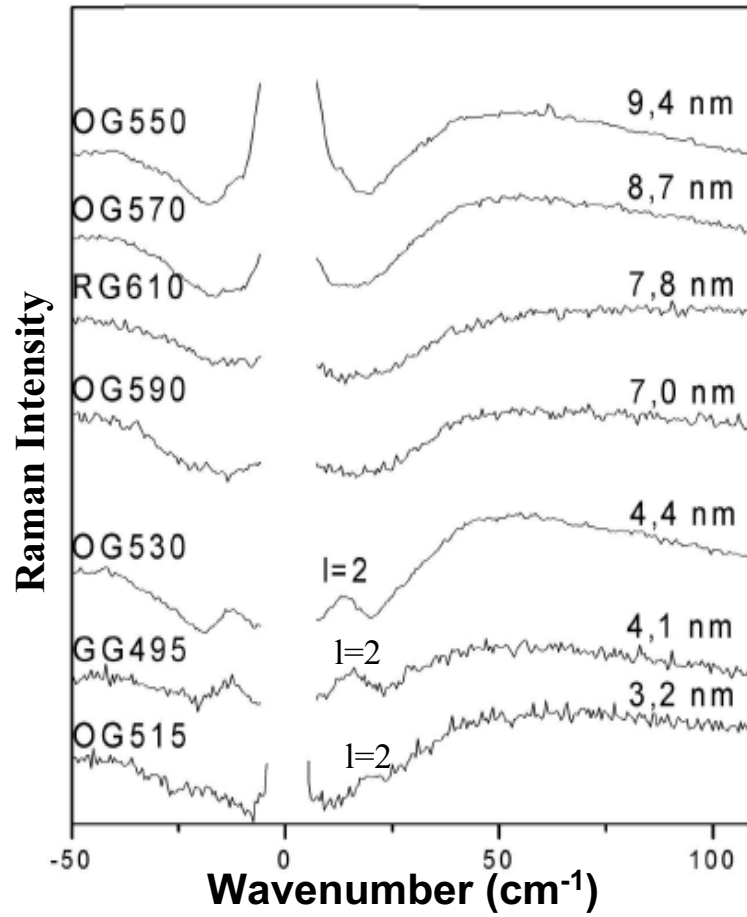


**Fig. 3.4:** Low wavenumber Raman spectra of  $CdS_xSe_{1-x}$  particles of different sizes, recorded in HV polarization geometry. The  $l = 2$  depolarized acoustic vibrational modes are visible.

calculation procedure. The resulted spectra  $VV - 9/5HV$  consists of the symmetric  $l = 0$  mode, its inner radial modes ( $p = 2, 3, \dots$ ) and the rest of the boson peak. In order to fit the boson peak for all spectra the phenomenological function  $cst \times \nu^3(40^2 + \nu^2)^{-1.7}$  [42] was used. After subtraction of the boson peak fit, the rest of the spectra containing only the symmetric surface and inner modes  $p = 1, 2, 3$  were subjected to a new fitting procedure with eq. 3.5. The results are shown in figure 3.5. The distribution widths  $\sigma$  obtained from the fit lie in the range between 15% and 17,5%. These values are in good agreement with the results of Irmer et al. [43], who measured the size distribution of  $CdS_xSe_{1-x}$  particles in Schott glass filters using x-ray scattering. They determined a sharp distribution of the FWHM of 20-30% of the mean particle diameters. From the inset in figure 3.2 the inhomogeneous contribution to the linewidth of the symmetric mode can be estimated to be  $\approx 30\%$ , which is a considerable value.

Due to the shift of the symmetric acoustic vibrational mode with the size distribution width  $\sigma$ , a corrected equation for the determination of the mean particle diameter has to be used:

$$D = \frac{(1.12 + 0.17x) \times 10^{-5}}{\nu_M} (1.12 - 1.13\sigma). \quad (3.6)$$

Here,  $\nu_M$  is the maximum wavenumber value of the observed symmetric mode peak,  $x$  is the CdS content, and  $\sigma$  is the size distribution width, which in the case of our Schott glasses lies between 0.15 and 0.175. This relation is valid for  $\sigma < 0.3$  and can be of practical interest.

To summarize, low wavenumber Raman scattering for off-resonant excitation conditions is an appropriate tool yielding the most important characteristics of QDs embedded in a glass matrix. The spectral shape and width of the symmetric acoustic vibrations were calculated taking into account both the homogeneous (interaction of the particles with the dielectric matrix) and the inhomogeneous broadening (due to particle size distribution inside the matrix). The comparison of the theoretically

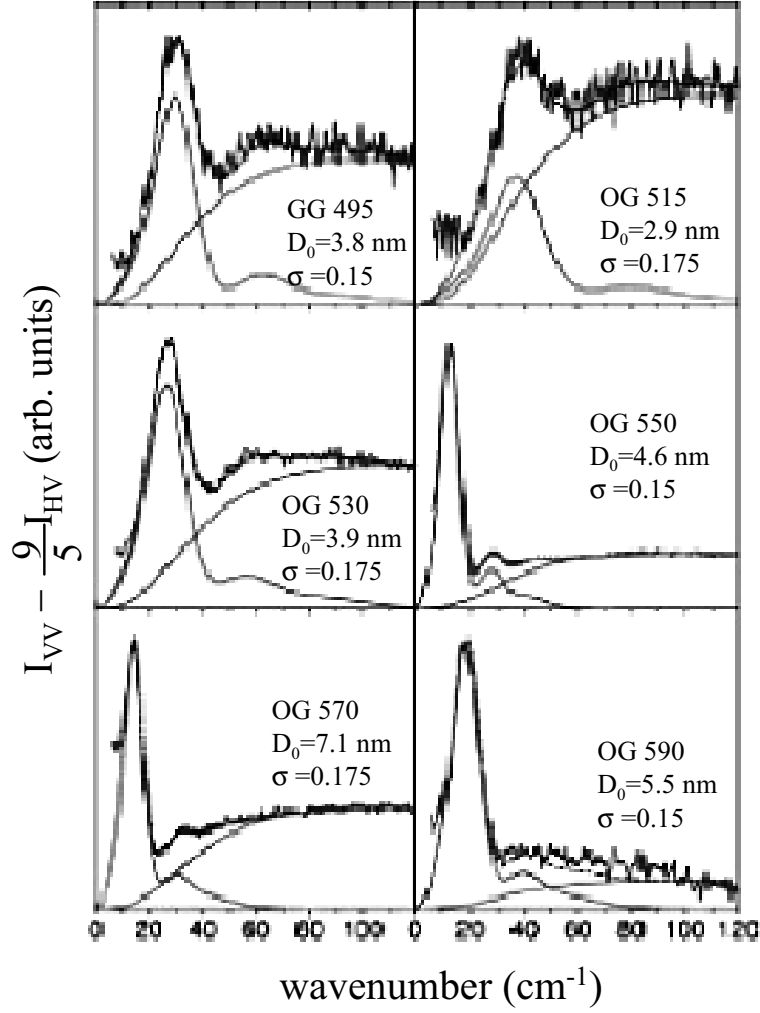


**Fig. 3.5:**  $I_{VV} - \frac{9}{5}I_{HV}$  spectra fitted with the boson peak and containing the  $CdS_xSe_{1-x}$  symmetric modes inhomogeneously broadened due to particles' size distribution. The parameters  $D_0$  and  $\sigma$  are results of the fit.

determined values with the experimental spectra allows one to determine the mean particle size and the distribution width for each sample individually.

In this chapter the key-parameters of the QDs were determined. However, the characterization of quantum confined systems is far from being complete. Further properties correlated to the energy distribution due to confinement of carriers are desirable to be analyzed. The investigation of the energetic structure, lifetime of different exciton states and the ultrafast relaxation processes in  $CdS_xSe_{1-x}$  require employment of pulsed laser beams and nonlinear spectroscopy techniques, presented in the following chapters.

## 4 Four-Wave-Mixing Spectroscopy

*This chapter gives a brief description of the four wave mixing spectroscopy technique, successfully applied to study ultrafast processes taking place in confined systems. The theoretical model supporting the applied ultrafast spectroscopy techniques is described in the first part of this chapter. The theoretical background is based on the treatment of the third order nonlinear susceptibility in the framework of a density matrix formalism. This formalism is extended by taking into account the propagation of third order nonlinear polarization and the Liouville theorem. For a better understanding of the four-wave mixing process, the theoretical model is completed by a schematic representation of the interaction processes using Feynman diagrams. The application of this model in the analysis of experimental spectra results in the determination of essential parameters like life- and spin dephasing time of different exciton levels. Moreover, as it will be shown in chapters 6 and 7, by applying this technique a successful description of symmetry characteristics and of nonlinear relaxation processes taking place in quantum confined systems can be achieved.*

## 4.1 Theoretical Model

The rapid development of ultrafast spectroscopy techniques [44–47] made the investigation of various dynamical processes taking place in sub picosecond range possible. In order to avoid artifacts introduced by coherent effects, spectrally resolved common pump-probe spectroscopy is combined with transient grating techniques based on four-wave-mixing (FWM) spectroscopy, which were proved to be powerful methods to study nonlinear properties of semiconductors [48–53]. In the simplest approximation, the coherent phenomena in semiconductors are analyzed for an ensemble of independent two-level systems treating third order optical interactions in the framework of perturbation theory. Details concerning the FWM processes can be found in many excellent books [54–61]. Here only a brief description of the femtosecond pump-probe transmission and of the most general form of FWM technique, namely degenerate four-wave-mixing (DFWM) in the framework of transient grating are given.

Beginning with a general approach, particularities of the theoretical model will be developed for the spectroscopy methods utilized in chapters 6 and 7 applied to characterize quantum confined systems. Here we refer to an ensemble of  $CdS_xSe_{1-x}$  semiconductor QDs embedded in a glass matrix.

The first approximation includes a classification of the system in two parts: a small quantum system containing only a few energy levels, which correspond to the well separated energy levels of the excitons in QDs, and a macroscopic thermal bath, which corresponds to a phonon bath. Although only the quantum system is coupled to the light, its phase coherence is strongly affected by the coupling to the phonon bath. Thus the quantum system has a limited number of degrees of freedom and its reduced density matrix has a reasonable size. The simplest approximation to treat the coupling between the excitons and the phonon bath is based on the Bloch equation, which despite of drastic approximations (i.e. including only Markovian processes) has been proved to be very useful for the illustration and understanding



the basic physics of femtosecond dynamics.

The evolution of a two-level quantum system is described by its density matrix  $\rho$ . Taking into account only Markovian processes, the density matrix can be written:

$$\rho = \begin{bmatrix} n & p \\ p^* & 1 - n \end{bmatrix}, \quad (4.1)$$

where  $n$  and  $1 - n$  are population terms, which represent the *probability* for the system to occupy one or the other level, respectively. The off-diagonal elements  $p$  and  $p^*$  represent the *coherence* intrinsic to a superposition state. The density matrix introduced in Liouville's theorem results in the Bloch equation [48], which, taking into account the coupling to the bath, leads to the equation describing the evolution of the system:

$$i\hbar \frac{d\rho}{dt} = [H_0, \rho] + [W(t), \rho] + i\hbar \frac{\partial \rho}{\partial t} |_{relax}, \quad (4.2)$$

where  $H_0$  is the reduced unperturbed Hamiltonian,  $W(t) = -\mu E(t)$  is the dipolar interaction with the total electric field  $E(t)$  of the incident femtosecond pulses, and  $\mu$  the electric-dipole operator. The eigenstates of the unperturbed Hamiltonian are  $H_0|n\rangle = \hbar\omega_n|n\rangle$ . The interaction with the phonon bath leads to a relaxation term

$$\frac{\partial \rho_{nm}}{\partial t} |_{relax} = -\Gamma_{nm}(\rho_{nm} - \rho_{nm}^{(0)}), \quad (4.3)$$

with  $\Gamma_{nm}$  the decay rate of the relaxation process, which corresponds to a dephasing rate when  $n \neq m$  ( $n$  and  $m$  are the two different energy levels) and to a population relaxation rate when  $n = m$ . The non-diagonal terms of the density operator at thermal equilibrium  $\rho^{(0)}$  are all zero. Assuming only the ground state as being populated ( $\rho_{00}^{(0)} = 1$  and all other matrix elements zero), the matrix elements of the two commutators in eq. 4.2 are:

$$\begin{aligned}
 \langle n|[H_0, \rho]|m \rangle &= \langle n|H_0\rho - \rho H_0|m \rangle \\
 &= \langle n|\hbar\omega_n\rho - \rho\hbar\omega_m|m \rangle = \hbar\omega_{nm}\rho_{nm},
 \end{aligned} \tag{4.4}$$

where  $\omega_{nm} = \omega_n - \omega_m$  and

$$\begin{aligned}
 \langle n|[W, \rho]|m \rangle &= \langle n|W\rho - \rho W|m \rangle = \sum_l (W_{nl}\rho_{lm} - \rho_{nl}W_{lm}) \\
 &= -E(t) \sum_l (\mu_{nl}\rho_{lm} - \rho_{nl}\mu_{lm}),
 \end{aligned} \tag{4.5}$$

where  $n, m$  and  $l$  are summation indices, indicating different energy states.

Thus the evolution of the density matrix can be written as:

$$\left( i\frac{d}{dt} - \omega_{nm} + i\Gamma_{nm} \right) \rho_{nm}(t) = -\frac{E(t)}{\hbar} \sum_l (\mu_{nl}\rho_{lm}(t) - \rho_{nl}(t)\mu_{lm}). \tag{4.6}$$

This equation can be solved introducing Green functions and Fourier transform [47], thus obtaining for the density matrix:

$$\rho_{nm}(t) = G_{nm}(t) \otimes (E(t) \sum_l [\mu_{nl}\rho_{lm}(t) - \rho_{nl}(t)\mu_{lm}]), \tag{4.7}$$

where

$$G_{nm}(t) = \frac{i}{\hbar} \Theta(t) \exp(-i\omega_{nm}t - \Gamma_{nm}(t)) \tag{4.8}$$

with  $\Theta$  the Heaviside step function. The Green function can be interpreted as the impulsive response function of the material.

### 4.1.1 Perturbation Theory

If the electric field is small enough, it can be considered as a small perturbation to the equilibrium of the system. This allows one to expand the density operator into a perturbation series [62–65]

$$\rho(t) = \rho^{(1)}(t) + \rho^{(2)}(t) + \rho^{(3)}(t) + \dots, \quad (4.9)$$

where  $\rho^{(p)}$  is the  $p^{\text{th}}$  order of  $\rho$  in the electric field. This perturbation expansion allows one to compute the term of order  $p + 1$  from the  $p^{\text{th}}$  element:

$$\rho_{nm}^{(p+1)}(t) = G_{nm}(t) \otimes E(t) \sum_l [\mu_{nl} \rho_{lm}^{(p)}(t) - \rho_{nl}^{(p)}(t) \mu_{lm}], \quad (4.10)$$

thus obtaining a sequence of equations allowing one to iteratively compute the density matrix up to any order in the electric field.

Considering the simplest case of a two-level system consisting of a ground state  $|g\rangle$  and an excited state  $|e\rangle$ , the only non-zero matrix element of the dipole operator is  $\mu_{eg}$  and eq. 4.7 results in

$$\rho_{eg}(t) = \mu_{eg} G_{eg}(t) \otimes \{E(t)[\rho_{gg}(t) - \rho_{ee}(t)]\}, \quad (4.11)$$

which connects population terms to coherent terms, and

$$\rho_{ee}(t) = G_{ee}(t) \otimes \{E(t)[\mu_{eg} \rho_{ge}(t) - \mu_{ge} \rho_{eg}(t)]\}, \quad (4.12)$$

connecting coherence terms to population terms. Thus through the perturbation expansion an alternating development is obtained:

$$\rho_{gg}^{(0)} \longrightarrow \rho_{eg}^{(1)} \longrightarrow \rho_{ee}^{(2)} \longrightarrow \rho_{eg}^{(3)} \longrightarrow \dots$$

Considering the system in equilibrium and at zero temperature ( $\rho_{gg}^{(0)} = 1$ ), the first three terms of the expansion can be determined from eq. 4.11 and eq. 4.12 [47]. Thus the first-order coherence is:

$$\rho_{eg}^{(1)}(t) = \mu_{eg} G_{eg}(t) \otimes E(t), \quad (4.13)$$

which is used in order to obtain by iteration the second-order population term:

$$\rho_{ee}^{(2)}(t) = -|\mu_{eg}|^2 G_{ee}(t) \otimes (E(t)\{[G_{eg}(t) + G_{ge}(t)] \otimes E(t)\}), \quad (4.14)$$

and, further, the third-order coherence term:

$$\rho_{eg}^{(3)}(t) = 2\mu_{eg}\mu_{ge}\mu_{eg}G_{eg}(t) \otimes \{E(t)[G_{ee}(t) \otimes (E(t)\{[G_{eg}(t) + G_{ge}(t)] \otimes E(t)\})]\}. \quad (4.15)$$

In the case of a two-level system, only two relaxation times appear, given by the relaxation rates  $\Gamma_{eg} = 1/T_2$ , where  $T_2$  stays for the dephasing time of the ensemble, and  $\Gamma_{ee} = 1/T_1$ , where  $T_1$  is the population relaxation time of the excited energy level. The population life time  $T_1$  is strongly correlated to the dephasing time  $T_2$  of the system:

$$\frac{1}{T_2} = \frac{1}{T_2^*} + \frac{1}{2(T_{1g} + T_{1e})}, \quad (4.16)$$

where  $T_2^*$  is the pure dephasing time of the system due to interactions with the environment (i.e. collisions with defects) [59, 66]. Furthermore, the interaction of the electric fields with a two-level system will be discussed, taking into account the polarization induced in the ensemble.

### 4.1.2 Induced Polarization

The optical properties of the system are determined by the macroscopic polarization induced in the material, which is actually responsible for the emission of the radiated electric field. For an ensemble of  $N$  identical, independent systems per unit volume, the total polarization per unit volume is connected to the density matrix by the mathematical relation:

$$P(t) = N \langle \mu \rangle = N \text{Tr}\{\mu\rho(t)\} = N \sum_{nm} \mu_{mn}\rho_{nm}, \quad (4.17)$$

which can be expanded like the density operator into a perturbation series:

$$P(t) = P^{(1)}(t) + P^{(2)}(t) + P^{(3)}(t) + \dots \quad (4.18)$$

Thus the  $(p + 1)^{th}$  component of the macroscopic polarization can be computed, analogous to the density matrix, from the  $p^{th}$  term of the series. Applying Liouville's theorem from eq. 4.2, one can compute the nonlinear susceptibility tensors  $\chi$ :

$$P^{(p)}(t) = \epsilon_0 \int_{-\infty}^{+\infty} \frac{d\omega_1}{2\pi} \dots \int_{-\infty}^{+\infty} \frac{d\omega_p}{2\pi} \times \chi^{(p)}(-\omega_s; \omega_1, \dots, \omega_p) E(\omega_1) \dots E(\omega_p) \exp(i\omega_s t), \quad (4.19)$$

where  $\omega_s = \omega_1 + \omega_2 + \dots + \omega_p$  with  $\omega$  the angular frequency of the incident electric field. The nonlinear susceptibility tensor is a constant of the material, but its dependence on the excitation frequency leads to memory effects which allow one to compute the response of the system at any sequence of femtosecond pulses. In the following, the dynamics of the quantum system will not be limited to this nonlinear susceptibility formalism, but the whole polarization terms will be directly used.

## 4.2 Femtosecond Spectroscopy

This section includes an adaptation of the theoretical model presented in the former section to the femtosecond spectroscopy techniques applied in chapters 6 and 7. First, the response of the system to the consecutive interaction with three incident laser pulses will be successively analyzed. Then, concrete relations describing nonlinear dynamics of the system for two different femtosecond spectroscopy techniques, namely femtosecond pump-probe spectroscopy and degenerative four wave mixing in the framework of transient grating will be presented.

### 4.2.1 First Order Polarization

A laser pulse of a given electric field

$$\mathcal{E}(t) = A \exp[i(kr - \omega t)], \quad (4.20)$$

propagating in the direction given by its wave vector  $k$  and angular frequency  $\omega$  incident on the sample induces a polarization in the sample volume. This polarization, called first order polarization, can be computed from the first order density operator:

$$\rho_{nm}^{(1)}(t) = G_{nm}(t) \otimes [E(t) (\mu_{nm} \rho_{mm}^{(0)} - \rho_{nn}^{(0)} \mu_{nm})], \quad (4.21)$$

where  $E(t)$  represents the real part of the electric field  $E(t) = \text{Re}\mathcal{E}(t)$ , with  $\mathcal{E}$  staying for the total electric field composed of a real and an imaginary part. Applying a Fourier transformation eq. 4.21 results into

$$\rho_{nm}^{(1)}(\omega) = \mu_{nm} G_{nm}(\omega) E(\omega) (\rho_{mm}^{(0)} - \rho_{nn}^{(0)}). \quad (4.22)$$

Equation 4.22 introduced in eq. 4.17 can be used to calculate the induced first order polarization for an ensemble of  $N$  non-interacting identic systems:

$$P(\omega) = N \sum_{nm} \mu_{mn} \mu_{nm} G_{nm}(\omega) (\rho_{mm}^{(0)} - \rho_{nn}^{(0)}) \mathcal{E}(\omega). \quad (4.23)$$

The interaction of the electric wave with the sample can be illustrated using Feynman diagrams [55, 59–61] as shown in figure 4.1.

After the pulse has left the sample space, the induced polarization decays with a dephasing time  $T_2$  given by eq. 4.16. Using eq. 4.19, the linear susceptibility is determined from the linear polarization eq. 4.23:

$$\chi^{(1)}(\omega) = N \sum_{nm} \frac{-|\mu_{nm}|^2}{\hbar \epsilon_0} \frac{\rho_{mm}^{(0)} - \rho_{nn}^{(0)}}{\omega - \omega_{nm} + i\Gamma_{nm}}. \quad (4.24)$$

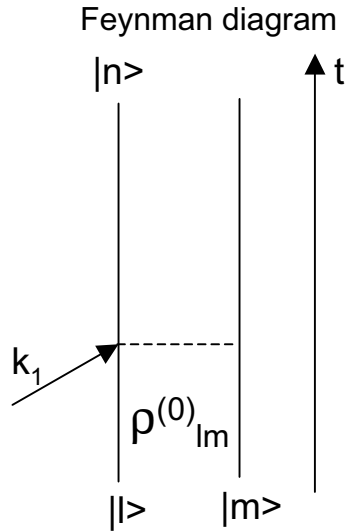


**Fig. 4.1:** Schematic representation of the interaction of a laser pulse with the sample material: Feynman diagram. The laser pulse with a wave vector  $k_1$  interacts with the sample and induces a coherence term  $\rho_{lm}^0$  between the two states  $l$  and  $m$ .

The real part of the linear susceptibility yields the refractive index, whereas the imaginary part gives the absorption coefficient. All these results are well known from linear optics and only show that the above formalism yields reasonable results in this regime. Linear terms are essential in developing higher order nonlinear properties. For the femtosecond experiments presented within this study, nonlinear terms of 2<sup>nd</sup> and 3<sup>rd</sup> order are of interest and will be described in the following.

### 4.2.2 Second Order Polarization

If a second pulse propagating in the direction given by its wave vector  $k_2$  is incident on the sample before the linear polarization induced by the first pulse (with wave vector  $k_1$ ) is dephased, the two polarization patterns will interfere in the sample volume and form a grating. The finite cross-section of the laser beams (figure 4.2) spatially limits the extent of the interference zone [67].

The dynamics of the population grating created by the interference of the two

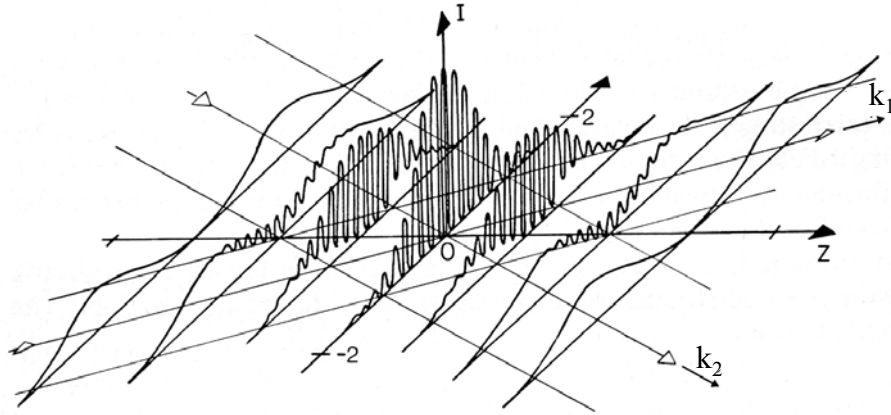


**Fig. 4.2:** Spatial distribution of intensity within the volume – grating pattern created by the interference of two Gaussian beams of equal intensity [67].

pulses is described by the second order polarization, which is computed from the second order coherence terms of the density operator:

$$\rho_{nm}^{(2)}(t) = \frac{|\mu_{nm}|^2}{2\hbar} \text{Im} \int_{-\infty}^t \mathcal{E}^*(t') [G_{nm}(t') \otimes \mathcal{E}(t')] dt', \quad (4.25)$$

where  $\mathcal{E}^*$  is the complex conjugate of the incident electric field of the second pulse and  $t$  represents the time when the second pulse arrives at the sample. In the case of a two-level system, the states  $|m\rangle$  and  $|n\rangle$  correspond to the ground  $|g\rangle$  and excited state  $|e\rangle$ , respectively. After the second pulse has left the sample volume, the excited population is given by [47]:

$$\rho_{ee}^{(2)}(+\infty) = \frac{|\mu_{eg}|^2}{2\hbar} \int_{-\infty}^{+\infty} |\mathcal{E}(\omega)|^2 \text{Im} G_{eg}(\omega) \frac{d\omega}{2\pi}. \quad (4.26)$$

In order to schematically illustrate the interaction process, several energy levels have to be taken into account because more than two energy levels are excited by the laser pulses. In the simplest case, where only 3 energy levels are involved, not only the population terms  $\rho_{11}$  and  $\rho_{22}$ , but also coherence terms  $\rho_{12}$  and  $\rho_{21}$  are excited (figure 4.3).



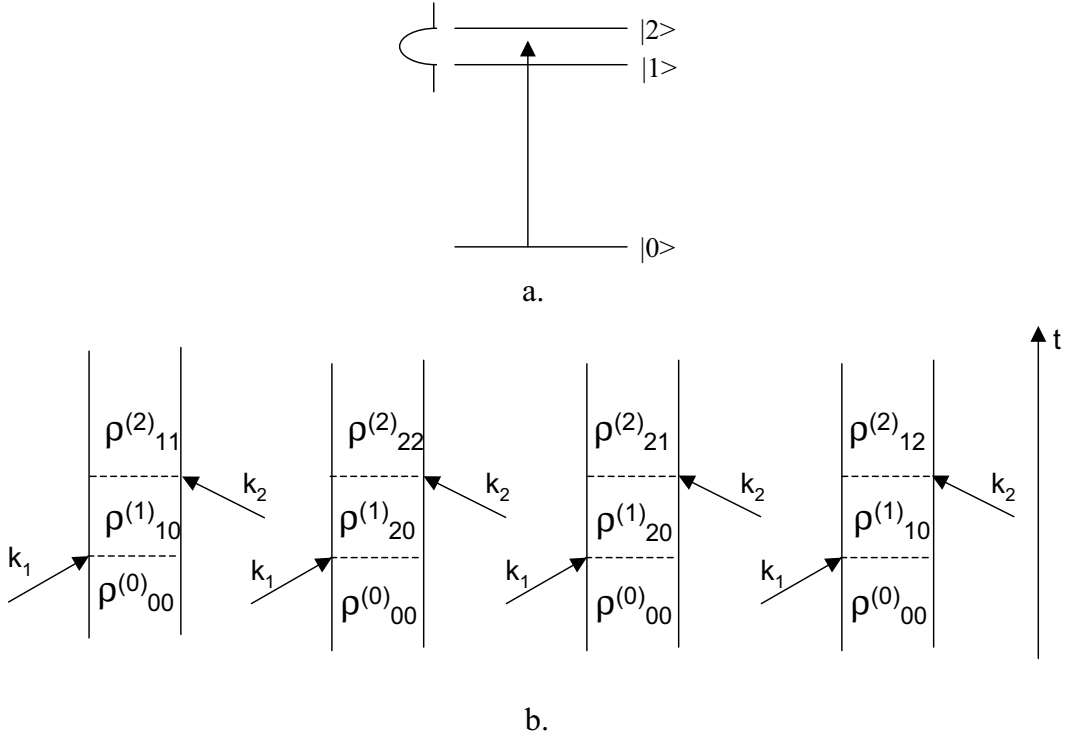


**Fig. 4.3:** Schematic representation of the interaction of the second laser pulse incident on the sample. a. Three-level system; b. Possible Feynman diagrams.

The coherence term between the excited states  $|1\rangle$  and  $|2\rangle$  can be obtained analogous to eq. 4.14:

$$\rho_{21}^{(2)}(t) = -\mu_{20}\mu_{01}G_{21}(t) \otimes (E(t)\{[G_{01}(t) + G_{20}(t)] \otimes E(t)\}), \quad (4.27)$$

and consequently, the second order polarization induced in the material is then given by:

$$P^{(2)}(t) = -\mu_{01}\mu_{12}\mu_{20}G_{21}(t) \otimes (E(t)\{[G_{01}(t) + G_{20}(t)] \otimes E(t)\}). \quad (4.28)$$

The second order polarization oscillates at the angular frequency  $\omega_{21}$  and its dephasing rate is given by  $\Gamma_{21}$ . It is interesting to observe that in the case of centrosymmetric systems, the second order polarization vanishes, due to the fact that

the product  $\mu_{01}\mu_{12}\mu_{20}$  is non-zero only in non-centrosymmetric systems [47].

### 4.2.3 Third Order Polarization

In order to explore higher order response functions of the system, more than one laser beam is usually used for the excitation. By controlling the time delay between the pulses a better exploration of the nonlinear response functions is achieved. For simplification, a two level system will be further considered and the two most common configuration geometries relevant for this work will be presented.

#### 4.2.3.1. Pump–Probe Spectroscopy

In the case of pump–probe experiments, two pulses are incident onto the sample: a pump pulse described by an electric field  $\mathcal{E}_P(\mathbf{r}, t) \sim \exp(i\mathbf{k}_P\mathbf{r})$  propagating in the direction  $k_P$ , and a probe (test) pulse  $\mathcal{E}_T(\mathbf{r}, t) \sim \exp(i\mathbf{k}_T\mathbf{r})$  propagating in the direction  $k_T$ . A signal can be observed in more than one direction, given by different phase matching conditions (see figure 4.4). One of these, interesting for the experiments presented in chapters 6 and 7, is given by the diffraction of the pump in the direction of the probe, which leads to a signal  $k_s$  propagating in the direction  $k_s = k_P - k_P + k_T = k_T$ .

In order to compute the third order density operator and the third order polarization, the total electric field

$$E(\mathbf{r}, t) = \frac{1}{2} [\mathcal{E}_P(\mathbf{r}, t) + \mathcal{E}_T(\mathbf{r}, t) + \mathcal{E}_P^*(\mathbf{r}, t) + \mathcal{E}_T^*(\mathbf{r}, t)] \quad (4.29)$$

has to be introduced into eq. 4.15. The fact that the total electric field is a combination of all incident electric fields (eq. 4.29) leads to many different combinations of the four terms. Only those terms, where all three incident fields  $\mathcal{E}_P(\mathbf{r}, t)$ ,  $\mathcal{E}_P^*(\mathbf{r}, t)$  and  $\mathcal{E}_T(\mathbf{r}, t)$  appear only once are relevant for the detected pump–probe signal [47, 48]. A schematic representation of the possible scattering directions of the pump–probe signal is shown in figure 4.4. The fs pump–probe experiments presented in chapter 6

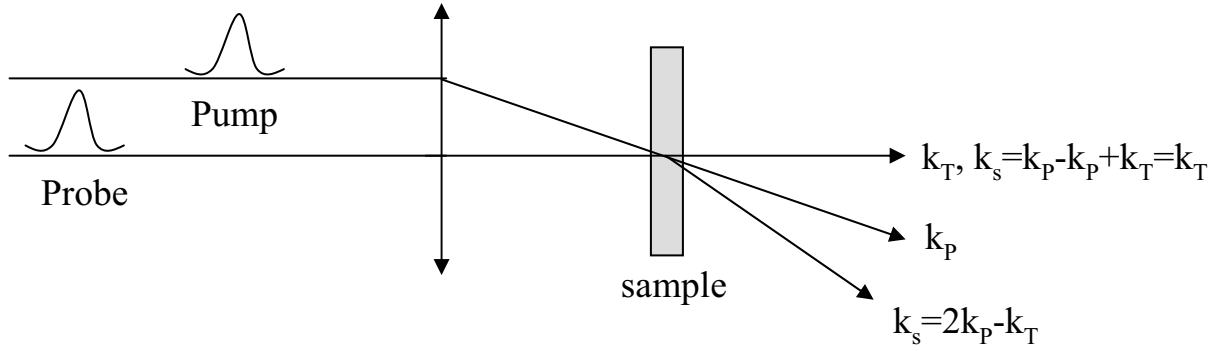


**Fig. 4.4:** Experimental set-up using two excitation beams in order to perform third order nonlinear optical measurements. [47] A signal can be observed in two directions given by the phase matching conditions:  $k_s = k_P - k_P + k_T = k_T$  and  $k_s = 2k_P - k_T$

were carried out recording the intensity of the pump-probe transmission signal in the direction  $k_s = k_T$ . This signal is related to the third order polarization  $P^{(3)}$  [47, 48]. In a pump-probe experiment, under the approximation that the probe pulse is much weaker in intensity than the pump pulse and the sample is very thin, usually the differential transmission signal is recorded:

$$\frac{\Delta I(\omega)}{I_0(\omega)} \approx \frac{n\omega L}{\epsilon_0 c} \text{Im} \frac{P^{(3)}(\omega)}{\mathcal{E}_T(\omega)}, \quad (4.30)$$

where  $n$  is the non-perturbed refractive index,  $\epsilon_0$  the non-perturbed permeability and  $L$  represents the thickness of the sample.

Once the density operator is known, the differential transmission signal is easy to evaluate. Further, the cases where in the Feynman diagram the pump appears twice and the probe only once will be discussed [63]. The time sequence of the incident pulses determines three different contributions to the differential absorption, which are illustrated in figure 4.5.

In the first two cases (figure 4.5a and b), the pump  $k_P$  and its complex conjugate propagating in the direction  $-k_P$  precede the probe pulse  $k_T$  and create a *population term*  $\rho_{ee}^{(2,PP)}$  which modifies the transmission of the probe pulse:

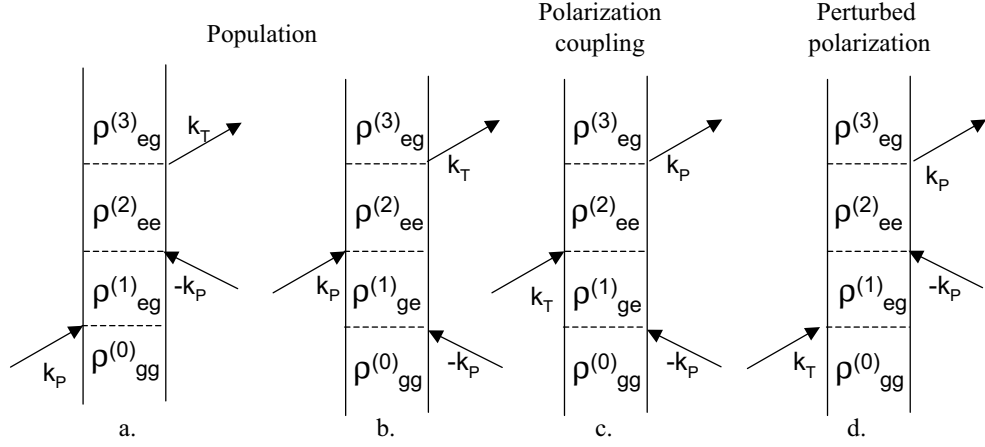


**Fig. 4.5:** Feynman diagrams for different time sequences of the laser pulses in a pump-probe experiment. The "minus" sign of the wave vector corresponds to the complex conjugate electric field  $\mathcal{E}^*$ .

$$\begin{aligned}
 \rho_{eg}^{(3,TPP)}(t) &= \frac{\mu_{eg}}{2} G_{eg}(t) \otimes \{ \mathcal{E}_T(t) [\rho_{gg}^{(2,PP)}(t) - \rho_{ee}^{(2,PP)}(t)] \} \\
 &= \frac{\mu_{eg}\mu_{ge}\mu_{eg}}{4} G_{eg}(t) \otimes [ \mathcal{E}_T(t) (G_{ee}(t) \otimes \\
 &\quad \{ \mathcal{E}_P^*(t) [G_{eg}(t) \otimes \mathcal{E}_P(t)] - \mathcal{E}_P(t) \\
 &\quad [G_{eg}^*(t) \otimes \mathcal{E}_P^*(t)] \} ) ] . \tag{4.31}
 \end{aligned}$$

In this case, the population created by the pump is probed by the test pulse and the signal appears only for positive delay times between these two pulses. The decay of the population is given by the decay time  $T_1$ . If the pump and the probe overlap in space and time, another contribution to  $\rho_{eg}^{(3)}$  emerges from the so called *pump-polarization coupling* represented in diagram c. of figure 4.5:

$$\begin{aligned}
 \rho_{eg}^{(3,PTP)}(t) &= \frac{\mu_{eg}}{2} G_{eg}(t) \otimes \{ \mathcal{E}_P(t) [\rho_{gg}^{(2,TP)}(t) - \rho_{ee}^{(2,TP)}(t)] \} \\
 &= \frac{\mu_{eg}\mu_{ge}\mu_{eg}}{4} G_{eg}(t) \otimes [ \mathcal{E}_P(t) (G_{ee}(t) \otimes \\
 &\quad \otimes \{ \mathcal{E}_T(t) [G_{eg}^*(t) \otimes \mathcal{E}_P^*(t)] \} ) ] . \tag{4.32}
 \end{aligned}$$

This signal can be interpreted as the diffraction of the pump beam in the direction of the probe beam, after the diffraction process on the population grating created by the interference between the pump and the probe.

For negative time delays between the excitation pulses, when the probe precedes the pump beam, a third contribution to  $\rho_{eg}^{(3)}$  is generated. It is called *perturbed polarization decay* [63,68] and it can be interpreted as a perturbation of the polarization induced by the probe pulse through the pump pulse:

$$\rho_{eg}^{(3,PPT)}(t) = \frac{\mu_{eg}\mu_{ge}\mu_{eg}}{4} G_{eg}(t) \otimes [\mathcal{E}_P(t) (G_{ee}(t) \otimes \{\mathcal{E}_P^*(t) [G_{eg}(t) \otimes \mathcal{E}_T(t)]\})]. \quad (4.33)$$

The major difficulty in such experiments represents the simultaneous use of spectral and temporal resolution due to validity of the time–frequency uncertainty principle. Another spectroscopic method, which avoids this difficulty is discussed in the next section.

#### 4.2.3.2. Photon Echo

The experimental setup for a four-wave mixing (FWM) experiment is presented schematically in figure 4.6. Such experiments are based on the successive interaction of three laser beams incident onto the sample. The separate control of delay times between all three pulses allows the investigation of more nonlinear phenomena occurring in the system as in the case of only two incident pulses.

The first (in time) pulse  $k_1$  induces a polarization in the sample, whereas the second pulse  $k_2$  interacts with the polarization pattern induced by  $k_1$  thus forming a grating. The third pulse propagating in the direction  $k_3$  is scattered on this grating (process similar to Bragg diffraction) in the direction given by the phase matching condition  $k_s = -k_1 + k_2 + k_3$  [48,59,69]. Of course, there are also other scattering directions corresponding to other phase matching conditions given by

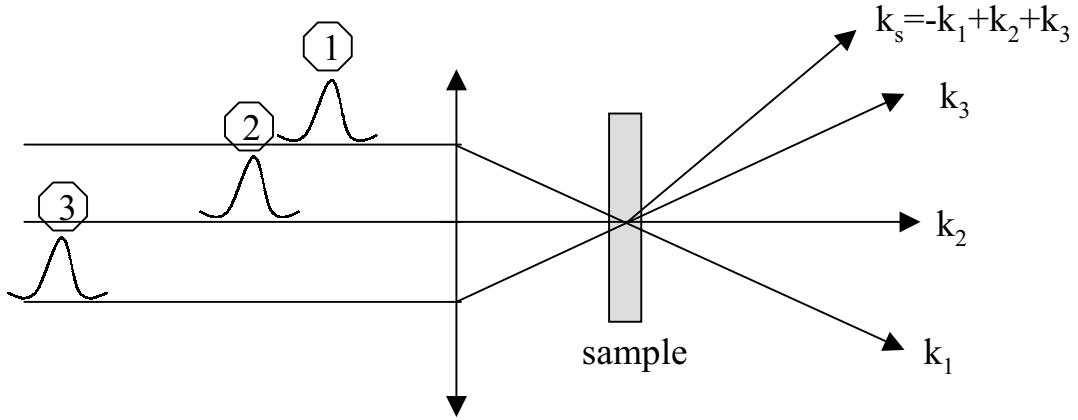


**Fig. 4.6:** Experimental set-up for FWM experiment using three-beam excitation [47].

another combination of the incident wave vectors, but only the former is of interest for the studies presented in chapter 6 and 7.

Thus the only relevant term in the nonlinear polarization describing this diffraction process is proportional to  $\mathcal{E}_1^* \mathcal{E}_2 \mathcal{E}_3$  and the corresponding Feynman diagram is given in figure 4.7. The FWM processes are achieved in the framework of transient grating experiments in form of photon echo, a process described by the Feynman diagram shown in figure 4.7a. The experimental setup for the *two-pulse photon echo* measurements is identical with the one shown in figure 4.4. The simplest form of photon echo is in principle identical with the pump-probe experimental setup with the signal collected in the direction  $k_s = 2k_P - k_T$ .

In the following, it will be referred to the general case of three-pulse photon echo experiments carried out in chapter 6 and 7. The contribution to the density operator can be directly derived from the Feynman diagram shown in figure 4.7a:

$$\rho_{eg}^{(3)} = \frac{|\mu_{eg}|^2 \mu_{ge}}{4} G_{eg}(t) \otimes [\mathcal{E}_3(t) (G_{ee}(t) \otimes \{\mathcal{E}_2(t) [G_{eg}^*(t) \otimes \mathcal{E}_1^*(t)]\})]. \quad (4.34)$$

Introducing the Heaviside step function  $\Theta$  and assuming infinitely short pulses [ $\mathcal{E}_\alpha(t) = \mathcal{E}_\alpha(t)(t - \tau_\alpha)$  where  $\tau = 1, 2, 3$  counts the time sequence of the incident

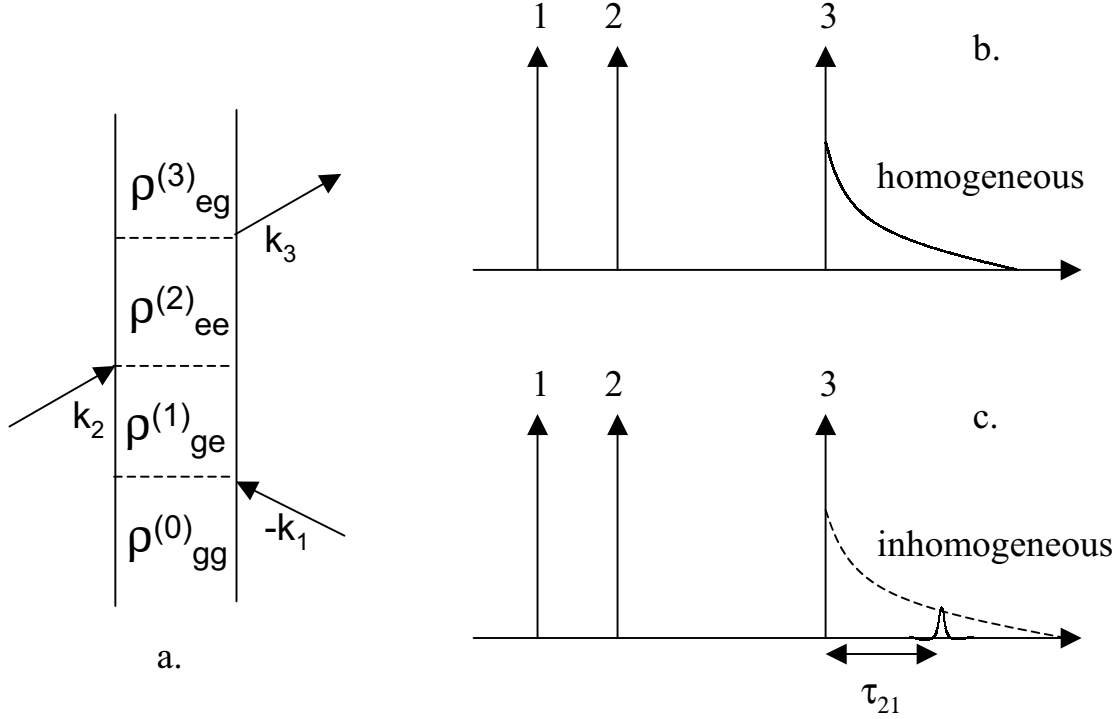


**Fig. 4.7:** a. Feynman diagram relevant to photon echo experiments. b. Induced polarization in a homogeneous system. c. Induced polarization in an inhomogeneous system. Here, the polarization looks like a small echo of the third (in time) pulse  $k_3$

pulses], the third order density operator can be expressed as a function of the dephasing time  $T_2$  and population relaxation time  $T_1$ :

$$\begin{aligned} \rho_{eg}^{(3)} &= -i \frac{|\mu_{eg}|^2 \mu_{ge}}{4\hbar^3} \Theta(t - \tau_3) \Theta(\tau_{21}) e^{-\tau_{32}/T_1} e^{-(t - \tau_3 + \tau_{21})/T_2} \\ &\quad \times \mathcal{E}_1^* \mathcal{E}_2 \mathcal{E}_3 \exp[-i\omega_{eg}(t - \tau_3 - \tau_{21})]. \end{aligned} \quad (4.35)$$

Thus the third order polarization occurs at the time  $t = \tau_3$ , just after the third pulse, its decay depending on the dephasing time of the material. The intensity of the recorded signal will be proportional to  $\exp(-2\tau_{21}/T_2)$ , where  $\tau_{21} = \tau_2 - \tau_1$  is the delay time between the pulses 2 and 1.

In the case of an inhomogeneously broadened system composed of independent

two-level systems with a Gaussian distribution of transition frequencies  $g(\omega_{eg})$ , the averaged density operator can be written:

$$\begin{aligned}
 \langle \rho_{eg}^{(3)} \rangle &= -i \frac{|\mu_{eg}|^2 \mu_{eg}}{4\hbar^3} \Theta(t - \tau_3) \Theta(\tau_{32}) \Theta(\tau_{21}) e^{-\tau_{32}/T_1} e^{-(t-\tau_3+\tau_{21})/T_2} \\
 &\quad \times \mathcal{E}_1^* \mathcal{E}_2 \mathcal{E}_3 \int_{-\infty}^{+\infty} g(\omega_{eg}) e^{[-i\omega_{eg}(t-\tau_3-\tau_{21})]} d\omega_{eg} \\
 &= -i \frac{|\mu_{eg}|^2 \mu_{ge}}{4\hbar^3} \Theta(t - \tau_3) \Theta(\tau_{32}) e^{-\tau_{32}/T_1} e^{-(t-\tau_3+\tau_{21})/T_2} \\
 &\quad \times \mathcal{E}_1^* \mathcal{E}_2 \mathcal{E}_3 g(t - \tau_3 - \tau_{21}), \tag{4.36}
 \end{aligned}$$

where  $g(t)$  is the Fourier transform of the frequency distribution  $g(\omega_{eg})$ . The time dependence of the corresponding photon emission process is governed by  $g(t)$ , so that the duration of the emission process scales inversely to the inhomogeneous linewidth, i.e. the inhomogeneous dephasing time. For an inhomogeneous system, the polarization decays first in the interval  $[0, \tau_{21}]$  and a second time in the interval  $[\tau_3, \tau_3 + \tau_{21}]$ , leading to an exponential dependence of the signal amplitude proportional to  $\exp(-2\tau_{21}/T_2)$ . Thus the time-integrated intensity of the photon echo signal decays with the constant  $T_2/4$ . Moreover, the echo signal provides information about the homogeneous dephasing processes in the system, independently from the inhomogeneous broadening.

One of the advantages of this method consists of the fact that the recorded signal is free from any background contributions from the incident beams. Although the theoretical model presented above is based on drastic approximations (i.e. only Markovian processes are taken into account), it can be successfully applied to interpret the experimental data presented in the chapters 6 and 7, proving to be a suitable tool to describe nonlinear processes in confined systems.



## 5 Experimental Setup

*This chapter focuses on the description of the laser system employed for the generation of the femtosecond laser pulses necessary to perform the experiments described in chapters 6 and 7. The first part of this chapter focuses on the procedure of generating and characterizing femtosecond laser pulses. One major advantage of the setup described here is the possibility of tuning the wavelength of the laser pulses over the whole visible range. The setup also enables one to individually control the time sequence of all three laser pulses, thus making various nonlinear processes accessible.*

*Another advantage of the setup consists in the ability to perform FWM experiments using different beam geometries, thus choosing different phase matching conditions. Here, only the beam geometries corresponding to the phase matching conditions applied for the experiments presented in chapters 6 and 7 are discussed. The degrees of freedom provided by these arrangements allow one to individually control the polarization of the incident laser beams, thus different dynamical processes in the system being accessible to study.*

## 5.1 Femtosecond Laser Pulses: Generation and Characterization

Although the nonlinear processes in confined systems usually occur on a picosecond time scale, for their ingenious investigation laser pulses in the femtosecond range are necessary. In this section the laser system used to generate femtosecond laser pulses will be presented. The actual generation and acquiring process will be only briefly described. Detailed information can be found in the literature [48, 70–72].

The laser system presented schematically in figure 5.1 generates laser pulses at a repetition rate of 100 kHz with a full-width half-maximum (FWHM) of 60-80 fs and an energy of 50-100 nJ/pulse, thus being suitable for the investigation of nonlinear dynamics in condensed matter. The fs-system consists of a Kerr-lens, mode-locked Titanium:Sapphire oscillator, a Titanium:Sapphire amplifier unit with a compressor and two white-light optical parametric amplifiers as shown in figure 5.1. The 25 W output power of an argon ion laser (Sabre, Coherent) operating in the multi-line mode is split in two parts. 8 W are used to pump the oscillator (MIRA, Coherent) and 17 W to pump the regenerative amplifier (RegA, Coherent). The oscillator is operated at 800 nm generating femtosecond laser pulses at 76 MHz with a FWHM of approximately 60 fs and an energy of 10 nJ/pulse. 30% of the oscillator power is used to read the amplifier. An opto-acoustic modulator is responsible for the selection of a single laser pulse to be coupled into and out of the cavity of the amplifier with a repetition rate of 100 kHz. To avoid independent lasing of the cavity, the Q-switch also realized by an opto-acoustic modulator allows the cavity to open exclusively for the time when the pulses are propagating in the amplifier. In order to avoid damages of the optics in the cavity, the pulse is stretched in its temporal profile by introducing dispersion during each of its round trips in the cavity. The pulses are amplified by multiple passes through the active medium of the cavity. The amplified pulses are coupled out of the amplifier. Multiple reflections on a holographic grating assures

compensation of the dispersion introduced during the amplification process. The outcoupled pulses show a FWHM of approximately 120 fs at a central wavelength of 800 nm with approximately 8  $\mu\text{J}$ /pulse at a repetition rate of 100 kHz.

The amplified pulses are used to pump two white-light *optical parametric amplifiers* (OPA 9400, Coherent). The OPAs allow for wavelength tunability over the whole visible range (450-700 nm). The tunable wavelengths are accomplished by utilizing difference-frequency generation with the second harmonic pulses and the IR components of the white light pulses generated by the OPAs. The dispersion introduced inside the OPAs is compensated by two double prism-compressors (dispersive medium: BK7) in a standard configuration [73]. The pulses thus obtained show a FWHM of approximately 60-80 fs with an energy of 50 to 100 nJ. They are split with appropriate beam splitters into three independent pulses. The control of the time sequence of these three pulses is realized by two delay stages (OWIS) equipped with retroreflectors indicated in the figure 5.2 by arrows.

The length of the fs-pulses is characterized with an autocorrelator (Femtoscope MC-2, BMI) and the spectral profile is acquired with a combination of a monochromator (SpectraPro 500, Acton) and a CCD detector (LN/CCD512SB, Princeton Instruments). The monochromator allows the spatial separation of the recorded signal into its spectral components, which are simultaneously detected with the help of the multichannel CCD camera. The silicon chip of the CCD camera, which registers the signal, is divided into  $512 \times 512$  pixels, each pixel having the dimensions of  $26 \times 26 \mu\text{m}$ . At a fixed delay time of the time variable laser pulse, a mechanical shutter opens and allows the chip to be exposed for approximately 0,1 to 1 s. The CCD camera integrates over approximately  $10^4$  to  $10^5$  signal shots in the time interval in which the shutter is open. The combination of the CCD camera with the monochromator has the advantage that the whole broad band spectrum of the fs pulse can be recorded at once, in the interval between the moment when the shutter opens and closes, respectively [60]. After the accumulated signal on the silicon chip was read out, the relative timing of the variable laser pulse that introduces the time

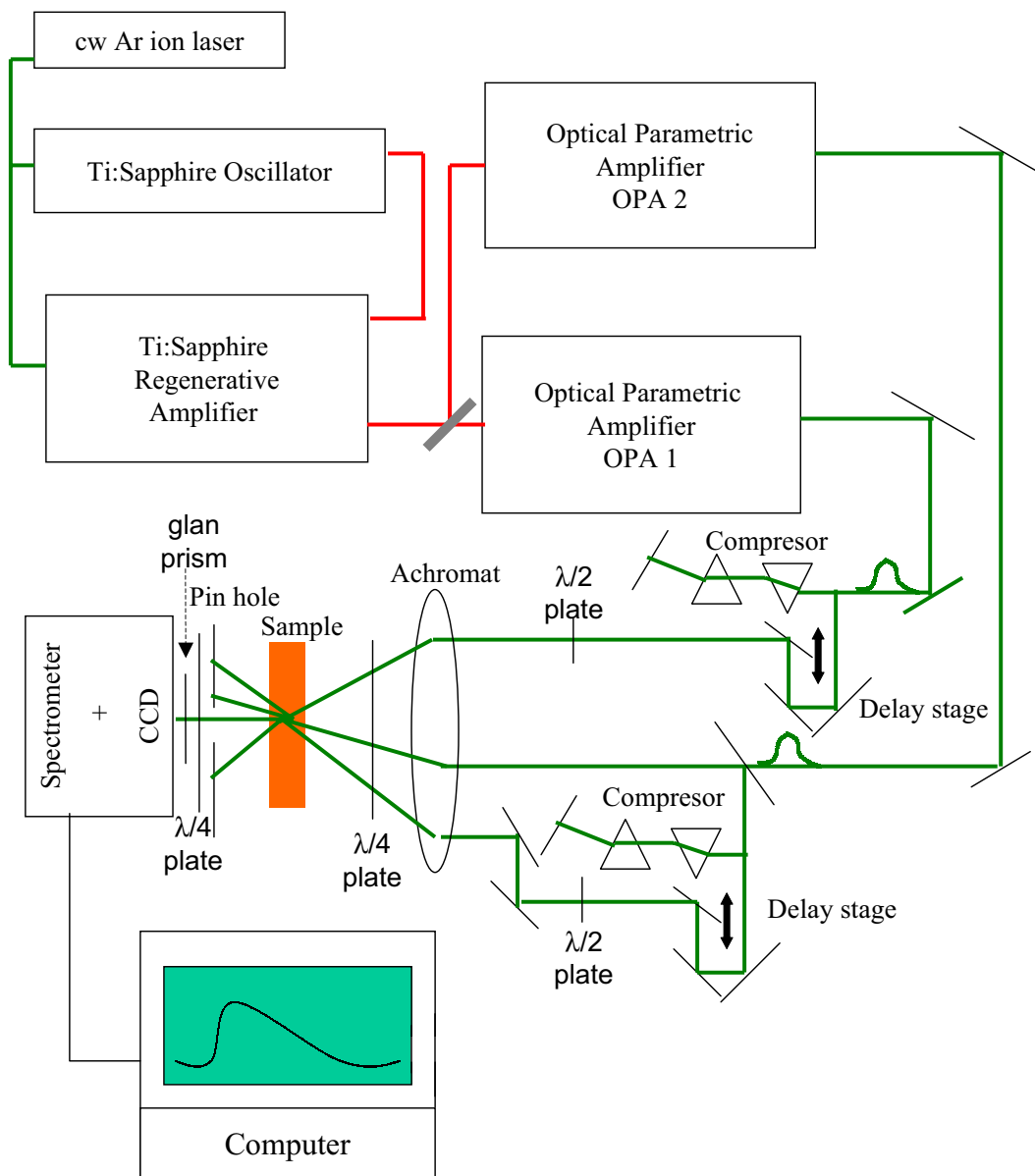


**Fig. 5.1:** Schematic representation of the femtosecond laser system.

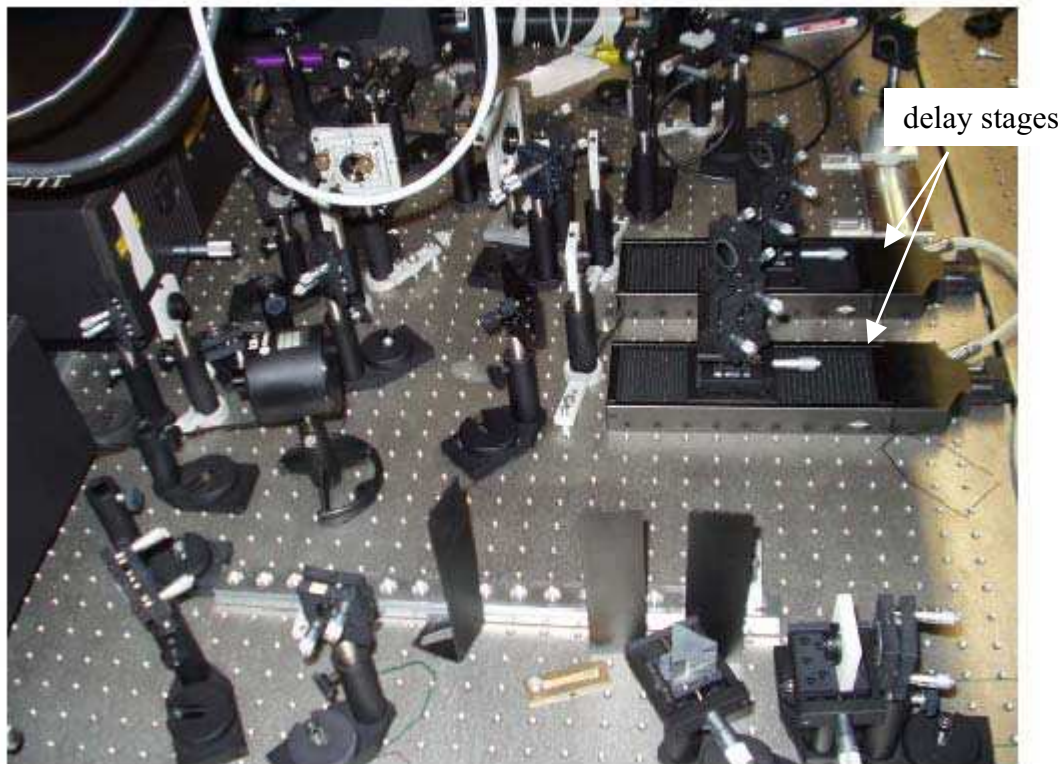


**Fig. 5.2:** Optics involved in the experiment. The two delay stages, which control the time sequence of the femtosecond pulses are indicated by arrows.

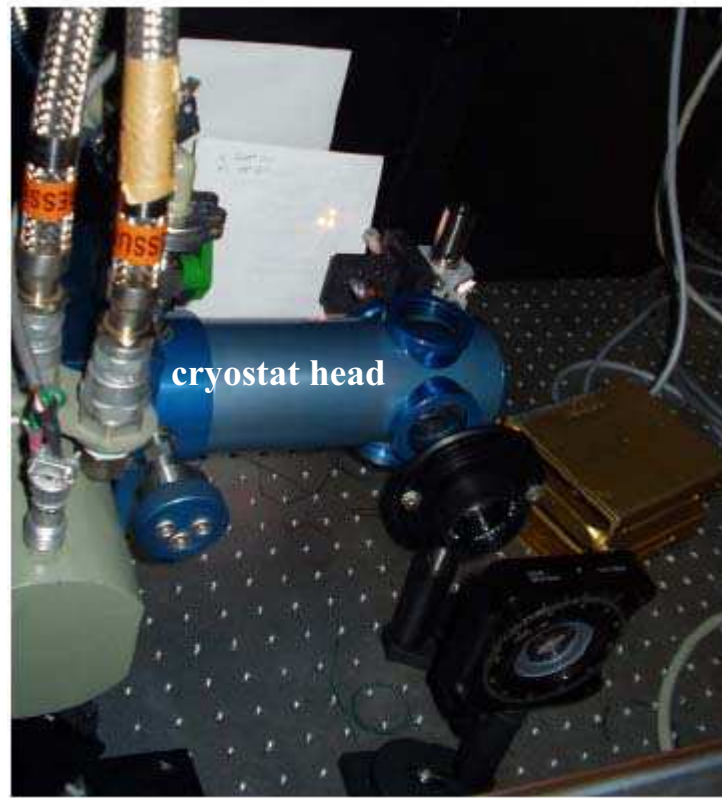


**Fig. 5.3:** Optical cryostat head – Oxford Instruments. Top view.

resolution in the experiment, is moved to a new delay time value and this procedure is repeated for all desired delay times. Thus the whole spectrum of FWM or pump-probe transmission (PPT) signal as a function of the variable delay time of the laser pulses can be obtained.

In the case of both types (FWM and PPT) of experiments, the samples were kept at low temperatures inside a closed cycle He cooled optical cryostat (Oxford Instruments CCC1204). The cryostat head is shown in figure 5.3.

High vacuum ( $7,4 \times 10^{-7}$  Torr) is created inside the cryostat by a turbo-molecular vacuum pump (Pfeiffer TSH 060/TMH 064). The closed cycle He cooler (Cryodrive 3.0 from CTI-Cryogenics Helix Company) allows the control of the temperature in a range from 10 to 300 K. This cryogenic system has the advantage of reduced

windows for maximized optical throughput.

Special attention was paid to the polarization of the incident pulses. The linear polarization of the laser beams was selected to be perpendicular or parallel to the propagation plane by using  $\lambda/2$  plates (achromatic quartz and  $\text{MgF}_2$  retarders, Bernhard Halle Nachfl. GmbH). Circularly polarized pulses are obtained by letting the laser beams pass through  $\lambda/4$  plates (achromatic quartz and  $\text{MgF}_2$  retarders, Bernhard Halle Nachfl. GmbH). The direction of the circular polarization (left  $\sigma^+$  and right hand  $\sigma^-$  circular polarization, respectively) was controlled by using a combination of  $\lambda/2$  and  $\lambda/4$  plates. By recording the FWM and PPT signal, the polarization sensitivity of the spectrometer grating was taken into account by placing both a  $\lambda/4$  and a glan prism in front of the spectrometer's entrance slit.

## 5.2 Phase Matching Condition

In this section, the phase matching conditions needed to generate a degenerate four-wave-mixing (DFWM) and simple pump-probe transmission (PPT) signal will be presented. The experimental setup described in section 5.1 allows the application of different phase matching masks and to vary the number of incident pulses (from 1 to 3 pulses incident on the sample).

For standard FWM measurements, three incident beams with wave vectors  $k_1$ ,  $k_2$  and  $k_3$  in a non-collinear configuration are focused by a lens onto the sample. In order to select the spatially separated scattered FWM signal with a wave vector  $k_s$  a mask is used. Panels a-c. of figure 5.4 illustrate the beam geometry, the phase matching mask (Mask 1) and the wave vector diagram applied for the DFWM measurements, where all three incident pulses have the same wavelength.

The wave vector of the scattered DFWM signal is given by the momentum conservation:

$$k_s = -k_1 + k_2 + k_3. \quad (5.1)$$

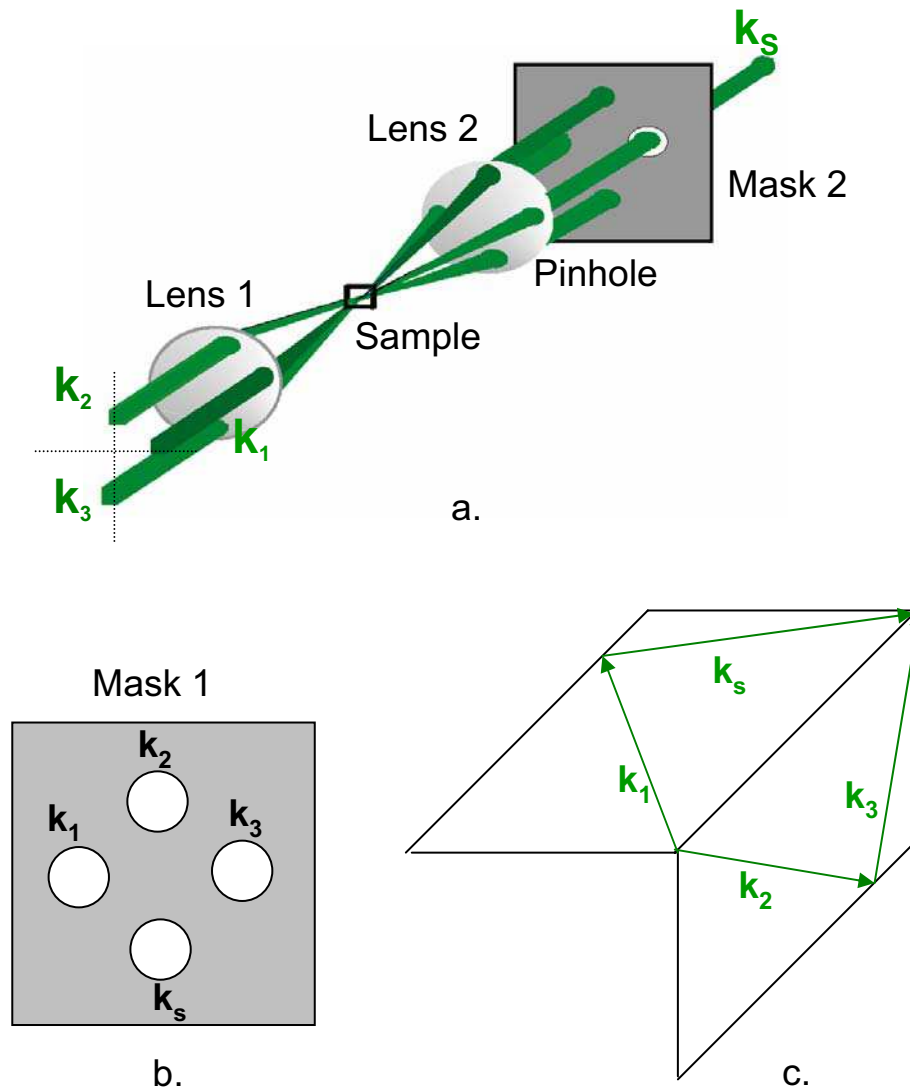


**Fig. 5.4:** **a.** Diagonal view of the beam geometry in DFWM processes (folded BOXCARS arrangement). **b.** Phase matching mask 1, realizing the non-collinear configuration of the three incident beams by letting the laser beams pass through the respective holes of the mask. **c.** Wave vector diagram illustrating the phase matching condition achieved in DFWM measurements.



The chosen beam geometry, depicted in figure 5.4 a., referred to in literature as folded BOXCARS arrangement [74–76], allows for maximum spatial separation of the FWM signal from the incident laser beams. All three non-collinear beams, after they have passed through mask 1, are focused with lens 1 onto the sample. The FWM signal is generated inside the sample and is converted together with the three incident laser pulses into a parallel, non-collinear configuration by lens 2. Applying the second mask, the FWM signal is separated from the incident beams by means of mask 2. Thus the folded BOXCARS arrangement allows the background free detection of the scattered FWM signal.

In the case of simple femtosecond pump–probe measurements, only two incident pulses were involved: a pump pulse  $k_p$  and a probe (test) pulse  $k_T$ . As shown in section 4.2.3, the pump–probe signal can be seen as the diffraction of the probe pulse on the population grating created by the pump:

$$k_s = -k_p + k_p + k_T = k_T. \quad (5.2)$$

Thus the pump–probe signal is propagating in the direction given by the wave vector of the probe pulse  $k_s = k_T$ . By recording the changes in the probe pulse, as theoretically derived in section 4.2.3 information about different dynamical processes of the system can be obtained.



## 6 Biexciton and Spin Dephasing Effects Proved by four-wave-mixing and Pump-Probe Spectroscopy

*This chapter demonstrates the complementarity of linear and nonlinear spectroscopy methods for the characterization of semiconductor quantum dots embedded in a dielectric matrix. In chapter 3 the key-properties of the QDs like their size and the inhomogeneously broadened size distribution were determined. This section includes nonlinear spectroscopy studies on semiconductor nanoparticles. In particular, femtosecond four wave mixing (FWM) and pump-probe transmission experiments were performed on QDs of different sizes.*

*By analyzing the polarization properties of the time integrated four-wave-mixing (TI-FWM) and pump-probe transmission (PPT) signal, valuable information about the QD's energy structure is obtained. The experimental setup allows to individually select and vary the polarization of the incident laser pulses and to generate various polarization geometries. It will be shown, that the appearance of strong TI-FWM signals in forbidden polarization geometries according to the non-interacting oscillators' model, is due to a strong exciton-exciton coupling inside the same QD and to the inhomogeneous spin dephasing of the QD excitons due to a random exchange splitting of the  $J = 1$  exciton state, originating in the lowered QD symmetry.*

*Similar depolarization effects observed for the DTS signals in the case of pump–probe experiments validate the results obtained from FWM measurements, the intensity of the DTS signal being the square root of the TI-FWM signal [48].*

## 6.1 Exciton–Exciton Coupling in CdS<sub>0.6</sub>Se<sub>0.4</sub> Quantum Dots

In this section, the polarization properties of one of the samples discussed in chapter 3 will be presented. The QD system studied here consists of CdS<sub>0.6</sub>Se<sub>0.4</sub> nanoparticles embedded in a glass matrix. The chemical composition of the nanocrystals was determined by the group of Dr. M. Ivanda at the Ruder Boskovic Institute in Zagreb, Croatia. The mean diameter of the investigated QDs is 9.1 nm with a size distribution of 15% were determined in chapter 3. The volume fraction of QDs in the glass counts 1%. The sample is manufactured by Schott Inc. in Mainz and commercially available under the name OG550.

The sample was mounted into an optical cryostat described in section 5.1 and kept during the FWM and pump–probe experiments at a temperature of 10 K. Figure 6.1 displays the absorption spectrum for the investigated QD system at a temperature of 10 K. Depending on the experiment (TI-FWM or pump–probe spectroscopy) three or two incident 80-fs laser pulses were used for excitation, respectively. For all pulses the same excitation energy was chosen (corresponding to 510 nm), lying in the range of inhomogeneously broadened  $1s - X$  exciton transition (figure 6.1).

The dynamics of the QD system was first investigated by three pulse photon echo spectroscopy. This is a FWM technique used in the framework of transient gratings, which avoids the inhomogeneous broadening of oscillators' energies because the integrated photon echo signal reflects the average properties of nanoparticles within the inhomogeneous distribution [48]. Three pulse photon echo was preferred

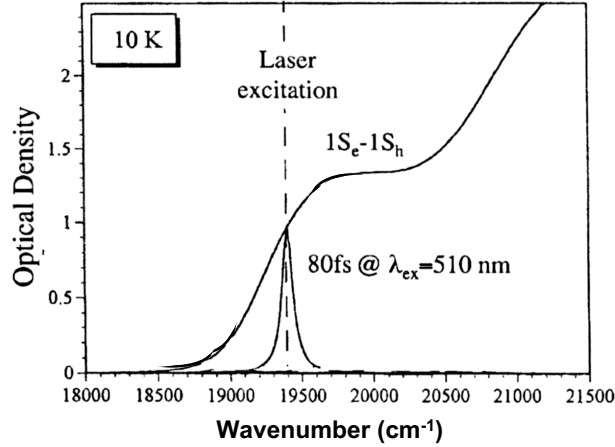


**Fig. 6.1:** Absorption spectrum recorded for  $CdS_{0.6}Se_{0.4}$  QDs of 9.1 nm in diameter, embedded in a glass matrix.

to two pulse photon echo in order to be able to individually control the polarization of the incident laser pulses. In the experiments presented below, all three pulses were circularly  $\sigma^+$  or  $\sigma^-$  polarized. The notations  $\sigma^+$  and  $\sigma^-$  stand for left and right hand circular polarization of the beams, respectively. Propagating in the directions given by their wave vectors  $k_1$ ,  $k_2$  and  $k_3$ , the laser pulses are incident on the sample under an angle of incidence of about  $5^\circ$  and the photon echo signal is scattered in the direction given by the phase matching condition (section 5.2):

$$k_s = -k_1 + k_2 + k_3 \quad (6.1)$$

In the following it will be referred to the TI-FWM signals in different polarization geometries as  $I^{ijkl}$ , where  $I$  is the intensity of the recorded signal and the indexes  $i$ ,  $j$ ,  $k$  and  $l$  equal to  $+$  or  $-$  represent the  $\sigma^+$  or  $\sigma^-$  polarization of the electric fields of the pulses with wave vectors  $k = k_1, k_2, k_3$  and  $k_s$ . The time sequence of the pulses was selected to be zero for the first two (in time) incident pulses ( $t_{21} = t_2 - t_1 = 0$ ) and the FWM signal was recorded as a function of the delay time  $t_{31} = t_3 - t_1$  between the third pulse and the two time coincident pulses. This corresponds to a diffraction of the electric field  $E_3$  of the third pulse, for positive  $t_{31}$  delay times, on

the population grating created through the interference of the pulses  $E_1$  and  $E_2$  in the sample space. In this geometry, the TI-FWM signal is a direct measure of the population dynamics.

Figure 6.2 displays the three pulse photon echo signal recorded for the 9.1 nm mean diameter QDs ensemble embedded in a glass matrix at 10 K for different polarization geometries of the electric fields of the incident laser pulses. The polarization selection rules for a system of non-interacting oscillators (NIO) predict a non-zero TI-FWM signal only for the case when all incident pulses have the same polarization [48]. Figure 6.2 proves that indeed the strongest signal appears for pulses having the same  $\sigma^+$  polarization, the intensity of  $I^{++++}$  at  $t_{31} = 0$  being the highest. In contrast to the NIO model, the experiment shows at  $t_{31} = 0$  strong signals for two other polarization configurations  $I^{++--}$  and  $I^{+-+-}$ . The rapid decrease in intensity of  $I^{+-+-}$ , as it will be shown in the section 6.2, is due to the difference in the gratings created by the first two pulses. The appearance of other FWM signals in forbidden polarization geometries (according to the NIO model) is due to depolarization effects (the intensity of the signal in forbidden geometries is one order of magnitude smaller) and/or to lowering of the symmetry of the QDs but unfortunately they yield no valuable information for this study.

In the following, a qualitative study of the electronic properties of such a confined system will be presented by focusing on the time behavior of the TI-FWM signals recorded under two specific configurations of the incident pulses, namely the allowed  $I^{++++}$  and forbidden  $I^{++--}$  configuration according to NIO model. For clarity, these two signals are plot once more in figure 6.3 together with the time behavior of the sum and the difference between  $I^{++++}$   $I^{++--}$  as a function of  $t_{31}$ . With increasing  $t_{31}$ ,  $I^{++++}$  first decreases in intensity by a factor of 2 in the first  $t_{31} \approx 5$  ps, afterwards its decay time decreases drastically and exceeds 100 ps. The behavior of  $I^{++--}$ , forbidden according to the NIO model is quite different.  $I^{++--}$  corresponds to scattering of  $\sigma^-$  polarized light on the population grating created by two  $\sigma^+$  polarized beams. Its intensity first even increases in the first  $t_{31} \approx 5$  ps and only

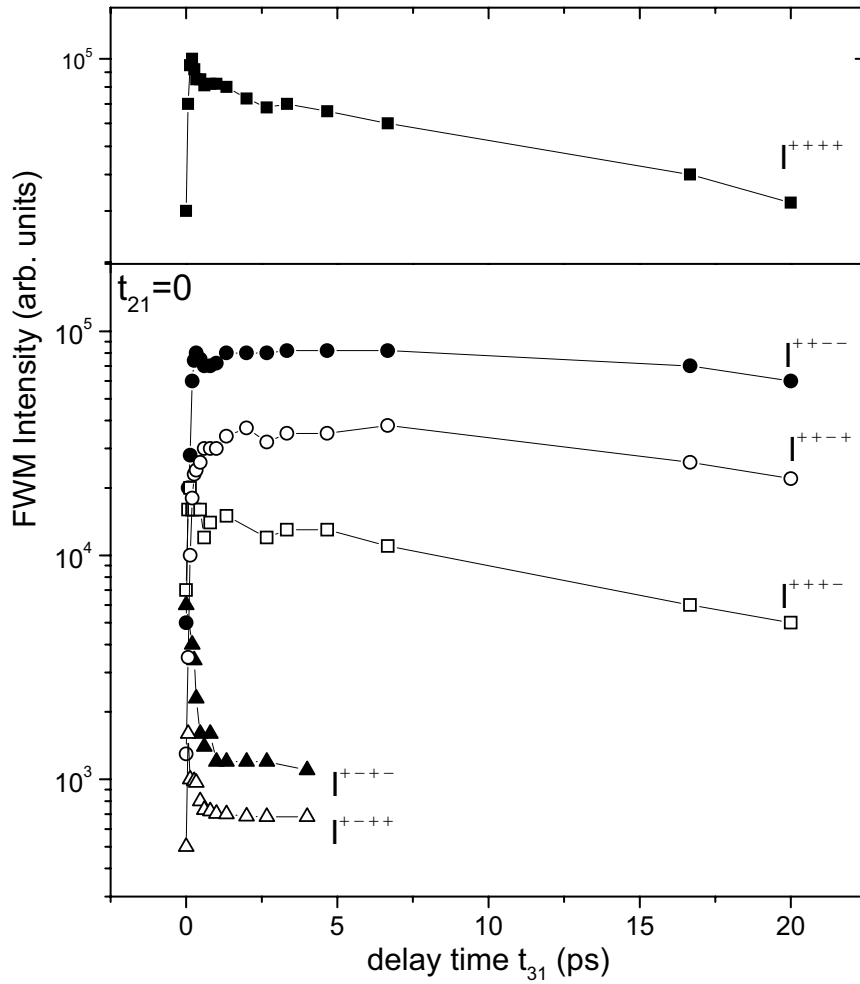


**Fig. 6.2:** Time integrated photon echo for different polarization geometries of the incident beams recorded as a function of the delay time  $t_{31}$ . The data are plotted on a logarithmic scale. The transient recorded with all laser pulses having the same polarization  $I^{++++}$  is vertically shifted for clarity.

after that it decays with the same time constant as  $I^{++++}$ .

A similar depolarization effect was observed in the case of pump–probe transmission (PPT) measurements. The intensity of the differential transmission signal (DTS) should be the square root of the intensity of the FWM signal [48]. The DTS spectra recorded for OG550 under two different polarization geometries are shown in figure 6.4. It is noticeable that the  $\sigma^+$  polarized pump pulse influences the transmission of both  $\sigma^+$  and  $\sigma^-$  polarized probe pulses, and the behavior of the DTS  $I^{++}$  and  $I^{+-}$  is quite similar to that of the FWM signals  $I^{++++}$  and  $I^{++--}$ , respectively.  $I^{++}$  shows first a fast decay, then its decay time exceeds 100 ps, whereas  $I^{+-}$  first increases and only afterwards decreases with the same decay time as  $I^{++}$ . Thus the DTS results are in agreement with the TI-FWM experiments.

In order to explain the unexpected time behavior of FWM–signal and PPT signal, the electronic structure of the QDs has to be considered [1–4, 33, 77]. As shown in figures 2.5 and 2.6, the 3D confinement of electrons and holes results in a strong quantization of their states. The lowest exciton state  $1s - X$  is formed mainly by the electron and the hole in the ground ( $1s$ ) QD confined states with the total spin  $J = \frac{1}{2}$  and  $\frac{3}{2}$ , respectively. In a spherical dot, which presents a wurtzite lattice structure, the electron–hole exchange interaction splits the  $1s - X$  state into a set of states with spins equal to 1 and 2 [1–3]. The exciton ground state with spin 2 is optically passive in the dipole approximation, because emitted or absorbed photons cannot have an angular momentum projection  $\pm 2$ . This state with  $J = 2$  is known in the literature as "dark exciton state" [1–3]. The lowest optically active state is a  $J = 1$  spin doublet. However, if the QD's symmetry is reduced to  $C_{2v}$  or lower, the  $J = 1$  doublet splits further into two states with the corresponding ket vectors:  $|X \rangle = \frac{|1\rangle + |-1\rangle}{\sqrt{2}}$  and  $|Y \rangle = \frac{|1\rangle - |-1\rangle}{\sqrt{2}}$ . These two states are optically active in mutually orthogonal linear polarizations [5, 6]. The energy splitting of these states  $\Delta$  is usually rather small, in the range of 1 meV.

In QDs with cubic symmetry, the Fs  $\sigma^+$  polarized beam excites the pure X (exciton) state  $|+1\rangle$ , whereas in a nanodot of lower symmetry it excites a linear



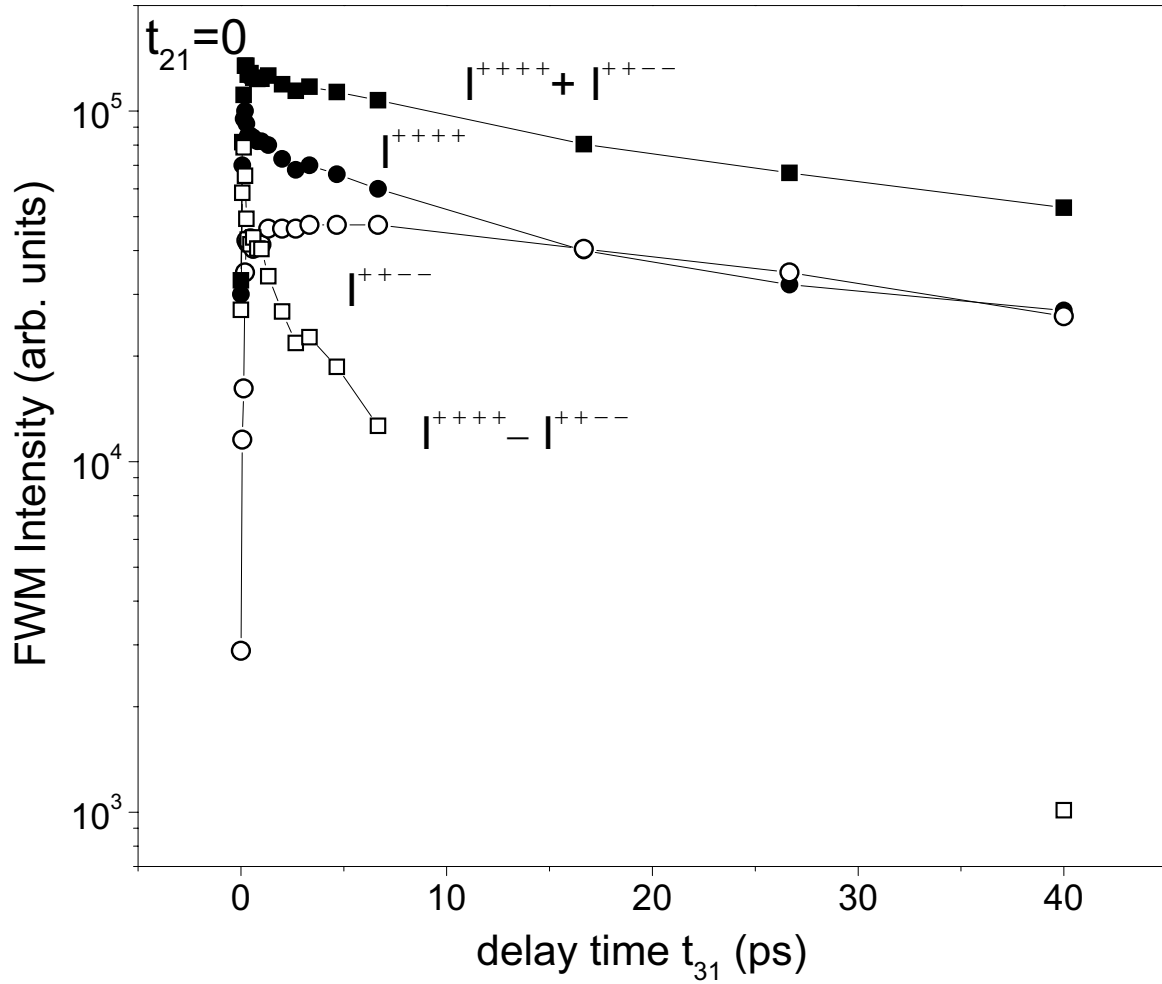


**Fig. 6.3:** Dependence of the time integrated photon echo in the  $I^{++++}$  and  $I^{++--}$  configuration, of the sum  $I^{++++} + I^{++--}$  and of the difference  $I^{++++} - I^{++--}$  on the delay time  $t_{31}$ . The data are plot on a logarithmic scale.

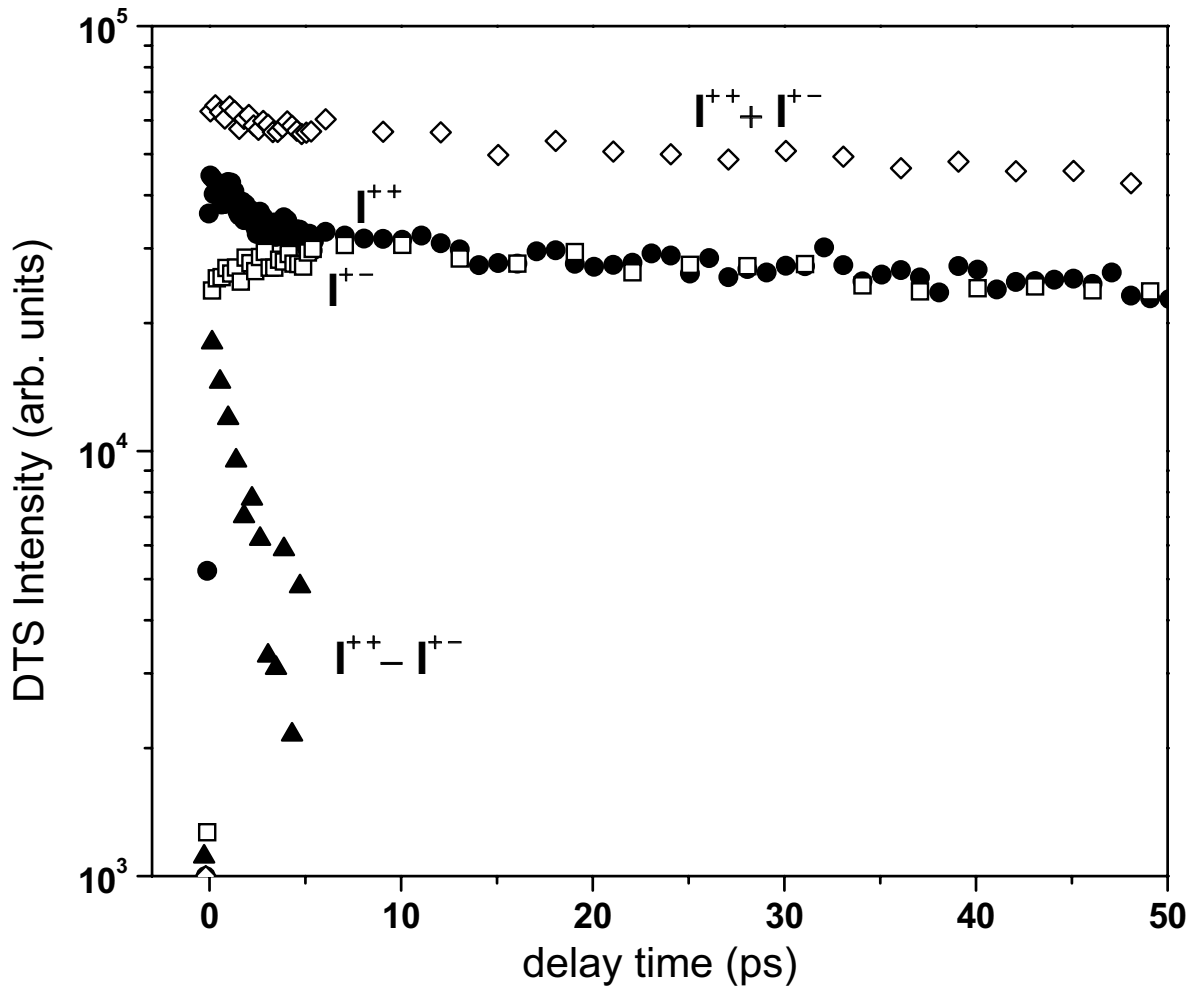


**Fig. 6.4:** Differential Transmission Signal (DTS) recorded in  $I^{++}$  and  $I^{+-}$  configuration as a function of the delay time between the two pulses  $t_{21}$ . The sum  $I^{++} + I^{+-}$  and the difference  $I^{++} - I^{+-}$  are also plot. The data are plot on a logarithmic scale.

combination of  $|X\rangle$  and  $|Y\rangle$  states. In the case of lower symmetry QDs, the energy difference between the states marked  $|X\rangle$  and  $|Y\rangle$  leads to spin precession. However, the effect of the latter can be neglected for delay times  $t_{31}$  much smaller than  $2\pi\hbar/\Delta$ . For the investigated sample, this time is in the order of 3 ps (as it will be shown later) and thereby the splitting can be neglected for delay times  $t_{31}$  below 1 ps.

In order to explain the strong signal in forbidden polarization geometries (according to the NIO model) one has to take into account the exciton–exciton interaction [48]. The volume fraction of the QDs is 1%, thus the Coulomb interaction between excitons belonging to different QDs can be neglected due to the large separation between the nanoparticles. In contrast, the Coulomb interaction between excitons belonging to the same QD is very strong, due to the electron–hole confinement. As a result:

1. an excitation of two  $1S$  excitons with the same spin in the same QD is forbidden according to Pauli principle;
2. the excitation of the first  $|+1\rangle$  exciton causes a marked decrease in the photoexcitation energy of the second  $|−1\rangle$  exciton in the same QD.

The decrease in photoexcitation energy of  $|−1\rangle$  excitons as consequence of photoexcitation of  $|+1\rangle$  excitons results in a change of the dielectric function and leads to the appearance of PPT signal  $I^{+-}$  and to the scattering of a  $\sigma^-$  polarized beam on the polarization grating created by two  $\sigma^+$  polarized pulses ( $I^{++--}$ ), forbidden according to the noninteracting oscillators model (NIO).

The appearance of the PPT and FWM signals in forbidden polarizations ( $I^{+-}$  and  $I^{++--}$ ) is explained in the framework of the four-level model (figure 2.5 and figure 2.6) including a ground state, two X states of opposite polarizations ( $|+1\rangle$  and  $|−1\rangle$ ) and a singlet two–exciton (biexciton) state. A  $\sigma^+$  polarized pulse can only excite excitons with positive spins, i.e.  $J = |+1\rangle$ , the excitation of  $J = −1$

excitons being possible only with  $\sigma^-$  polarized pulses. Here, two interfering  $\sigma^+$  polarized pulses create in the sample a density grating in the  $1s^+ - X$  state, noted  $\rho_{++}$ , where the sign "+" indicates the spin  $J = +1$  of the exciton. Considering the total density grating created in the sample as being equal to 1, the density grating created in the ground state is given by the difference:

$$\rho_{00} = 1 - \rho_{++}. \quad (6.2)$$

In the  $1s^- - X$  exciton or in the biexciton states no density grating appears ( $\rho_{--} = 0$ ). The absorption (refraction) is proportional to the difference:

$$\rho_{00} - \rho_{++} = [1 - \rho_{++}] - \rho_{++} = 1 - 2\rho_{++} \quad (6.3)$$

for  $\sigma^+$  polarized light. For a  $\sigma^-$  polarized beam, the absorption is proportional to the difference:

$$\rho_{00} - \rho_{--} = [1 - \rho_{++}] - 0 = 1 - \rho_{++}. \quad (6.4)$$

This model predicts a maximum ratio 1 : 2 for  $I^{+-} : I^{++}$  in the PPT measurements. The intensity of the FWM signal is squared with respect to the DTS intensity [48]. This results in a ratio of 1 : 4 for the photon echo signals  $I^{++--} : I^{++++}$ . As it will be shown later, the investigated QDs have a relatively low symmetry and a random orientation in the glass matrix. Thereby, one can expect a relaxation of the selection rules. Indeed, the polarization dependence relaxes in absorption measurements. However, the influence of the random orientation of nanoparticles on the selection rules in PPT and FWM measurements is much weaker [1, 77]. This is due to the predominant excitation of QDs with a quantization plane perpendicular to the pump beam, when the electric field of the pump pulse is parallel to the QD's polarization plane.

To estimate the effect of the orientational induced disorder on the DTS and FWM signals, calculations in the limit of the 4-level model and of the random distribution

**Table 6.1:** Relative DTS signal for different polarizations of the pump and the probe laser beams

$\sigma_{pump}\sigma_{probe}$	$I^{ij}$		$I^{ij}/I^{++}$		
	NO	RND	NO	RND	RND-NO
+ +	2.000	0.933	1.000	1.000	0
+ -	1.000	0.600	0.500	0.643	0.143

of noninteracting  $J = 1$  exciton oscillators were performed. In this approximation, the QDs have a cylindrical symmetry and their polarization in the direction of a cylindrical axis is zero [77]. Therefore, only the in-plane component of the electric field has to be considered for the corrections to the density matrix  $\rho^{(2)}$  (eq. 4.14) for the case of DTS measurements and  $\rho^{(3)}$  (eq. 4.15) for the case of the FWM experiments, respectively. The results of the calculations are presented in the tables 6.1 and 6.2 for the pump-probe and FWM measurements, respectively. Here, the following notations were used: NO stays for the normal orientation of the QD's symmetry axes (like coins on the table), whereas RNO represents the situation when the normals of the QDs are randomly oriented in the ensemble.

The orientational induced disorder (see table 6.1) was found to lead to relatively weak changes in the relative intensities of the DTS and FWM signals in  $I^{+-}$  and  $I^{++--}$  geometries, respectively. However, the orientational induced disorder does not predict the appearance of any signals in the forbidden FWM geometries  $I^{++++}$ ,  $I^{+++}$ ,  $I^{++}$  and  $I^{+-}$ .

The 4 level model predicts for oriented QDs the maximum ratio 1 : 2 for  $I^{+-} : I^{++}$  in the PPT measurements and the ratio 1 : 4 for the photon echo signals  $I^{++--} : I^{++++}$ . The orientational induced disorder in QDs predicts only small changes in the ratios:  $I^{++--}/I^{++++} \approx 0.41$  for FWM (see table 6.2) and  $I^{+-}/I^{++} \approx 0.64$  for DTS (see table 6.1). However, the experiment shows that the intensity of the

**Table 6.2:** Relative FWM signal in the direction  $-k_1 + k_2 + k_3$  for different polarizations of the incident laser beams

$\sigma_1\sigma_2\sigma_3\sigma_s$	$I^{ijkl}$		$I^{ijkl}/I^{++++}$		
	NO	RND	NO	RND	RND-NO
++++	4.000	0.871	1.000	1.000	0
+++−	0	0	0	0	0
++−+	0	0	0	0	0
++−−	1.000	0.360	0.250	0.413	0.163
+−++	0	0	0	0	0
+−+−	0	0	0	0	0

PPT ( $I^{++}$  and  $I^{+-}$ ) and FWM ( $I^{++++}$  and  $I^{++--}$ ) signals in the allowed and forbidden polarization geometries are almost the same after longer delay times  $t_{31}$  (see fig.6.3 and fig.6.4). Therefore, the orientational induced disorder cannot be alone responsible for the appearance of the DTS and FWM signals in forbidden polarization geometries and the strong X-X interactions cannot be neglected for excitons belonging to the same QD.

To summarize, it was shown, that the orientational disorder does not disturb the polarization selection rules and the appearance of strong DTS ( $I^{+-}$ ) and FWM ( $I^{++--}$ ) signals in forbidden geometries is well explained by the four level model taking into account the strong  $X - X$  coupling in the QD, thus proving the existence of biexciton states. The orientational disorder does not disturb the polarization selection rules and leads only to a relatively small changes in the relative intensities of the signals recorded under various allowed polarization geometries.

## 6.2 Spin Dephasing in 3D Confined Systems

In order to study spin dephasing effects in QDs, the behavior of the  $I^{++--}$  and  $I^{+-+-}$  FWM signals (figure 6.2) recorded in forbidden polarization geometries – according to NIO model – will be discussed. Although the time behavior of  $I^{++--}$  and  $I^{+-+-}$  in quantum well (QW) structures is rather similar [78], in the case of 3D confined carriers significant discrepancies have been observed (figure 6.2).

The time behavior of  $I^{+-+-}$  is quite different from  $I^{++--}$ . The intensity of  $I^{+-+-}$  decreases rapidly by two orders of magnitude and becomes almost zero for  $t_{31} > 400$  fs, i.e. when the temporal overlap of the pulses with the wave vectors  $k_2$  and  $k_3$ , creating the grating, disappears. The observed equality in intensities of  $I^{+-+-}$  and  $I^{++--}$  at zero time  $t_1 = t_2 = t_3 = 0$  is expected because the spatial direction of the FWM signal is symmetric under the interchange of the first two (in time) pulses  $k_1$  and  $k_2$ . The difference between the pulses  $k_2$  and  $k_3$  for time delays  $t_{32} = t_{31} \neq 0$  is connected to the fact that the second (in time) pulse interferes in the sample space with the first (in time) pulse and forms thus the population grating, while the third pulse  $k_3$  is scattered onto this grating according to the Bragg condition. Therefore, the huge difference in the decay behavior of  $I^{++--}$  and  $I^{+-+-}$  indicates the qualitative difference in the gratings created by the pulses  $k_1$  and  $k_2$  having the same (both  $k_1$  and  $k_2$  being  $\sigma^+$  polarized) and opposite polarizations ( $k_1$  being  $\sigma^+$  and  $k_2$   $\sigma^-$  polarized), respectively.

The grating created in the sample space by two  $\sigma^+$  polarized laser pulses is a population grating which decays with the exciton lifetime  $T_1$ , which in the case of the QDs under discussion is rather long and leads to a long decay time of both  $I^{++++}$  and  $I^{++--}$ . Such a grating is obviously absent for orthogonal polarizations of the laser beams. In this case only a polarization grating is created in the sample volume. The pulses  $k_1$  ( $\sigma^+$  polarized) and  $k_2$  ( $\sigma^-$  polarized) thus excite linearly polarized states ( $|X \rangle$  and  $|Y \rangle$ ) with an electric vector precessing with a period of  $1/(|k_1 + k_2|)$ . The properties of such a polarization precession grating are qualitatively different

from those of a population grating created by pulses having the same polarization.

First of all, the polarization vector's precession leads to a very specific scattering: the scattering occurs by changing the circular polarization of the incident beam to the opposite one. In addition, the direction of the scattering depends on the polarization of the third (in time) beam, which is scattered on the polarization grating. Therefore, a  $\sigma^+$  polarized beam is scattered in the direction  $-k_1 + k_2 + k_3$  and this signal is  $\sigma^-$  polarized, whereas a  $\sigma^-$  beam scatters into  $\sigma^+$  in the direction  $k_1 - k_2 + k_3$ . Finally, the decay of this grating is determined by its dephasing, which occurs at times much shorter than  $T_1$ , resulting in a very fast decay of  $I^{+--+}$ . These predictions are in qualitative agreement with the experiment. First, as shown in figure 6.2, the  $\sigma^+$  polarized  $k_3$  scatters in the direction  $-k_1 + k_2 + k_3$  and the signal is highly  $\sigma^-$  polarized. Second, no marked scattering of a  $\sigma^-$  polarized  $k_3$  beam in this direction is observed. Moreover,  $I^{+--+}$  is lower in intensity as  $I^{+--+}$ . By analyzing figure 6.2, it becomes much clearer that this scattering process by changing the polarization of the third pulse  $k_3$  into the opposite one is only characteristic to polarization gratings: the intensity of  $I^{+++-}$  is one order of magnitude smaller in comparison to  $I^{++++}$ , while the same dependence in relative intensities is observed for  $I^{+--+}$  in comparison to  $I^{++--}$ . Finally, in contrast to  $I^{++++}$ , the decay time of  $I^{+--+}$  is only about 200 fs. The latter is similar to the exciton dephasing time, determined separately in another FWM geometry, where  $k_2$  and  $k_3$  were overlapped in time and the signal was recorded as a function of the delay of  $k_1$  (figure 6.5). As a reference, a glass plate showing no dynamics was used. The perfect correspondence of the two transients (from glass and QDs, respectively) suggests that the exciton dephasing time of QDs is equal or shorter than the time resolution of our system (50 fs). As shown in section 4.2.3 using eq. 4.36, the intensity of TI-FWM signal is directly proportional to  $T_2/4$  for inhomogeneous systems, leading to a spin dephasing time of  $T_2 \approx 200$  fs.

Therefore, the drastic difference between the time behavior of  $I^{+--+}$  and  $I^{++--}$  is well explained by the four-level model.



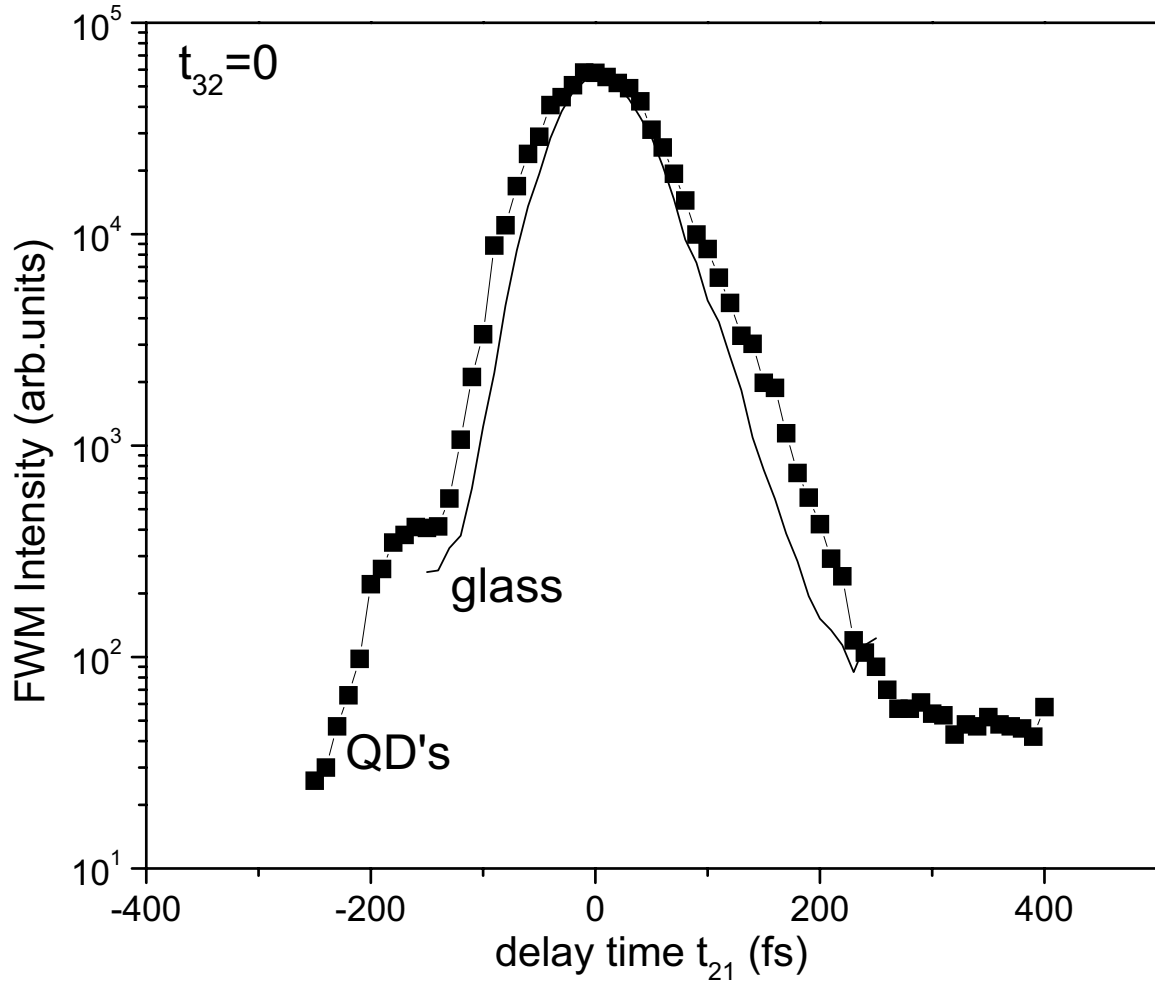


**Fig. 6.5:** FWM signal  $I^{++++}$  recorded with  $k_2$  and  $k_3$  overlapped in time ( $t_{32} = 0$ ), the transient being recorded as a function of  $t_{21}$  in the direction given by the phase matching condition  $k_s = k_1 - k_2 + k_3$ . The data are plot on a logarithmic scale. The experimentally recorded points are represented by symbols connected by a solid line. The spectrum recorded for the reference (glass plate) is marked only by a solid line and is vertically shifted for clarity.

For a closer analysis of the spin dephasing process in QDs, the behavior of the TI-FWM signals  $I^{++++}$  and  $I^{++--}$  has to be carefully studied. In both cases, the FWM signal is a result of scattering a  $\sigma^-$  polarized pulse on the population grating created by two  $\sigma^+$  polarized pulses. However, their temporal behavior is different for small  $t_{31}$  delay times ( $I^{++++}$  decreases in intensity, whereas  $I^{++--}$  first even increases in intensity) and the difference disappears only at  $t_{31} > 5$  ps (figure 6.3). A similar behavior is observed in figure 6.4 for the PPT signals:  $I^{++}$  decreases, whereas  $I^{+-}$  increases in intensity for the first  $\approx 5$  ps. It is natural to suppose that the difference in the temporal behavior of  $I^{++++}$  and  $I^{++--}$  is due to the spin dephasing process taking place at early delay times. For  $t_{31} > 5$  ps the density grating is already spin dephased and a FWM signal decay time of  $\tau_1 \approx 80$  ps is determined resulting in a lifetime  $T_1 = 2\tau_1 \approx 160$  ps for the bright QD exciton.

A similar value for the exciton lifetime  $T_1 \approx 180$  ps can be extracted from the PPT signal in figure 6.4. Moreover, the sum of  $I^{++}$  and  $I^{+-}$  shown in figure 6.4 displays the same decay time in the whole range of delay times exceeding 0.3 ps. A similar behavior is observed for the sum of  $I^{++++}$  and  $I^{++--}$  in figure 6.3. That is an additional proof that the changes both in the PPT signals  $I^{++}$ ,  $I^{+-}$  and in TI-FWM signals  $I^{++++}$ ,  $I^{++--}$  for early delay times are connected to an exciton spin dephasing process. Moreover, the dominating dephasing seems to occur just between the two bright exciton states with  $J = 1$  and does not include scattering into the dark exciton states with  $J = 2$ . That allows one to neglect phonon assisted spin flip processes, which result mainly in the conversion of bright exciton into dark ones, having the characteristic time in the ns regime [77].

One of the most effective mechanisms of the spin dephasing between two  $J = 1$  states is connected to their splitting due to a lowered QD symmetry. The splitting causes a spin precession in excitons generated by circularly polarized light with a rate  $\frac{\Delta}{2\pi\hbar}$ , where  $\Delta$  is the difference in energies between the two exciton states (X) under discussion ( $J = \pm 1$ ). In a system of homogeneously split Xs, with the same value of  $\Delta$  in all QDs such a precession would lead to quantum beats in the population

densities  $\rho_{++}$  and  $\rho_{--}$ . The system under study obviously exhibits inhomogeneously split Xs, therefore medium population densities have to be considered:  $\langle \rho_{++} \rangle$  for X states with  $J = +1$  and  $\langle \rho_{--} \rangle$  for X states with  $J = -1$ . The fluctuations in  $\Delta$  lead to spin dephasing and result in decreasing difference between  $\langle \rho_{++} \rangle$  and  $\langle \rho_{--} \rangle$  [79]. As a result  $\langle \rho_{++} \rangle$  decreases and  $\langle \rho_{--} \rangle$  increases in time till a mean value ( $\approx \rho_{++}(t_{31} = 0)/2$ ) is achieved. This causes an increase in intensity of the FWM signal  $I^{++--}$  and PPT signal  $I^{+-}$  for early delay times  $t_{31}$  and, vice versa, the fast decrease in intensity of  $I^{++++}$  and  $I^{++}$ . The observed spin dephasing time (also separately determined from the difference between  $I^{++++}$  and  $I^{++--}$  in figure 6.3) is about 1 ps indicating that  $\Delta$  in our sample fluctuates in the range of  $\approx \pm 1$  meV. It is important to note that this dephasing time is not a real spin dephasing time ( $T_2$  being determined as  $\approx 200$  fs) but a spin dephasing connected to the lowered symmetry of the nanoparticles.

In conclusion, the investigations of the polarization properties of the TI-FWM and PPT signals have shown that the relaxation of selection rules due to orientational disorder in QDs is relatively weak. The strong scattering of a  $\sigma^-$  polarized light on the population grating created by two  $\sigma^+$  polarized pulses and the strong  $I^{+-}$  PPT signal appear due to a strong X–X coupling in the nanoparticles. The spin dephasing of a  $\sigma^+$  population grating leads to the disappearance of the difference in  $I^{++++}$  and  $I^{++--}$  signals for long delay times, determining a population lifetime of  $T_1 \approx 180$  ps. No marked population grating is created by two pulses having opposite ( $\sigma^+$  and  $\sigma^-$ ) polarizations. In this case the grating is determined by the polarization vector's precession and decays with the exciton dephasing time  $T_2 \approx 200$  fs. Moreover, the splitting in energy between the exciton levels  $J = 1$  could also be estimated indicating a lowered symmetry of the nanoparticles. Furthermore, ultrashort processes in such confined systems are studied by applying nonlinear spectroscopy techniques, like TI-FWM and DTS involving circularly polarized laser pulses.

## 7 Degree of Asymmetry of Nanoparticles Embedded in Dielectric Matrix

*As already introduced in chapter 6, the polarization properties strongly depend on the internal and crystal shape asymmetries, and not only on the changes in the energy distribution due to strong electron–hole exchange interaction. This chapter deals with detailed investigations of the nanoparticles’ symmetry. The aim is to determine the net splitting parameter  $\Delta$  of the energy levels, which is a direct measure of the QD’s asymmetry, using the TI-FWM technique with circularly polarized light.*

*A comparison between polarization properties of commercially available  $\text{CdS}_{0.6}\text{Se}_{0.4}$  QDs and heat treated CdSe QDs embedded in a dielectric matrix is performed. Nanoparticles of different sizes and/or the same size but grown under different conditions are investigated in order to determine the optimal growth conditions for obtaining high quality QDs with the highest symmetry achievable. The spin dephasing effects and exciton lifetimes for ground- and excited states of electron–hole pairs are intensively discussed. It will be shown that samples containing nanoparticles of the same size, but grown under different conditions exhibit different exciton spin dephasing times and consequently different asymmetries. Finally, ultrafast relaxation paths and the role of Auger processes in the relaxation mechanisms in quantum confined systems will be discussed.*

## 7.1 Influence of Growth Conditions on the Exciton Spin Dephasing

As already shown in chapter 6, the electron–hole interactions play a crucial role in all processes in QDs. In particular, the electron–hole interaction (in CdS and CdSe QDs) splits the lowest exciton state, formed by the electron having a spin of  $J = 1/2$  and by the hole with a spin  $J = 3/2$ , into a set of states with  $J = 1$  and 2 [3, 77]. The lowest optically active state (spin doublet with  $J = 1$ ) is split further due to lowering of the QD’s symmetry into two states with  $J = \frac{|+1\rangle+|-1\rangle}{\sqrt{2}}$  and  $J = \frac{|+1\rangle-|-1\rangle}{\sqrt{2}}$ , optically active in mutually orthogonal linear polarizations [6]. Moreover, the random exchange splitting of the  $J = 1$  exciton state, which leads to the depolarization of the DTS and FWM signals, originates from the lowered symmetry of the nanoparticles. Thus the measurements of the exciton spin dephasing time using polarized FWM spectroscopy allow one to estimate the QD’s asymmetry and follow its dependence on the growth conditions.

The samples investigated in this chapter were obtained from commercial RG695 filter glass provided by Schott Glass Technologies. The samples containing *CdSe* QDs embedded in a glass matrix were subject to a heat-treatment procedure performed in the group of Dr. A. Filin at the Rensselaer Polytechnic Institute, Troy, USA. As-received RG695 was melted at 1050°C to dissolve particles and heat-treated after quenching to grow QDs of different size. (For details concerning the preparation see Ref. [80].) By controlling the growth parameters (time and temperature) nanoparticles of different sizes can be formed. The dimensions of the investigated QDs vary from 2.4 to 8 nm in diameter, obtained by varying the growth temperature in a range from 590°C to 720°C and the growth time between 0.5 and 280 h. The study will focus on samples having the same size but grown under different conditions. It will be referred to as ”slow-growth” for the samples grown over a longer period of time at lower temperature and ”fast-growth” for the samples grown

over shorter periods but at higher temperature. For the QDs grown under these conditions, the observed asymmetry will be discussed in terms of the kinetics of QD's growth.

In this section it will be focused in particular on two pairs of samples: the first pair (1a and 1b) has an average diameter  $\langle D \rangle = 2.8$  nm and the second pair (2a and 2b)  $\langle D \rangle = 4.8$  nm, respectively. The samples were prepared under the following conditions:

- sample 1a was grown during 280 hours at a temperature of 590°C (280h@590C) and will be called "slow growth 1" (SG1);
- sample 1b was heat treated for 2 hours at 650°C (2h@650C) and will be called "fast growth 1" (FG1);
- sample 2a was grown 8 hours at 700°C (8h@700C) and will be referred to as "slow growth 2" (SG2);
- sample 2b was treated for 1 hour at 720°C (1h@720C) and will be referred to as "fast growth 2" (FG2).

The absorption spectra of these samples are shown in figure 7.1. The exciton spin relaxation is investigated by means of the TI-FWM technique, using three perfectly circularly polarized laser pulses of approximately 80 fs duration. All three fs pulses have the same wavelength lying in the range of the  $1S_e - 1S_h$  transition as indicated by arrows in figure 7.1 for each sample separately. Note that the size of the interrogated particles is selected by the laser wavelength, because only the QDs resonant with the laser wavelength are excited. The study of the QD ensemble was reduced to the investigation of the time behavior of the TI-FWM signal for only two polarization geometries  $I^{++++}$  and  $I^{++--}$  (see chapter 6). In both cases, a transient population grating is created by temporal ( $t_{21} = t_2 - t_1 = 0$ ) and spatial interference of the first two  $\sigma^+$  polarized pulses in the sample space. The third pulse

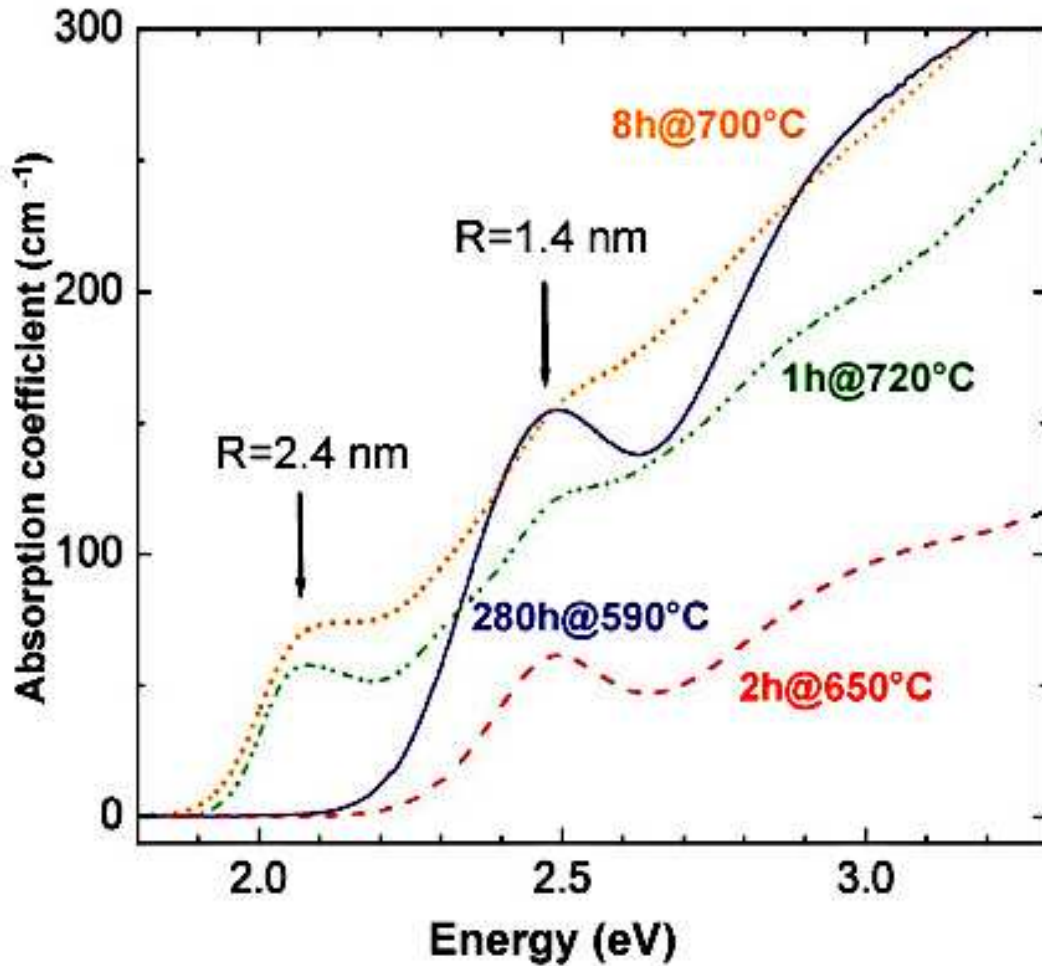


**Fig. 7.1:** Absorption spectra of QDs of different sizes (the radius of the dots are indicated in the figure) and grown under different conditions. The spectra are recorded at a temperature of 10 K. The excitation energies used in the TI-FWM measurements are indicated by arrows for each sample individually.

scans the transient population grating ( $t_{31} = t_3 - t_1$ ) and can be  $\sigma^+$  ( $I^{++++}$ ) or  $\sigma^-$  polarized ( $I^{++--}$ ), the FWM signal being scattered in the direction given by the phase matching condition  $k_s = -k_1 + k_2 + k_3$ , whose polarization always corresponds to the polarization of  $k_3$ . As shown in chapter 6, spin dephasing processes lead to the disappearance of the difference in intensities of the signals  $I^{++++}$  and  $I^{++--}$  for long  $t_{31}$  delay times, i.e. when the population grating is already spin dephased. Thus, the sum  $S^+ = I^{++++} + I^{++--}$  is analyzed in order to determine the exciton lifetime and the difference  $S^- = I^{++++} - I^{++--}$  to determine the exciton spin dephasing time and thus for estimating the QD's asymmetry.

The transient grating created in the sample volume by the interference of two  $\sigma^+$  polarized pulses with wave vectors  $k_1$  and  $k_2$  leads to a modulation of the refractive index due to the creation of an induced grating in the sample volume, whose knots are occupied by excitons. The amplitude of this induced grating and therefore the intensity of the scattered FWM signal is proportional to the exciton population density. Thus the intensity of the TI-FWM signal for different polarization geometries depends on the population density given by the excitons arrived in both states, with  $J = +1$  (eq. 6.3) and  $J = -1$  (eq. 6.4). For a  $\sigma^+$  polarized  $k_3$  beam one has  $I^{++++} \sim (2\rho_{++} + \rho_{--})^2$  and  $I^{++--} \sim (\rho_{++} + 2\rho_{--})^2$  for a  $\sigma^-$  polarized  $k_3$  pulse, respectively. Taking into account the exciton lifetime  $\tau_l$  and exciton spin relaxation time  $\tau_s$ , the population densities created in the two states  $J = \pm 1$  can be written as functions of decay times:

- $\rho_{++}(t) \sim \exp(-t/\tau_l)(1 + \exp(-t/\tau_s))$
- $\rho_{--}(t) \sim \exp(-t/\tau_l)(1 - \exp(-t/\tau_s))$ .

Therefore, the intensities of the TI-FWM signals can be expressed as follows:

$$I^{++++} \sim (2\rho_{++} + \rho_{--})^2 \sim \exp(-2t/\rho_l)(3 + \exp(-t/\tau_s))^2 \quad (7.1)$$

$$I^{++--} \sim (\rho_{++} + 2\rho_{--})^2 \sim \exp(-2t/\rho_l)(3 - \exp(-t/\tau_s))^2. \quad (7.2)$$



Therefore, the difference  $S^- = I^{++++} - I^{++--}$  results into:

$$S^- \sim \exp(-2t/\tau_l)\exp(-t/\tau_s) = \exp(-t/\tau^-), \quad (7.3)$$

where  $\frac{1}{\tau^-} = \frac{2}{\tau_l} + \frac{1}{\tau_s}$  is the decay time of the difference  $S^-$ . For the sum  $S^+ = I^{++++} + I^{++--}$  one obtains:

$$S^+ \sim \exp(-2t/\tau_l)[9 + \exp(-2t/\tau_s)] \approx \exp(-2t/\tau_l) = \exp(-t/\tau^+), \quad (7.4)$$

where  $\tau^+ = \tau_l/2$  is the decay time of the sum. The sum can be described by a single exponential with an accuracy of about 10%, because  $\exp(-2t/\tau_s) \leq 1$ .

Thus the decay of the sum  $S^+$  reflects the transient population dynamics, whereas the decay of the difference  $S^-$  is enhanced due to an exciton spin dephasing process. One of the fastest dephasing processes in an ensemble of asymmetric QDs with split  $J = 1$  exciton states is a spin precession with a rate of  $\Delta/2\pi\hbar$ . Such a spin precession in a randomly split exciton system leads to the disappearance of the difference in FWM signals observed for a scattering of  $\sigma^+$  ( $I^{++++}$ ) and  $\sigma^-$  polarized light ( $I^{++--}$ ) on the transient population grating created by two  $\sigma^+$  polarized pulses. Therefore, the temporal behavior of the difference  $S^- = I^{++++} - I^{++--}$  characterizes the dynamics of exciton spin dephasing.

Figure 7.2 shows the population dynamics for the two pairs of investigated samples. As it is clearly observable, the occupation decay time depends strongly on the particle size, while the lifetime of the population grating gets shorter with decreasing particle size. It is remarkable that the population lifetime is nearly independent on the growth conditions for particles having the same size, i.e. the decay of the sum  $S^+$  being the same for samples containing nanoparticles of the same size but grown under different conditions. In contrast, the exciton spin dynamics exhibits a drastic dependence on the growth conditions. Figures 7.3 and 7.4 display the temporal behavior of the difference  $S^- = I^{++++} - I^{++--}$  recorded for QDs of 1.4 nm and 2.4 nm in radius, respectively. The occupation dynamics  $S^+$  for one sample of each size

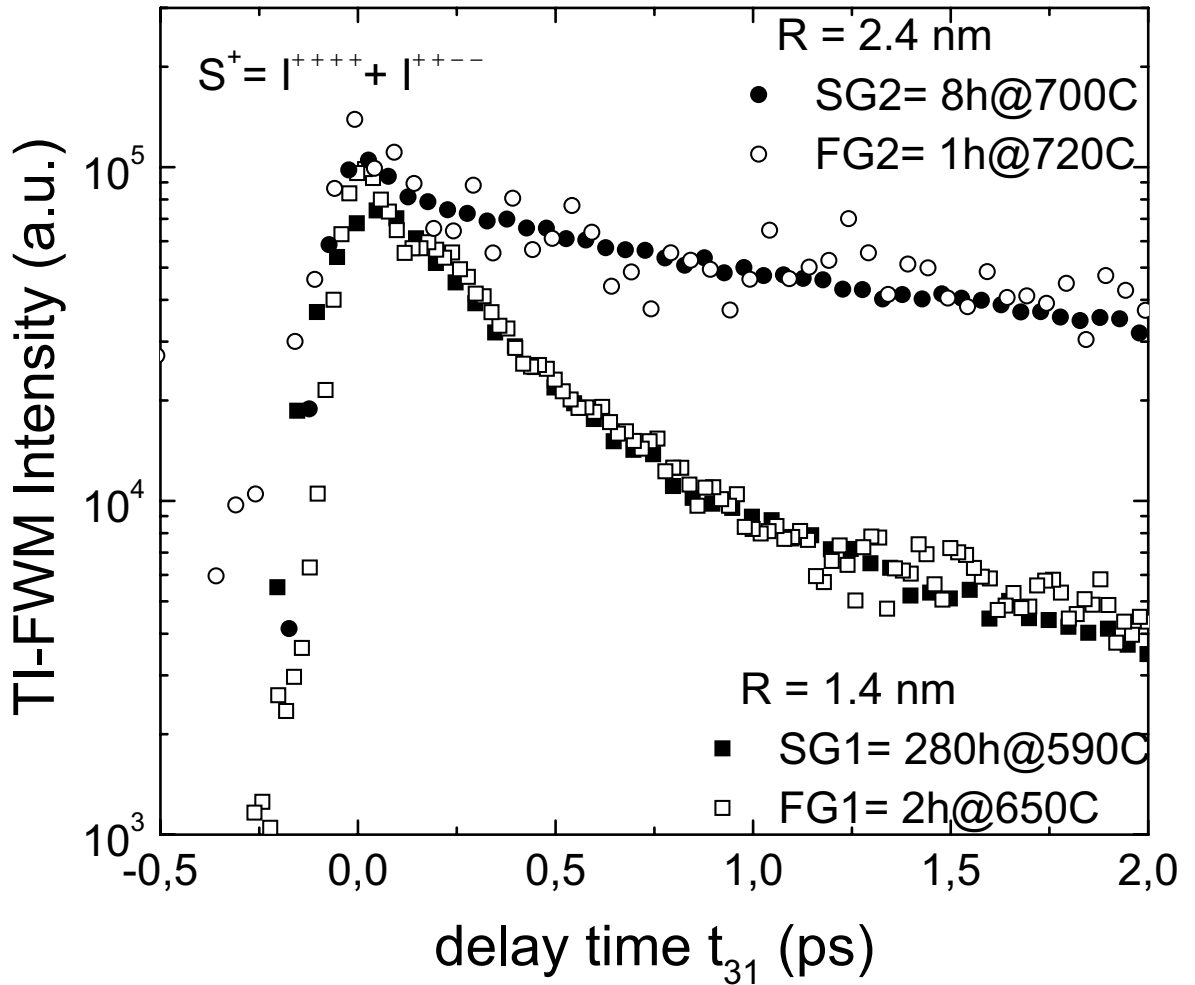


**Fig. 7.2:** The transients depicting the sum of polarized TI-FWM signals  $S^+ = I^{++++} + I^{+---}$  plotted on a logarithmic scale. The TI-FWM signals were recorded in the direction given by the phase matching condition  $k_s = -k_1 + k_3 + k_3$  as a function of time delay  $t_{31}$  of the pulse  $k_3$ . Squares correspond to the pair of samples containing smaller QDs ( $R=1.4$  nm) and the triangles to the pair containing larger QDs ( $R=2.4$  nm), respectively

are also plotted as a reference. The experimental data are represented by symbols, whereas the deconvolution (according to figures 7.4 and 7.3 for the sum  $S^+$  and for the difference  $S^-$ , respectively) by solid lines. For both pairs, the sample grown for shorter time at higher temperature ( $FG1 = 2h@650C$  and  $FG2 = 1h@720C$ ) shows much shorter decay time of the difference  $S^-$  as the sample grown for longer time at a lower temperature ( $SG1 = 280h@590C$  and  $SG2 = 8h@700C$ ). Note that the data are plot in logarithmic scale.

The exciton spin dephasing time  $\tau_s$  can be estimated from the difference  $S^-$ , however the exciton recombination has to be taken into account. The exciton depopulation time is:

$$\tau_l = 2\tau^+ \quad (7.5)$$

and therefore the spin dephasing time can be calculated:

$$\frac{1}{\tau_s} = \frac{1}{\tau^-} - \frac{1}{\tau^+}, \quad (7.6)$$

where  $\tau^+$  and  $\tau^-$  are the decay times of the sum  $S^+ = I^{++++} + I^{++--}$  and difference  $S^- = I^{++++} - I^{++--}$ , respectively.

For the sample SG1 containing smaller QDs (figure 7.3), the deconvolution according to eq. 7.3 yields a decay time of the difference  $S^-$  of  $\tau^- = 0.20$  ps, whereas the deconvolution according to eq. 7.4 yields a decay time  $\tau^+ = 0.28$  ps of the sum  $S^+$ , resulting in a spin dephasing time of  $\tau_s = 0.70$  ps. For the sample FG1 of the same pair 1 containing smaller dots,  $\tau^-$  is shorter than the time resolution of the system, i.e.  $\tau < 0.07$  ps.

The second pair of samples containing larger QDs show a more complex behavior. For SG2 one can associate two depopulation times:  $\tau_1^+ = 93$  fs and  $\tau_2^+ = 2.2$  ps, having their origins in two different kinds of particles. The contribution of the particles characterized by  $\tau_1^+$  is insignificant, their concentration being obviously smaller than that of the particles characterized by  $\tau_2^+$  (as it will be shown in the

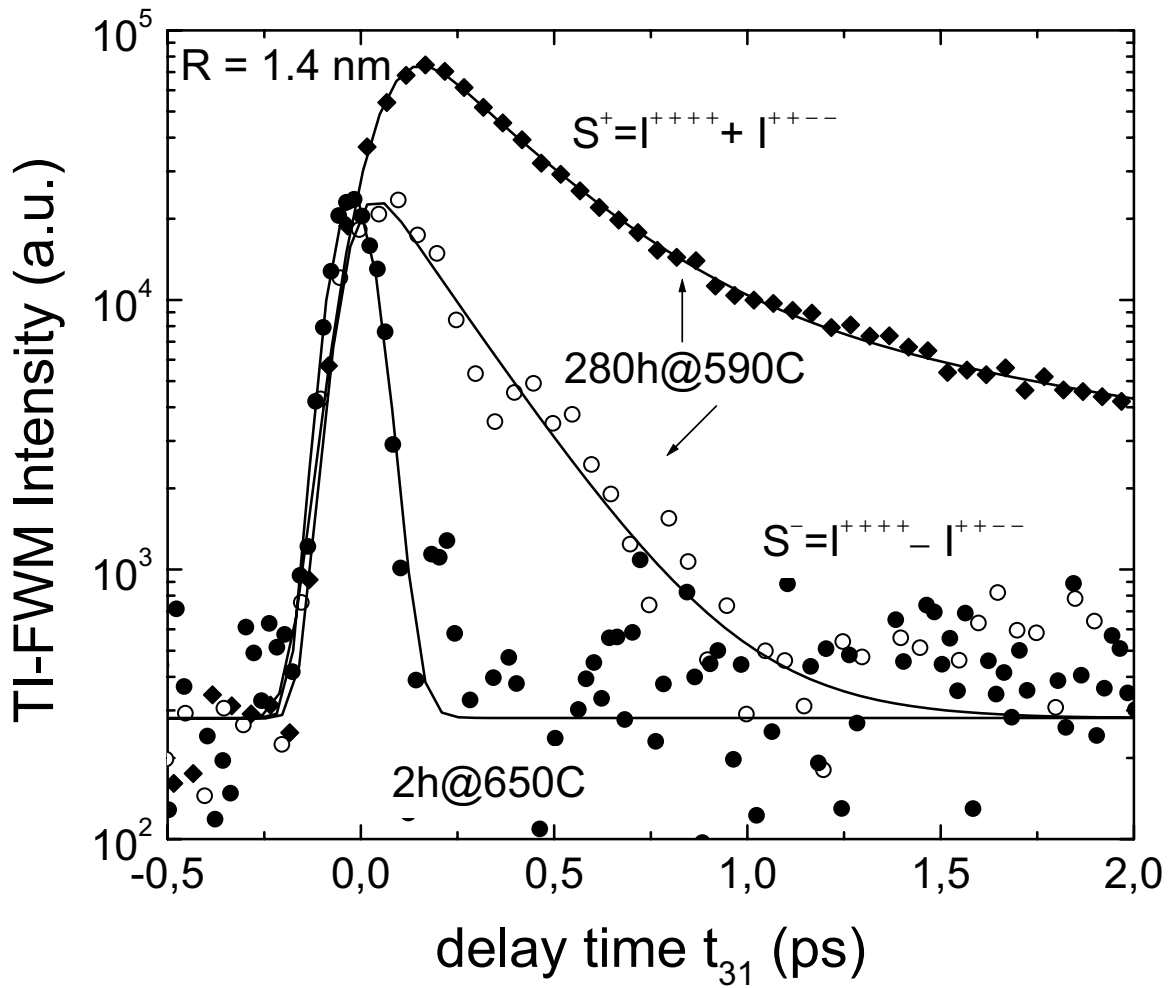


**Fig. 7.3:** Transients plotted as the difference in intensities of polarized TI-FWM signals  $S^- = I^{++++} - I^{+---}$  recorded for pair "1" of samples containing smaller QDs ( $R=1.4$  nm). The signals are plot on logarithmic scale. The empty circles correspond to "slow growth" sample SG1 (280h@590C), whereas the solid circles to the "fast growth" sample FG1 (2h@650C). The sum  $S^+$  is also plot (black curve with solid squares) and illustrates the difference in the behavior of the TI-FWM signals corresponding to the population and spin relaxation processes, respectively.

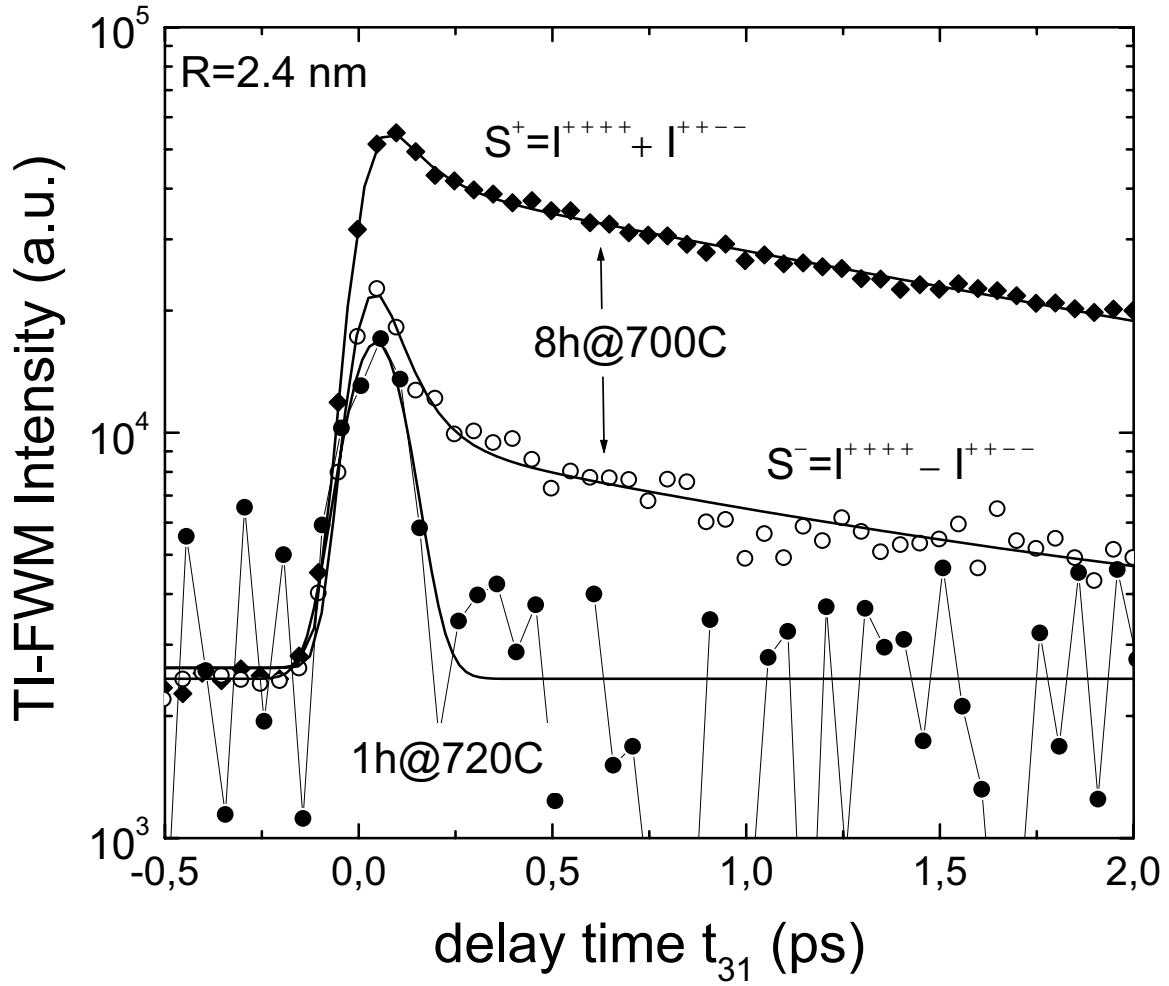


**Fig. 7.4:** Transients plotted as the difference in intensities  $S^- = I^{++++} - I^{+---}$  of polarized TI-FWM signals recorded for pair "2" of samples containing larger QDs ( $R=2.4$  nm). The signals are plot on a logarithmic scale. The empty circles correspond to the "slow growth" sample SG1 (8h@700C), whereas the solid circles to the "fast growth" sample FG1 (1h@720C). The sum  $S^+$  is also plot (black curve with solid squares) and illustrates the difference in the behavior of the TI-FWM signals corresponding to the population and spin relaxation processes, respectively.

next sections). Thus the dephasing process is mainly characterized by  $\tau_2^+$ . For SG2 one finds  $(\tau_s)_1 = 0.4$  ps and  $(\tau_s)_2 = 5.9$  ps, whereas in the case of FG2 one can only tell that  $\tau_s < 0.07$  ps, representing the time resolution of the fs system. As discussed earlier, the energy gap of the splitted  $J = 1$  exciton states can be estimated as  $\Delta \approx \hbar/\tau_s$ . For both "fast growth" samples (FG1 and FG2) it can be concluded with certainty that the energy splitting is  $\Delta > 20$  meV, which indicates a very high asymmetry of the quickly grown QDs. For the "slow growth" sample SG1, the splitting is  $\Delta \approx 2$  meV, whereas in the sample SG2 the most of the QDs show a much slower decay, indicating that  $\Delta \approx 0.3$  meV. The decreased splitting of the  $1S$  exciton state indicates that with increasing growth time the QD shape becomes more and more symmetric. Note that the results are used only for a qualitative rather than any quantitative estimations.

In summary, there are two remarkable aspects of the present observations:

1. the population lifetime depends only on the particle size, and doesn't depend on the growth temperature,
2. the exciton spin dephasing time depends strongly on the preparation history. Samples containing nanoparticles of the same size have the same lifetime, but if they were grown under different conditions, they exhibit different spin dephasing times: the samples grown for longer times at lower temperatures yield a longer spin dephasing time, whereas the samples grown for shorter times at higher temperature exhibit shorter spin dephasing times.

Note that the exciton spin dephasing time in discussion is not a "real spin decoherence time" but it is due to the random splitting of the  $J = 1$  exciton states.

The asymmetry of nanocrystals can originate a) from distortion of the hexagonal lattice structure of the crystal [1] and b) from the nonspherical shape of the finite nanocrystal having the radius smaller or comparable to the exciton Bohr radius [2]. The distortion of the intrinsic hexagonal structure does not influence the

splitting of the  $J = 1$  exciton state [1, 77]. The only contribution to the energy redistribution of the  $J = 1$  exciton comes from deviations from the spherical shape of the nanocrystals due to the creation of additional strains at the heterointerface semiconductor-dielectric matrix. It follows from studies of  $\tau_s$  that the  $J = \pm 1$  exciton splits and hence the QD's symmetry for nanocrystals of the same size increases strongly with increasing growth time and decreasing temperature.

The crystal quality and the deviation from the spherical shape of a nanocrystal can be related to three physical aspects:

1. entropy-induced disorder,
2. defects and roughness due to kinetic limitations,  
and/or
3. energy differences between crystallite facets.

In order to ingeniously determine the symmetry of the nanocrystals, their thermal history has to be taken into account. By means of rapid quenching from the melt, the QD's structure can be "frozen" in a homogeneous state in the dielectric matrix, whose viscosity strongly depends on the temperature. The rate of the QDs precipitation from glass depends on two factors: on the thermodynamic driving force and on the kinetic factor [81]. The thermodynamic driving force consists in a decrease in the free energy of the system due to the formation of a QDs precipitate. The kinetic factor is related to the mobility of the system and depends strongly on the temperature. Due to the fact that the kinetic factor is a proportionality constant between the driving force and the rate of particle formation, it is agreed that the kinetics factor plays the most important role in formation of defects in CdSe QDs in dielectric matrices.

Nanocrystals of high symmetry are obtained if the lowest energy state in the crystallite can be achieved. If this state involves symmetric facets with smooth surfaces, the nanoparticle can be prevented from achieving this lowest energy state if diffusion

and relaxation processes are slow compared to the rate of the arrival of atoms at the growth surface. In one extreme, the particle arrival without relaxation gives rise to fractal aggregation [82]. In order to compare samples prepared under different conditions, a parameter named "growth quality coefficient,  $Q$ " is introduced. This parameter is directly proportional to the diffusion rate  $Diff$  and inversely proportional to the flux of atoms (adatoms) migrating towards the growth surface  $F$ :

$$Q \sim \frac{Diff}{F}. \quad (7.7)$$

The growth rate is proportional to the adatom growth flux and hence inversely proportional to the growth time of the last crystallite monolayer. The growth rate can be estimated from the crystal size, and the relative relaxation rate from the self-diffusion data, respectively.

If we assume that the crystals were formed by diffusion-limited growth from infinitesimal seeds, then the growth rate can be estimated for these four samples (SG1, FG1, SG2 and FG2) for a particular size. For an estimation of the time to grow the last crystal layer, it has to be taken into account that in a diffusion-limited growth process the QD's size increases as the square root of the growth time [83]:

$$R(t) = R_0 + at^{1/2}, \quad (7.8)$$

where  $R_0$  is the initial size of the seed and  $a$  is the growth rate. The size of the initial seed is infinitely small and can be approximated to  $R_0 \approx 0$ , therefore:

$$t = \frac{1}{a^2}R^2, \quad (7.9)$$

whose derivative yields the time to grow the last monolayer  $\Delta t$ :

$$\Delta t = \frac{1}{a^2}2R\Delta R. \quad (7.10)$$



Here, taking into account 7.9, the growth rate  $a$  can be written as a function of the growth time  $t$  and the nanoparticle's radius  $R$

$$\frac{1}{a^2} = \frac{t}{R^2}, \quad (7.11)$$

enabling one to determine the time to grow the last layer  $\Delta t$  as a function of the QD's final size  $R$  and the total growth time  $t$ :

$$\Delta t = t \times \frac{2}{R} \times \Delta R. \quad (7.12)$$

Here,  $\Delta R$  is the thickness of the last monolayer and represents the lattice constant of CdSe,  $\Delta R = 0.27$  nm.

On one hand, one can expect that the longer the time to grow the last crystal monolayer, the better the QD's quality because the adatoms have more time to occupy proper positions (states of lower potential energy). Indeed, the lower the temperature, the longer the time to grow the last monolayer for samples containing QDs of equal size (see table 7.1).

However, there's another process which significantly affects the quality of QDs, connected to the migration of the adatoms towards the infinitesimal growing seeds. As indicated above, the growth mechanism takes place in the framework of diffusion-limited processes. Diffusion processes in such nanocrystals are characterized by the diffusion coefficient, estimated by Jones et al. [84]:

$$Diff = Diff_0 \exp\left(\frac{-2.7[eV]}{kT}\right). \quad (7.13)$$

The diffusion coefficient  $Diff$  is a measure of the adatoms kinetics, and, subsequently of their mobility. Therefore, it is evident that the larger the diffusion constant  $D$ , the better the quality of the crystal because for a certain time domain, the adatoms have larger degree of freedom to build a "perfect" crystal. In order to monitor the evolution of QDs in time, the diffusion scaling factor was analyzed:

**Table 7.1:** Degree of Asymmetry of QDs

R (nm)	Growth Time (h)	Growth Temp. (°C)	Last Layer Growth Time (h)	Diffusion Scaling Factor	Quality Coeff. Q	$\frac{1}{Q}$	$\tau_s$ (ps)	$\Delta$ (meV)
1.4	280	590	108	$3.22 * 10^{-15}$	1	1	0.7	2
1.4	2	650	0.77	$2.65 * 10^{-14}$	0.059	17	< 0.7	> 20
2.4	8	700	1.80	$1.26 * 10^{-13}$	0.56	1.8	0.4 5.9	4 0.3
2.4	1	720	0.22	$2.26 * 10^{-13}$	0.126	8.0	< 0.07	> 20

$$\frac{Diff}{Diff_0} = \exp(-2.7[eV]/kT[K]), \quad (7.14)$$

which shows the changes in the diffusion process during the crystal growth time.

The diffusion process is strongly temperature dependent. Higher temperatures assure better mobility and subsequently larger  $Diff$  and better quality of the QDs. However, in order to obtain QDs of a certain size, if the temperature is increased, the growth time has to be reduced. In order to figure out which factor is decisive for the characterization of QD's quality, the "quality coefficient Q" is introduced. Q is directly proportional to the time to grow the last monolayer  $\Delta t$  and inversely proportional to the diffusion scaling factor  $\frac{Diff}{Diff_0}$ . This is an arbitrary coefficient and can be set to 1 for the sample grown for longer time at lower temperature  $280h@590C$ , which is supposed to have the highest symmetry. The quality coefficients for the other three samples were scaled relative to Q determined for the sample  $280h@590C$ .

For both sample pairs discussed in this section, the "fast growth" samples (FG1 and FG2) exhibit much smaller quality coefficient  $Q$  as the "slow growth" (SG1 and

SG2) samples. These two samples FG1 and FG2 show also much shorter dephasing times as SG1 and SG2, the corresponding splitting being also relatively large ( $> 20$  meV), implying a relatively large asymmetry.

Figure 7.4 shows that the "slow growth" sample containing the larger QDs SG2 exhibit two values of  $\Delta$ , corresponding to two characteristic dephasing times. This result is a consequence of the transient fitting (see figure 7.4) with two exponentials. It is natural to suppose that in this sample two types of QDs are excited. Details concerning this two-exponential decay fit of the transient will be discussed in section 7.2. This fit shows that the majority of the QDs are characterized by a longer spin dephasing time of  $\tau_s = 5.9$  ps and only these must be further considered for a comparison with the other nanocrystals.

Thus the investigation of the exciton spin dephasing time in *CdSe* QDs embedded in a glass matrix by means of polarized transient grating methods yields valuable information on the symmetry of QDs grown under various conditions. The most surprising result of this study is the observation of those QDs that appear to be identical by many measures (size, linear absorption spectrum, exciton lifetime), these exhibiting very different exciton spin dephasing times. The dephasing times correlate with a measure of the crystal structural quality parameter estimated from the ratio between the time for a point defect to diffuse across the crystallite and the time necessary to grow the last monolayer of the crystal. For both pairs of samples of different sizes, when  $Q$  is small, the asymmetry measured by TI-FWM is large and when  $Q$  is large the degree of symmetry is much greater. The quality coefficients are summarized in table 7.1 and it can be seen, that the inverse of the quality coefficient ( $1/Q$ ) increases with increasing asymmetry of the nanocrystal. The splitting  $\Delta$  of the  $J = 1$  exciton state was estimated from the exciton spin dephasing time  $\tau_s$ , where  $\Delta \approx \hbar/\tau_s$ . These results are also summarized in table 7.1, reflecting the degree of asymmetry of the four samples discussed in this section.

A qualitative comparison using both methods was achieved. The results concerning the quality of the QDs determined using the diffusion calculation method and

thus calculating the quality coefficient  $Q$  are in very good agreement with the energy splitting  $\Delta$  calculated from the spin dephasing time of the exciton energy levels with  $J = 1$ . Comparing the results of these two methods, we can conclude that TI-FWM polarized measurements are an appropriate tool to investigate the asymmetry of nanoparticles. This study yields invaluable information for the QD manufacturing process of nanocrystals, showing the ways to be followed in order to obtain QDs of high quality.

## 7.2 Dependence of the Exciton Lifetime on the Nanoparticles' Size

The size of semiconductor nanostructures is a crucial parameter concerning both their electronic and optical properties [77,85]. This section is focused on the investigation of quantum size dependence of exciton fine structure of CdSe QDs embedded in a glass matrix.

Femtosecond DFWM in the framework of transient grating experiments, described in the chapters 4 and 5 were performed on heat treated CdSe QDs of different sizes, prepared by the method presented in section 7.1. The following samples were investigated:

1. 0.5h@700C containing QDs of 1.4 nm in radius;
2. 2h@700C containing nanoparticles of 2.2 nm in radius;
3. 16h@720C with QDs of 3.2 nm in radius.

The samples were labelled indicating both the duration of the heat treatment (in hours) and the temperature (in °C), abbreviated as follows "duration h @ temperature °C".

During the experiments the samples were mounted into an optical cryostat and kept at a temperature of 10 K. Size selective excitation of the nanocrystals was achieved by appropriate choice of the excitation energy. The choice of the latter near the resonance of the absorption of the  $1S_e - 1S_h$  exciton transition allows one to choose the excited QDs close to the mean size of the nanoparticles included in the matrix. The absorption spectra of the investigated samples are shown in figure 7.5, the excitation energy being indicated by arrows for each sample individually.

As already introduced in the chapters 4 and 5, the samples are excited by 3 circularly polarized femtosecond pulses in transient grating experiments and the FWM signal was scattered in the direction given by the phase matching condition

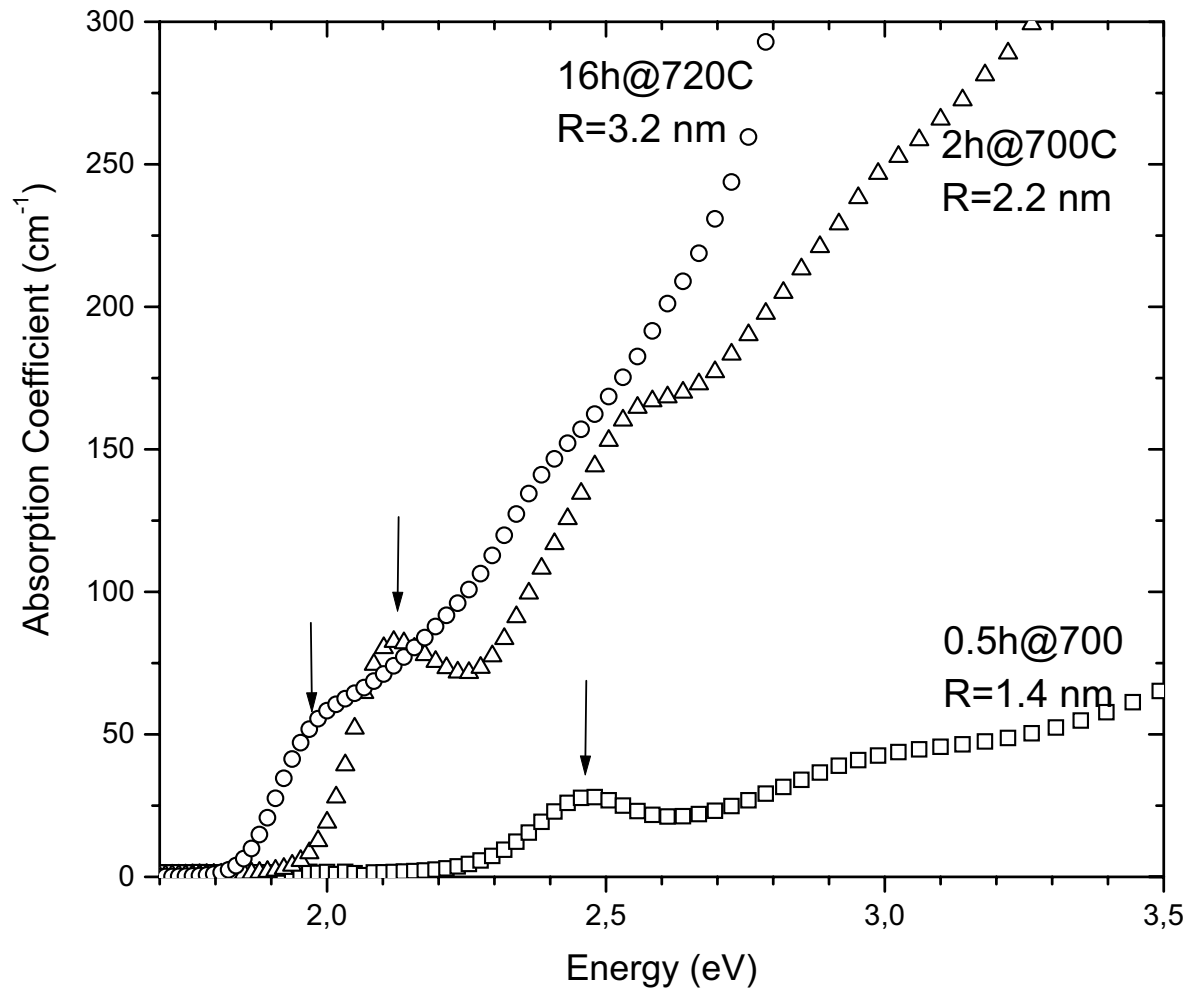


**Fig. 7.5:** Absorption spectra of CdSe QDs of different sizes embedded in glass matrix, recorded at 10 K. The excitation energy used in the FWM measurements is indicated by arrows for each sample individually.

$k_s = -k_1 + k_2 + k_3$ . The incident fs pulses are circularly polarized and for these experiments two relevant polarization geometries were selected:  $I^{++++}$  where all 3 incident pulses and the recorded signal are  $\sigma^+$  polarized and  $I^{++--}$ , where the first two (in time) pulses  $k_1$  and  $k_2$ , which create the exciton population grating are  $\sigma^+$  polarized, whereas the third pulse with a wave vector  $k_3$  and the recorded signal  $k_s$  are both  $\sigma^-$  polarized. The sum between the intensities of the TI-FWM signals recorded under these two polarization geometries  $S^+ = I^{++++} + I^{++--}$  is a direct measure of the exciton population dynamics, its decay serving as a measure of the exciton lifetime. This sum  $S^+$  registered for the QDs discussed above is shown in figure 7.6. In the following, the relaxation processes from the lowest lying  $1S$  exciton state will be discussed.

It was shown [81, 86, 87] that Auger processes play an essential role in the degradation of the nonlinear properties of nanocrystals. In particular, Auger ionization followed by the capture of carriers in the surrounding matrix bring strong contributions to the decay of the optically excited electron-hole states in confined media. The signal decay rate is determined mainly by the Auger ionization rate and the probability of creating two electron-hole pairs in the nanocrystal. The Auger processes affect all aspects of carrier relaxation and recombination.

The optical excitation of an electron-hole pair in an electrically neutral QD results usually in the emission of a photon as a consequence of its annihilation. However, in charged systems the annihilation energy can be taken up by the extra electron or hole instead of being re-emitted in form of a photon. This phenomenon is due to the large Auger rate in comparison to the radiative recombination rate in nanocrystals [81]. The extra charge can be created in the nanocrystal by optical excitation even if the energy of the incident photon is not sufficient for a direct ionization of the nanoparticle. The Auger autoionization of nanoparticles depends strongly on factors like QD's size, band offset between the semiconductor nanocrystal and the surrounding matrix, temperature and excitation energy.

For the creation of Auger autoionized nanocrystals, the simultaneous excitation

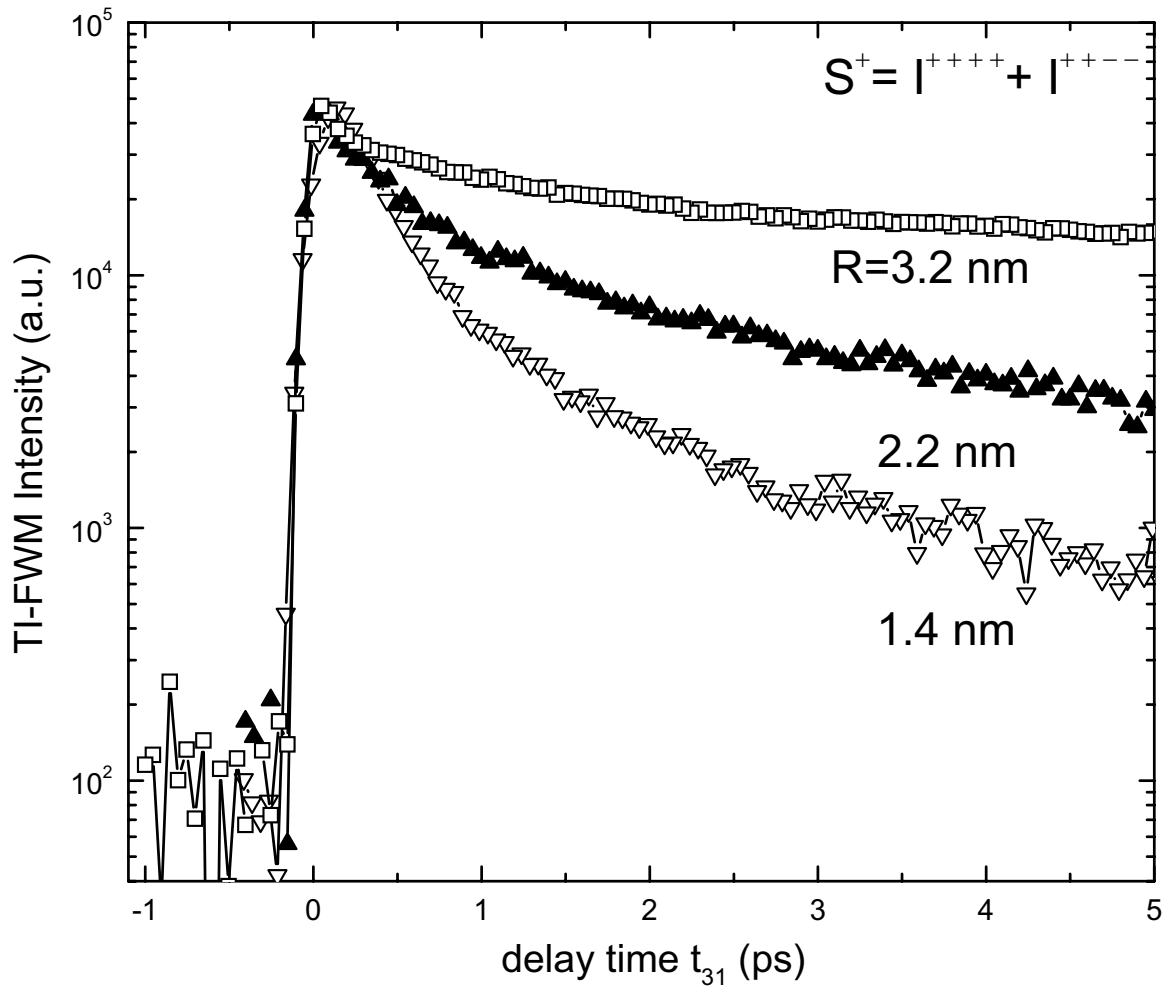


**Fig. 7.6:** Sum  $S^+ = I^{++++} + I^{+---}$  as a function of the delay time  $t_{31}$  for QDs of different sizes, whose absorption spectra are presented in figure 7.5.



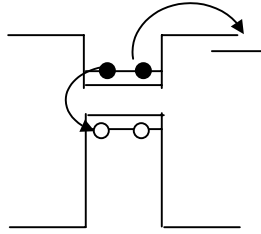


**Fig. 7.7:** Process of Auger autoionization in nanocrystals. Two electron-hole pairs are simultaneously excited, one of the carriers being ejected into the dielectric matrix and captured by surface states or crystal defects.

of two electron-hole pairs in the same QD is necessary (figure 7.7). The annihilation energy of one of the electron-hole pairs is transferred to the carriers of the second electron-hole pair thus resulting into ejection of carriers from the crystal. The ejected carriers (electrons or holes) are then localized in traps in the surrounding matrix or at the nanocrystal surface.

The efficiency of Auger processes in nanocrystals with respect to their rate in the bulk is related to energy and momentum conservation rules. In large band-gap bulk semiconductors as CdS and CdSe the Auger processes are considerably suppressed because in homogeneous materials both energy and momentum are conserved. These conservation rules lead to an exponential dependence of the recombination rate on the ratio  $E_g/T$ , where  $E_g$  represents the semiconductor band gap and  $T$  the temperature. Thus for large values of the energy gap  $E_g$  the Auger processes become negligible in the bulk.

The reasons for the enhancement of Auger processes in nanocrystals lies in the different structural properties of confined systems in comparison to bulk materials. In nanocrystals the momentum of the carrier motion is not a good quantum number anymore, therefore no valid conservation law for the momentum can be written. Moreover, the enhancement of Coulomb interactions between carriers due to quantum confinement cannot be ignored. Thus the Auger processes become very efficient when the volume of the semiconductor is reduced and the carriers are confined in all

three spatial dimensions. The rate of Auger interactions in QDs can be determined using Fermi's golden rule:

$$\frac{1}{\tau_A} = \frac{2\pi}{\hbar} \sum_{k,l,m} \left| \left\langle \Psi^i | V(r_1^{\vec{r}}, r_2^{\vec{r}}) | \Psi_{k,l,m}^f \right\rangle \right|^2 \delta(E_i - E_f), \quad (7.15)$$

where  $E_i$ ,  $E_f$  and  $\Psi^i$ ,  $\Psi^f$  are the energies and wave functions of the initial and final electronic states of the nanocrystal, respectively. The rate of Auger processes depends on the Coulomb potential  $V(r_1^{\vec{r}}, r_2^{\vec{r}}) = \frac{e^2}{\epsilon|r_1^{\vec{r}} - r_2^{\vec{r}}|}$  existing between two carriers situated at a distance defined by the difference between their position vectors  $|r_1^{\vec{r}} - r_2^{\vec{r}}|$  in a medium having the dielectric constant  $\epsilon$ . The summation is made over all final states of the system  $(k, l, m)$ .

A qualitative explanation in a semi-classical picture of the meaning of the Auger process rate can be given by analyzing the carrier dynamics in the framework of energy transfer. The electron shows an affinity to take up the annihilation energy of the exciting photon at the place where its kinetic energy, or kinetic energy uncertainty has a maximum value. Such a place can be created in the center of an impurity, where the potential energy goes to minus infinity and the kinetic energy has a maximum.

For quantum confined systems, Auger processes take place at the abrupt heterointerface, where the surface of the nanocrystal gets in contact with the dielectric matrix. Here, the electron momentum uncertainty is very large and the electrons can gain enough momentum at the interface. Quantum mechanical calculations [87] confirm that Auger processes take place right at the nanocrystal surface because the abrupt surface significantly accelerates the Auger ratio  $\tau_A$  in nanoparticles with large surface to volume ratio. Efros et al. demonstrated a very strong dependence of the Auger autoionization rate on the band offset and an even stronger dependence on the nanoparticles' size [77, 81]. The average size dependence was found to be:

$$\left\langle \frac{1}{\tau_A} \right\rangle \sim \frac{1}{R^\nu}, \quad (7.16)$$

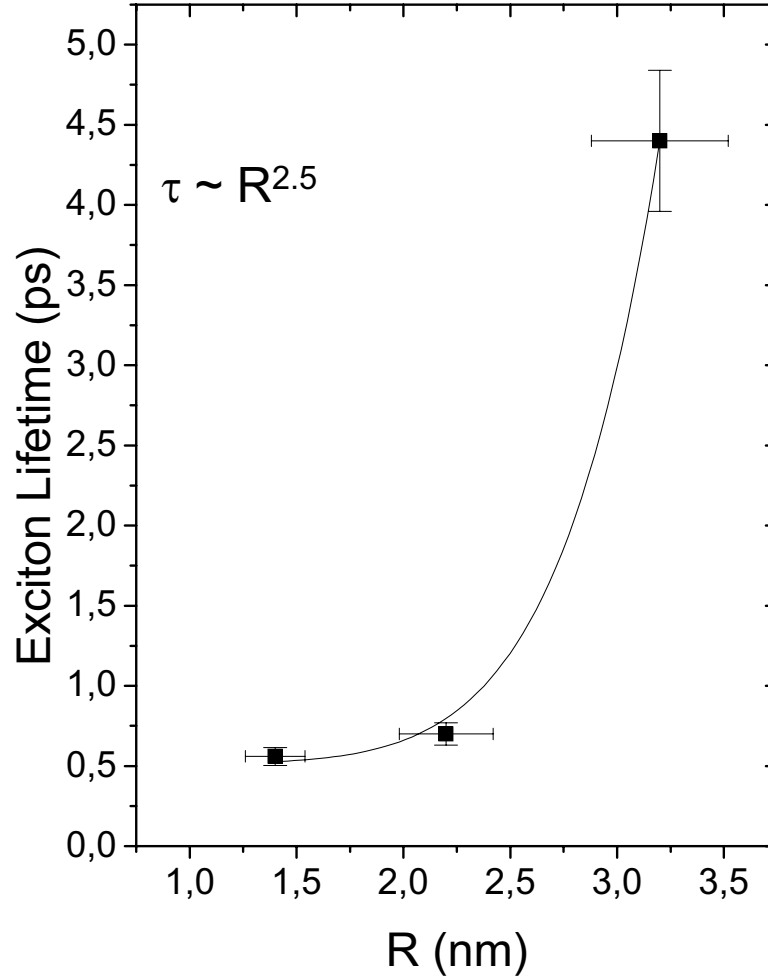


**Fig. 7.8:** Dependence of the exciton lifetime  $\tau_1$  on the size of the nanoparticles  $R$  following the power law  $\tau \sim R^{2.5}$ .

where  $R$  stands for the size of the nanocrystal and  $5 < \nu < 7$  is a coefficient depending on the band offset.

The exciton lifetime for the QDs under discussion was determined from the transients plotted in figure 7.6. The results are presented as a function of the QD's size in figure 7.8. Figure 7.8 shows that the dependence of the exciton lifetime on the QD's size is markedly weaker ( $\tau \sim R^{2.5}$ ) than Efros' predictions concerning the dependence of the Auger autoionization's rate on the QD's radius (eq. 7.16). Therefore, the Auger autoionization is not the major process contributing to the recombination

of excitons in the samples studied within this chapter and the transients plotted in figure 7.6 have to be analyzed more carefully.

The decay of the TI-FWM signal (figure 7.6) is not monoexponential, especially for QDs having a radius  $R < 2.5$  nm, two decay channels are clearly distinguishable: an initial very fast decay (a few hundred of fs) and a slower decaying channel (a few ps). These two decay channels indicate the existence of at least two different types of QDs, which coexist in the nanocrystals and exhibit different relaxation channels. In order to understand the relaxation process, the energy structure of the lowest lying exciton state ( $1S_{3/2}, 1s_e$ ) has to be taken into account. As described in detail in section 2.3.1 this electron-hole pair state is split due to the crystal field and/or QD's asymmetry (figure 2.5) into two sets of states, labelled  $A$  and  $B$  [4]. Figure 7.9 shows a simplified picture of the splitted  $1S$  exciton state, including the only optically accessible  $A$  states, which are further split into the states labelled  $A_T$  and  $A_F$ . It can be seen, that the lowest lying optically active exciton state  $A_T$  is not the energetically lowest lying exciton state. The latter is labelled  $A_F$  and is known in literature as "dark exciton state". Transitions to the dark state are optically forbidden, because the light couples to states with  $J = 2$  only in higher order perturbation theories. Therefore optical excitation occurs only on the  $A_T$  bright exciton state, from where the excitons in the investigated samples relax in a few ps.

From the bright exciton state, there are three possible relaxation channels:

- radiative recombination,
- capture of carriers in deep traps,
- spin relaxation into dark states.

The radiative recombination time in strongly confined CdSe QD systems was determined [88] to be approximately 300 ps and no decrease is expected for QDs with a radius  $R < 3$  nm. The calculations referring to nanocrystals embedded in a

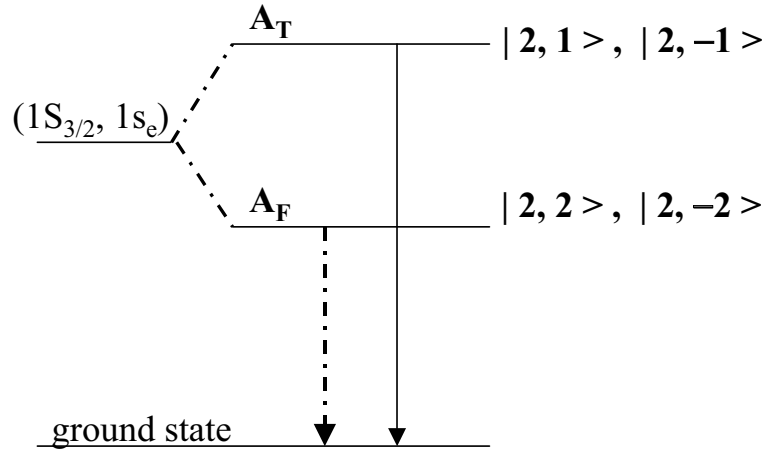


**Fig. 7.9:** Degeneracy of the lowest lying exciton state  $(1S_{3/2}, 1s_e)$  into the  $A_F$  dark- and  $A_T$  bright exciton states. The states are labelled by the corresponding "ket-vectors"  $|N, N_m\rangle$ , composed by the total pair angular momentum  $N$  and its projections  $N_m$ .

matrix with similar dielectric constants  $\epsilon_{matrix} \approx \epsilon_{QD}$  showed that corrections are necessary in order to explain the short relaxation times in the samples studied within this chapter. For example, the calculations must take into account the effect of the environment having a quite different dielectric constant  $\epsilon_{matrix} \neq \epsilon_{QD}$ . Indeed, the effect of a smaller dielectric constant of the matrix  $\epsilon_{matrix} \ll \epsilon_{QD}$  results into two opposite contributions:

1. decrease of the electric field of the light in the nanocrystal due to its redistribution into the matrix with smaller dielectric constant and thus increase in the exciton lifetime;
2. enhancement of Coulomb interaction between carriers ( $F_{Coulomb} \sim \frac{1}{\epsilon}$ ) and hence leading to some decrease in the exciton lifetime.

However, the effect of the enhanced Coulomb interactions cannot be significant concerning the relaxation of the excitons and cannot induce such a big decrease (two orders of magnitude) in the exciton lifetime, because the main effect in the

confinement of electrons and holes in nanocrystals is due to the QD confinement potential. Indeed, calculations performed by Tagakahara et al. for *CdSe* QDs embedded in a glass matrix have shown that the decreased dielectric constant in the matrix leads to a decrease by 0.6 in the exciton lifetime [89]. Thereby, it is obvious that the radiative recombination cannot result in the short exciton lifetimes observed in our experiments.

The initial very fast decay channel observed for all samples in figure 7.6 can be attributed to Auger autoionization processes. A very small fraction of QDs in the matrix are characterized by very short lifetimes (of a few hundred of fs) and they are connected to the initial fast decrease in the intensity of the TI-FWM signal. The experiments show a strong dependence of this decrease on the excitation density and temperature. To diminish this effect a minimal excitation density ( $0.1 \text{ nJ}/\mu \text{ m}^2$ ) and the lowest temperature achievable in the cryostat (10K) was chosen. Moreover, the Auger recombination occurs on a sub ps time scale and its rate increases with the excitation density and/or the temperature. Thus it can be concluded that this small part of nanocrystals are charged ones, which recombine via Auger-autoionization processes. Therefore, the Auger processes dominate only at the beginning of the exciton relaxation, after Auger recombination the charged QDs do not contribute further to the exciton lifetime.

The second relaxation channel observed in figure 7.6 can be connected either to a simple energy relaxation from the bright  $J = 1$  to the dark  $J = 2$  exciton state and/or to a capture of the exciton into a lower state connected to surface defects. The latter mechanism is very probably because the glass and the nanocrystals have quite different lattices and lattice parameters, a fact which favors the appearance of surface defects with captured charges, which show fast subsequent recombination. Both energy relaxation to the ground dark state and surface defect assisted recombination can provide a strong decrease in the lifetime of bright excitons. Indeed, as the QD's size (radius  $R$ ) increases, the energy relaxation from bright to dark exciton states involves an increasing number of phonons  $K \sim \frac{1}{R}$ , thus leading to a decrease

in the exciton lifetime. On the other hand, the effect of surface defects is usually proportional to the surface/volume ratio of the nanoparticle, increasing with  $1/R$ . In addition one has to take into account an increase in the exciton wave function at the QD boundary which results in an additional enhancement of the transfer of QD excitons to the surface defect.

Thus a differentiation between these two channels is not easy. Of course, the transition to dark state does not restore the ground state, the lifetime of dark excitons being in a microsecond range. Hence energy relaxation into the dark exciton state can result maximum in a 4-times decrease in the intensity of the FWM signal. The experiments show a much stronger decrease for samples with very small dots (almost one order of magnitude for the samples 0.5h@700C and 2h@700C containing QDs of 1.4 nm and 2.2 nm in radius, respectively). Thereby one assumes that the main channel is the surface defect assisted recombination of bright excitons.

The sample containing bigger QDs with a radius  $R > 2.5$  nm (16h@720C) shows a relatively small decrease in the TI-FWM signal (10%) and to choose between the two relaxation channels described above is impossible. The relaxation into dark exciton states is not excluded and contributes to the FWM signal via the unoccupied ground state. For the smallest nanocrystals with  $R < 2.5$  nm where the fraction of the slowly decaying signal is well below 10% definitely indicates that the measured time is not the spin relaxation time from a bright  $J = 1$  into a dark  $J = 2$  exciton state. Another proof that the measured time corresponds to the nonradiative surface defect assisted recombination of QD excitons is the fact described in section 7.1, where it was shown that the exciton lifetime depends only on the QD's size and not on the growth conditions. In section 7.1 it was shown that the growth conditions, which influence the QD's symmetry and therefore the energy separation  $\Delta$  between the bright and dark exciton states do not have any influence on the exciton lifetime. If the exciton would relax via this path (bright to dark states), their lifetime should definitely depend on the fine energy structure of the  $1S$  exciton and hence on the QD's shape.

In conclusion, the relaxation scenario occurs as follows: First, there is a small part of charged dots with a decay of a few hundred of fs and whose contribution disappears already for the sub ps range. However, most of the nanoparticles are neutral but show surface defects. These defects result in a strong decrease of the bright exciton lifetime to a ps or an even smaller range with decreasing QD's size. The decay is not monoexponential because with increasing delay time one deals already with a relatively small part of QDs, which are nearly free of defects having a relatively long lifetime in the range of hundred ps. It is certain as well that the part of bright excitons relaxes into dark exciton states that live in defect free dots hundreds of ns or even longer [90]. They as well contribute to the FWM signal via unoccupied ground states. However, this part of the QDs is negligible because the quantum efficiency of the emission from the dark exciton states is very small [90].

### 7.3 Energy Relaxation Mechanisms from Higher Excited States

In the previous sections it was shown that relaxation processes in quantum dot confined systems usually range on a ps time scale, thereby fs laser pulses are necessary for an ingenious investigation. Carrier relaxation in 3D confined systems is significantly different from the relaxation mechanisms in bulk semiconductors due to differences in the energy distribution. In contrast to the bulk, which shows energy bands with a continuum of states, the QDs present atomic-like discrete energy levels created as result of quantum confinement effects [1–4, 33, 77]. Therefore it is expected that the carrier relaxation in nanocrystals is governed by other rules as in bulk semiconductors. In the bulk, the relaxation of nonequilibrium electrons and holes is mainly mediated by carrier interaction with phonons and, subsequently, carrier-carrier scattering. In nanoparticles such mediation of carrier relaxation by phonons is considerably suppressed even for nanocrystals in the weak confinement



regime, where the level spacing is only a few meV, because of restrictions imposed by energy and momentum conservation. Small II-VI semiconductor QDs, i.e. *CdSe*, show a large band gap of up to 16 LO-phonon energies – depending on the size of the nanocrystal. Therefore it is natural to suppose that carrier-phonon scattering can occur only via multiphonon processes [91], which are less probable mechanisms. Despite that, the relaxation rates of carriers in nanocrystals are not significantly slower than in materials with a continuous energy spectrum [92–94]. There are several mechanisms proposed for explaining this effect in QDs. An important role might play different types of Auger processes:

1. Auger-type scattering in the presence of dense electron-hole plasmas [92];
2. Auger-like energy transfer between carriers [93];
3. scattering on defects [94].

Electron-hole plasmas can be only created by a very high excitation density, which in glass matrix by the excitation density of  $0,1 \text{ nJ}/\mu\text{m}^2$  used in the experiments presented within this chapter is definitely excluded. Thus it will be focused on the other two possible relaxation mechanisms in order to explain the dynamics of carriers situated in higher excited states. The sample investigated in this section contains heat-treated QDs embedded in a glass matrix and belong to the same group of samples discussed in section 7.1 and 7.2. The preparation method is briefly described in section 7.1, detailed information being available in the PhD thesis of Yukselici [80]. In particular, it will be focused here on the samples called *2h@700C* containing nanoparticles of 2.2 nm in radius. During the experiments, the sample was mounted into an optical cryostat and kept at a temperature of 10 K.

The most probable transitions (figure 2.6) take place between the lowest lying exciton states. For QDs in strong confinement regime, the first five lowest lying exciton states were theoretically determined [4] as an increasing energy separation from the ground state:  $(1s_e, 1S_{3/2})$ ,  $(1s_e, 2S_{3/2})$ ,  $(1s_e, 1S_{1/2})$ ,  $(1s_e, 2S_{1/2})$ ,  $(1p_e,$

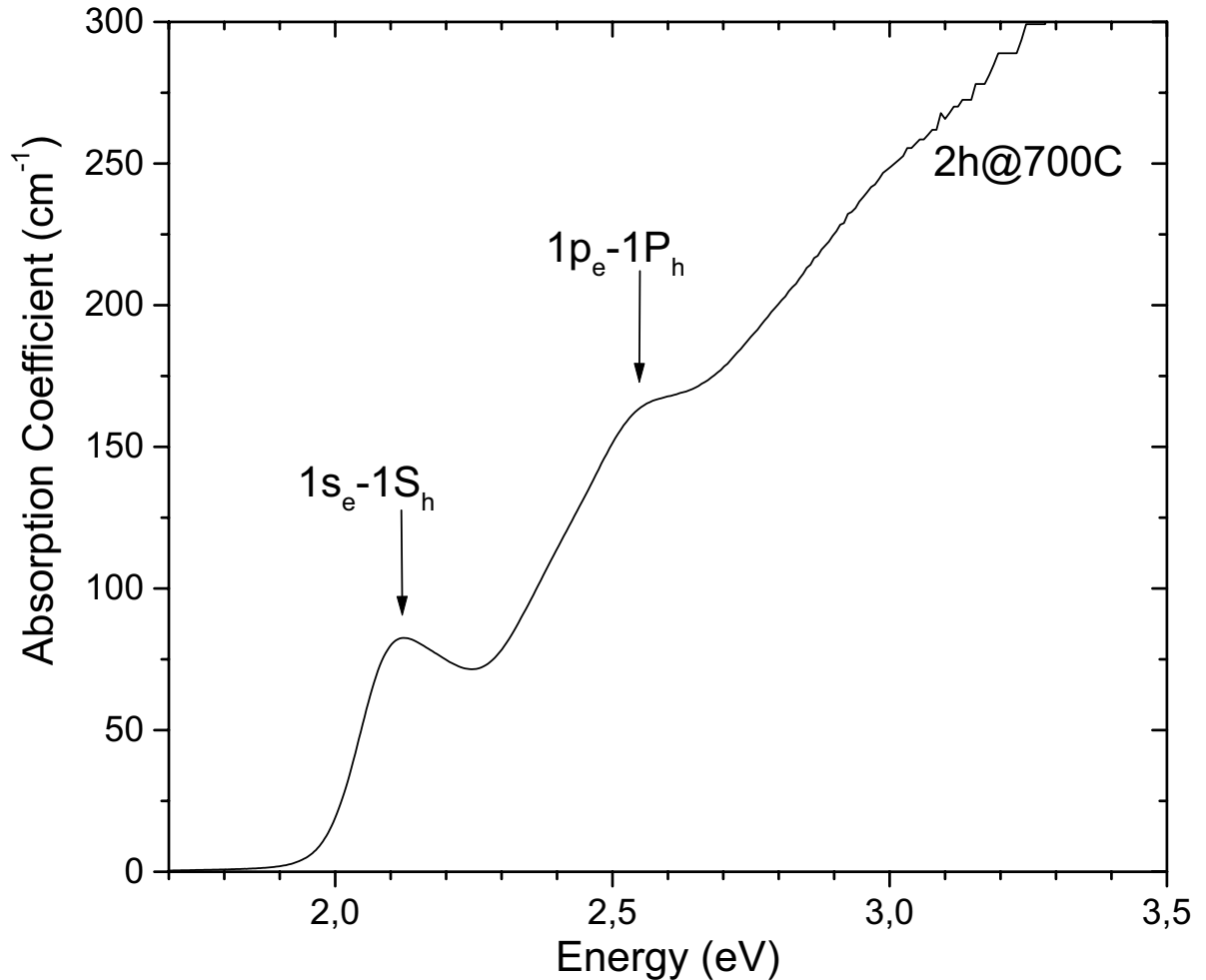


**Fig. 7.10:** Linear absorption spectra for 2.2 nm QDs included in the sample 2h@700C. The first peak corresponds to the lowest  $1S$  transition and the second peak to the  $1P$  transition, respectively. The excitation wavelengths of the incident laser pulses indicated by arrows are considered for each transition and sample separately.

$1P_{3/2}$ ) (see figure 2.6). The lowest transitions are involving the electron in its  $1s_e$  ground state, therefore the e-h pair relaxation times are mainly determined by the hole relaxation through its dense spectrum, even for high energy separation. Further, it will be focused on the transitions  $1S$  and  $1P$ , well-resolved in the linear absorption spectra of the sample  $2h@700C$  (figure 7.10).

The investigation technique, described in the chapters 4 and 5 involves three circularly polarized 80-fs pulses tuned to the absorption peak energy, indicated by arrows in the linear absorption spectra shown in figure 7.10. The phase matching condition of DFWM in the framework of transient grating is obeyed. The essential role of various polarization geometries has already been outlined in the previous chapters. In this section the two polarization geometries  $I^{++++}$  and  $I^{++--}$  were selected as relevant, so that the investigation technique focuses on the lifetime of e-h pairs situated on higher excited energy levels. By comparing excited- and ground state dynamics, it will be shown that Auger-like thermalization of carriers plays a decisive role in the electron-hole energy relaxation.

Time transients obtained by TI-FWM spectroscopy represent a direct measure of bright exciton lifetime. Moreover, a summation of the transients in  $I^{++++}$  and  $I^{++--}$  geometries also includes average relaxation rates of the spin states. By carefully choosing the excitation wavelength of the incident pulses to be in resonance with either  $1S$  or  $1P$  exciton state, both population dynamics in the lowest  $1S$  and in the first excited  $1P$  electron states can be investigated.

Figure 7.11 shows time transients recorded for the sample  $2h@700C$  in both ground  $1S$  and excited  $1P$  exciton states. More exactly, the sum  $S^+$  for the transients recorded under the two relevant polarization geometries  $I^{++++}$  and  $I^{++--}$  for these states is plotted.  $1P$  is the first optically allowed excited exciton state resolved in the linear absorption spectrum and it involves Coulomb interactions of the hole in  $1P_{3/2}$  with the electron in  $1p_e$  state.

The sample  $2h@700C$  contains small QDs of 2.2 nm in radius. Therefore, strong carrier-carrier interaction is expected. From the figure 7.11 it can be seen that the

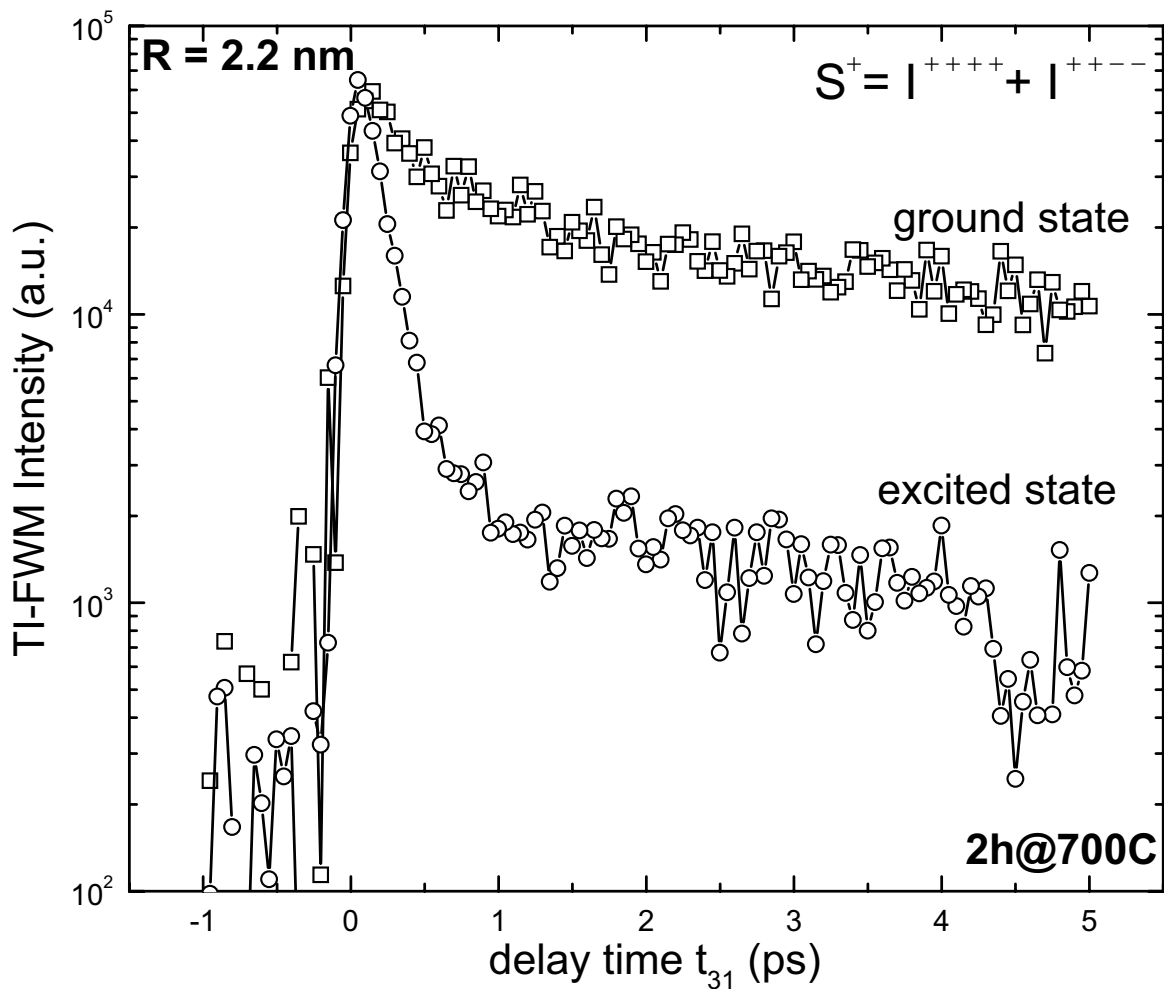


**Fig. 7.11:**  $S^+ = I^{++++} + I^{++--}$  recorded for 2.2 nm QDs included in the sample 2h@700C.  $S^+$  reflects the exciton lifetime in ground  $1S$  state (squares) and excited  $1P$  state (circles), respectively. The intensities of the two transients were normalized for clarity.

**Table 7.2:** Exciton Lifetime in CdSe QDs

R (nm)	Growth Time (h)	Growth Temp. (°C)	1S Exciton Lifetime (ps)		1P Ex- citon Lifetime (ps)		$\Delta$ (meV)
			$\tau_1$	$\tau_2$	$\tau_1$	$\tau_2$	
2.2	2	700	0.3	5.64	0.13	3.88	1.1

decay of the FWM signal intensity recorded for the excited  $1P$  state is much faster than its decay recorded for the ground state  $1S$ : the intensity of the TI-FWM signal for the  $1P$  state decreases almost two orders of magnitude for the time interval depicted in figure 7.11, whereas in the same interval the intensity of the TI-FWM signal recorded for the  $1S$  exciton decreases only 6 times. The most important optical and electronic properties, including exciton lifetimes and QD's symmetry characteristics are summarized in table 7.2.

Both  $1S$  and  $1P$  exciton states display a two-exponential decay behavior: first, a short but very fast decay of the exciton lifetime followed by a slow decay. The same behavior was observed for the "slow growth" sample  $8h@700C$  with QDs of 2.4 nm in radius. The behavior of the latter indicates the coexistence of two different kind of nanocrystals simultaneously excited by the laser pulses. Thus the capture of carriers into the dielectric matrix is mediated by two different type of traps. Furthermore, the interpretation is focused on the Auger mechanisms explaining the behavior of the excitons in the excited  $1P$  state.

The time transients depicted in figure 7.11 show an initial fast decay (in the first few hundred of fs) followed by a much slower decay which can be considered as a "background". It was shown that Auger processes play a decisive role in the relaxation of  $1P$  exciton into lower states [77, 81, 95, 96]. The observed fast dynamics

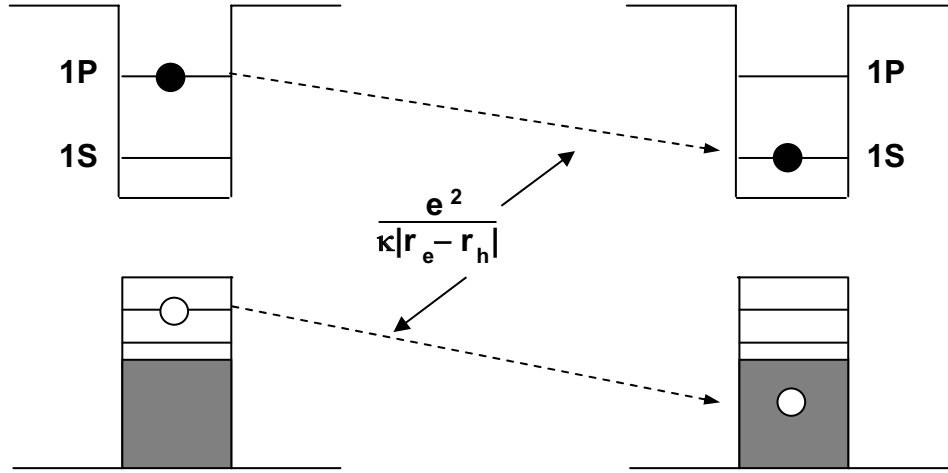


**Fig. 7.12:** Schematic illustration of the Auger-like thermalization of quantum confined carriers. Strong Coulomb interaction is responsible for energy transfer from the electron to the hole, which then relaxes rapidly through the almost continuous spectrum of its valence band states [97].

are best explained in terms of an Auger mechanism discussed in [93], which involves confinement-enhanced energy transfer of the electron excess energy to a hole. Subsequently, the hole relaxes relatively fast through its quasicontinuum of states.

The background-like decay observable in the transients shown in figure 7.11 for  $t_{31} > 300$  fs is due to formation of long lived ionized states by Auger-like carrier thermalization. It was shown [93] that Auger-like thermalization is a much faster process than the radiative recombination. A schematic representation of this process is given below (figure 7.12).

For the QDs discussed in this section, the energy spacing between the states  $1S$  and  $1P$  is on the order of  $300 - 500$  meV, which is significantly larger than the optical phonon energy ( $20 - 30$  meV). However, the strong Coulomb interaction between carriers in small QDs constrains the hole levels, so that the hole level spacing becomes an order of magnitude smaller than those of the electrons. This is a direct consequence of the greater hole effective mass ( $m_h/m_e \approx 6$ ) and the degeneracy of the valence band. As a result, the electron energy is transferred via

Coulomb interaction to the hole, which then relaxes very quickly through its much smaller split valence band states, a process known as Auger-like thermalization.

The exciton dynamics shown in figure 7.11 can be described as a multichannel relaxation of electrons and holes. The initial fast decay of the exciton lifetime can be attributed to an intraband relaxation mechanism of the electron. By optical excitation with the appropriate wavelength resonant with the  $1P$  transition (figure 7.10), the electron achieves the  $1P$  excited state, from where it first relaxes by Auger-like thermalization into lower lying states. This process is very fast and takes place on a sub ps scale (given by time constant  $\tau_1$  in table 7.2). This Auger-like thermalization from  $1P$  to energetically lower lying levels in 2.2 nm QDs in  $2h@700C$  was determined to lie in the range of 200 fs (decay of the sum  $S^+$  being 100 fs).

The strong electron-hole coupling influences the hole relaxation from its  $1P_{3/2}$  into lower energy states, which are easily achieved due to transitions between the dense energy states of the valence band. The "background"-like features in the transients are due to carrier trapping into long-living surface states, defects, and/or escaping into the dielectric matrix. Here, the Auger autoionization processes gain in importance and the relaxation process occurs as described in the previous section. After the hole was transferred into the matrix or deep surface traps, the relaxation time increases significantly and exceeds the ps barrier because the distance between the Coulomb interacting carriers drastically increases. It is worth to emphasize that even in a charge separated system the electron relaxes back into the ground state on a ps time scale, which is much faster than expected for phonon dominated relaxation [98].

It can be said with certainty that the electron-hole relaxation mechanisms involve strong Coulomb-interaction-mediated electron-hole energy transfer. Auger-like thermalization and autoionization play a decisive role in the relaxation process.

The contribution of other relaxation channels to the  $1P$  exciton lifetime can be ignored. The decay time of the FWM signal for  $1P$  excitons is markedly smaller than that for the  $1S$  states, which indicates that the direct recombination from the

optically active  $1P$  exciton states to the ground state is not the dominating channel. Moreover, taking a look at the background-like feature, which appears after the first 300 fs ( $t_{31} > 300$  fs), the intensity of this slowly decaying part of the TI-FWM signal is very low. Therefore the part of bright  $1P$  excitons converted into long lived dark  $1S$  exciton states ( $J=2$ ) is very small. This is in concordance with the very low quantum efficiency of the QD dark exciton emission by above band gap excitation [90].

In conclusion, the relaxation processes from higher lying exciton states were studied by means of three pulse DFWM spectroscopy in the framework of transient grating. It was shown, that the electron intraband dynamics depend strongly on the Coulomb interaction between electrons and holes. Even in the case of significant spatial separation between an electron and a hole, i.e. as result of trapping outside the nanocrystal into the dielectric matrix, the Coulomb interactions between carriers can be strong enough to provide an efficient channel for electron energy losses. This is a consequence of the fact that the Coulomb coupling does not require a direct overlap between the wave functions of electrons and holes, depending inversely proportional on the spatial separation between carriers. The relaxation from the energetically higher situated exciton state ( $1P_{3/2}, 1p_e$ ) occurs in two steps: a fast decay of the electron from its  $1p_e$  excited state into lower lying states (i.e. surface traps or escaping into the matrix), from where further relaxation into the lowest lying  $1s_e$  state occurs very slowly, giving rise to a "background"-like feature in the time transient. In the meantime, the hole relaxes first from its  $1P_{3/2}$  excited state into lower lying dense energy states into the valence band via Auger thermalization. This clearly indicates that electron relaxation in QDs is dominated by electron-hole interaction processes, but not electron-phonon interactions like in bulk semiconductors. The Coulomb forces acting between carriers are thus responsible for the breakdown of the phonon bottleneck in quantum confined nanocrystals.



## 8 Conclusions – Zusammenfassung

### 8.1 Conclusions

Although extensively investigated, the physics of quantum confinement is still not entirely understood. It is well known that the enhancement of electronic and optical properties of semiconductors is a direct consequence of spatial confinement of carriers in nanostructures. The strong dependence of the opto-electronic properties of confined ensembles on the experimental conditions makes it difficult to create for quantum confined systems a detailed description based on a rigorous theoretical model. Therefore further investigations are required.

This work focuses on a qualitative study of quasi-zero dimensional II-VI semiconductor nanostructures (quantum dots QDs). In particular, commercially available as-received and heat treated  $CdS_xSe_{1-x}$  QDs embedded in a dielectric matrix were investigated by means of linear and nonlinear spectroscopy techniques. Low wavenumber Raman in off-resonance scattering regime was applied in order to obtain key-properties of the nanocrystals, such as the QD's size and the distribution of the QD's size inside the inhomogeneous broadening. Moreover, by careful selection of the polarization geometries, different acoustic vibrational modes could be evidenced. Furthermore, nonlinear spectroscopy techniques like femtosecond four wave mixing (fs-FWM) and femtosecond pump-probe transmission (fs-PPT) were applied in order to determine intrinsic properties of the nanoparticles, like energy distribution, symmetry of the nanocrystals and ultrafast relaxation processes. The excitation of carriers was performed with circularly polarized femtosecond laser pulses, special

attention being paid to the non-phonon relaxation mechanisms.

Chapter 2 summarizes the basic properties of quantum confined systems. The electronic and optical properties of nanocrystals are illustrated using a theoretical model including simple approximations like the "particle in a box" and the "effective mass approximation". Due to quantum confinement and strong Coulomb interaction between the spatially confined electrons and holes, a redistribution of the energy levels of the nanocrystal into discrete atomic-like structure with well separated energy levels occurs. Therefore, one can expect the relaxation of the selection rules of the optical transitions between such atomic-like energy levels. This relaxation of the selection rules due to redistribution of the energy states in comparison to the bulk was extensively investigated in the following chapters.

Chapter 3 is dedicated to low wavenumber Raman studies on  $CdS_xSe_{1-x}$  QDs of different sizes enclosed in commercially available Schott filter glasses. The modifications in the energy distribution due to 3D quantum confinement lead to a large enhancement of the intensity of the acoustical vibrational modes. As shown in chapter 3, for nanocrystals only two acoustic vibrations are Raman active: spheroidal ( $l = 0$ ) and quadrupolar ( $l = 2$ ), which can be selectively excited using linearly polarized laser pulses. The experiments presented in this chapter are in good agreement with these predictions. The spheroidal  $l = 0$  vibrational modes being symmetric were observed only in the VV polarization geometry (incident beam vertically V polarized and scattered Raman signal vertically V analyzed – here vertical refers to the direction perpendicular to the scattering plane). The quadrupolar  $l = 2$  modes are depolarized and therefore they could be observed in both VV and HV polarization geometries (incident laser beam horizontally H polarized and scattered Raman signal vertically V analyzed). The low wavenumber Raman experiments were performed in off-resonant scattering regime, thus involving all particles inside the inhomogeneous distribution into the scattering process. The QD's size was determined using the dependence of the frequency of the acoustic vibrational mode on the diameter of the vibrating particle, whereas the QD's size distribution was

estimated from the normalized full width at the half of the maximum (FWHM) of the symmetric acoustic vibrational mode.

In order to study relaxation mechanisms, which in quantum confined systems occur on a ps time scale, ultrafast spectroscopy techniques using laser pulses in the fs range must be employed. The generation of femtosecond laser pulses used in both FWM and PPT experiments was achieved using the experimental setup described in chapter 5, whereas the theoretical background is presented in chapter 4. The experimental setup allows individual control of the polarization of all three laser pulses making multiple polarization geometries available for the experiment. The efficiency of three pulse FWM experiments consists in eliminating the inconvenience introduced by the two pulse FWM processes, where the pump  $k_2$  and probe  $k_3 = k_2$  are represented by the same beam  $k_2$ , thus making it impossible to achieve polarization geometries with opposite polarization of the pump  $k_2$  and the probe  $k_3 = k_2$  pulses. As it was shown, such polarization geometries are crucial for the investigations presented in this work.

Chapter 6 includes fs-FWM and fs-PPT measurements on  $CdS_{0.6}Se_{0.4}$  QDs of 9.1 nm in diameter, embedded in a glass matrix. For both FWM and PPT experiments circularly polarized femtosecond laser pulses were used. In this chapter it was shown that the relaxation of polarization selection rules depend strongly on the symmetry of the nanocrystals under discussion. The laser pulses excite nanoparticles belonging to the symmetry group  $C_2$  or lower, thus putting in evidence a hexagonal crystal shape of the QDs. It was shown that the appearance of weak time integrated FWM (TI-FWM) and differential transmission (DTS) signals in polarization geometries ( $I^{++--}$  and  $I^{+-}$ , respectively) forbidden according to the model of non-interacting oscillators cannot be explained taking into account only the orientational induced disorder. Such a disorder induced by the random orientation of the symmetry axes of the QDs ensemble leads indeed to the appearance of weak TI-FWM and DTS signals in forbidden polarization geometries and the observed relatively weak intensities of  $I^{++++}$ ,  $I^{++++}$  and  $I^{++--}$  signals are in good agreement with these predictions.

However, the strong  $I^{++--}$  and  $I^{+-}$  signals appearing in forbidden polarization geometries cannot be explained by taking into account only the orientational induced disorder and further consequences of the lowered QD's symmetry have to be considered.

Therefore, the reason for higher intensities of  $I^{++--}$  and  $I^{+-}$  as predicted by the orientational induced disorder was explained by a strong exciton–exciton exchange interaction between excitons belonging to the same QD. The Coulomb interaction between excitons contained in different dots is negligible due to the large separation between the nanoparticles. The appearance of TI-FWM and DTS signals for forbidden polarization geometries was explained in the framework of a four–level system. This includes the ground state, two exciton states with opposite polarizations and a singlet two–exciton state. Formation of biexcitons – exciton molecules – takes place due to the unavoidable approach of spatially confined excitons. Considering the absorption/refraction directly proportional to the population density created in an energy state having the same polarization as the exciting laser beam, the depolarization ratio for both TI-FWM and DTS can be calculated. In both cases a much higher depolarization ratio of the experimentally recorded TI-FWM and DTS spectra was observed, which was explained by the strong exciton–exciton coupling in quantum confined systems. The experimentally recorded TI-FWM and DTS signals prove the existence of biexciton structures and the validity of the four–level model.

The reason for the fast decay of  $I^{+++-}$  (by two orders of magnitude for  $t_{31} \approx 400$  fs) and for its qualitatively different behavior with respect to  $I^{++--}$ , both forbidden according to the non–interacting oscillators model, has its origin in the qualitatively different density gratings created by the first two time coincident pump pulses. The two time coincident pulses create the density grating and the third pulse is scattered on it, similarly to the Bragg diffraction. The polarization of these two pump pulses with wave vectors  $k_1$  and  $k_2$ , respectively is crucial for the formation of the density grating. For pulses having the same polarization, i.e.  $\sigma^+$ , an interference of the pump fields in the sample volume creates a population grating. In contrast, when

the grating is formed by two pulses having opposite polarizations, i.e.  $\sigma^+$  and  $\sigma^-$ , respectively, a polarization grating is created. The polarization vector executes a precession with a rate proportional to the splitting  $\Delta$  between the exciton levels, similar to a spin dephasing process. It has to be mentioned that the spin dephasing discussed here is not a "real spin dephasing" mechanism, but a process related to the exciton splitting, which is a measure of QD's asymmetry. Due to the fact that the scattering on the population grating results in a change of the direction of polarization from  $\sigma^+$  to  $\sigma^-$ , the spin dephasing effect explains the behavior of  $I^{++--}$  with respect to  $I^{++++}$  at early delay times. It is natural to suppose that after a while ( $t_{31} \approx 5$  ps) the whole ensemble is already spin dephased and thus the difference in the intensities of  $I^{++++}$  and  $I^{++--}$  at small delay times ( $t_{31} < 5$  ps) disappears and both signals decay with the same time constant, given by the population lifetime ( $\approx 160$  ps). Inverse proportionality between this dephasing time and the energy band offset allows one to draw conclusions related to the energy structure and symmetry of the nanocrystals.

Deviation from spherical symmetry is a decisive element which has to be taken into account for the characterization of quantum energy level structures. Lowering of the nanocrystal symmetry results in further splitting of the lowest optically active exciton spin doublet  $J = \pm 1$  into the states  $|X\rangle = \frac{|+1\rangle + |-1\rangle}{\sqrt{2}}$  and  $|Y\rangle = \frac{|+1\rangle - |-1\rangle}{\sqrt{2}}$  optically active in mutually orthogonal linear polarizations. A redistribution of the energy levels is a direct result of the lowering of the nanoparticles' symmetry, having significant influence on the nonlinear optical properties of quantum confined systems.

The efficiency of circularly polarized femtosecond FWM spectroscopy techniques was proved once more in the investigation of heat treated *CdSe* QDs embedded in a dielectric matrix. The role of non-phonon energy relaxation mechanisms in the exciton ground and excited state of the QDs ensemble was extensively studied. Moreover, the dependence of the crystal shape asymmetry on the particle size and on the growth conditions could be estimated. It was shown, that the most efficient

procedure to grow high quality nanocrystals is a longer heat treating at lower temperatures. In this case, the particles have more time to "nucleate" and to adopt a more "symmetric" shape.

In the last part of this work it was shown that the relaxation of excitons is a complex mechanism. The electron intraband dynamics depend strongly on the Coulomb interaction between electrons and holes. Even at low excitation density, the Auger processes cannot be ignored for early delay times of  $t_{31}$ . Auger autoionization of excitons followed by capture of carriers in surface states and deep traps outside the QDs in the dielectric matrix slow down the exciton relaxation process leading to an exciton lifetime ranging on a ps time scale. The relaxation of excitons from higher lying energy levels occurs also on two paths. At the beginning of the relaxation process ( $t_{31} < 400$  fs), Auger-like thermalization of carriers is responsible for relaxation of the electron from  $1p_e$  into its  $1s_e$  state, while the hole relaxes rapidly to its dense spectrum of states in the valence band. This process is immediately followed by capturing of carriers in deep traps, situated at the semiconductor-dielectric heterointerface. The traps are a consequence of the QD's asymmetry: the more and the deeper the traps, the higher the asymmetry of the nanocrystals (the band offset  $\Delta$  is larger).

This work presents a complete characterization of *CdSSe* QDs embedded in a glass matrix. The most important properties of the nanocrystals like QD's size and size distribution inside the inhomogeneous broadening were determined by means of low wavenumber Raman spectroscopy. In order to draw a full picture of these nanoparticles further complementary nonlinear spectroscopy techniques were used. Invaluable conclusions were available as a result of TI-FWM techniques applied in the framework of transient grating on 3D confined nanocrystals embedded in a glass matrix. The polarized the TI-FWM measurements were successfully performed on different QDs ensembles in order to determine symmetry properties and to describe the ultrafast relaxation mechanisms. This work brings additional contribution concerning the preparation of high symmetry QDs by presenting the effect of different

growth conditions on the QDs asymmetry, thus indicating a way for efficient manufacturing of nanocrystals.

## 8.2 Zusammenfassung

Trotz umfangreicher Nachforschungen ist die Physik des "Quantum Confinements" noch immer nicht völlig verstanden. Es ist zwar bekannt, dass räumlich eingeschränkte Ladungsträger in niederdimensionalen Halbleitern zur Verstärkung optischer und elektronischer Eigenschaften solcher Nanostrukturen beitragen. Die Entwicklung eines Modells, das solche räumlich eingeschränkten Ensembles detailliert beschreibt, hat sich wegen der starken Abhängigkeit der opto-elektronischen Eigenschaften von den experimentellen Randbedingungen als sehr aufwändig erwiesen. Die Entwicklung eines solchen theoretischen Modells erfordert weitere intensive Forschung.

Die vorliegende Arbeit beinhaltet eine qualitative Studie quasi-nulldimensionaler II-VI Halbleiter Nanostrukturen. Es wurden handelsübliche und wärmebehandelte  $CdS_xSe_{1-x}$  Quantenpunkte (QDs) mittels linearer und nicht-linearer Spektroskopie untersucht. Im Rahmen nicht-resonanter Raman Spektroskopie wurden Schlüsseigenschaften der QDs, wie z.B. der Durchmesser und die Größenverteilung, bestimmt. Außerdem wurden nicht-lineare Techniken, wie z.B. Femtosekunden Vier-Wellen-Mischung (Fs-VWM) und Femtosekunden-Pump-Probe-Transmission (Fs-PPT), eingesetzt, um Eigenschaften der QDs, wie z.B. Energieverteilung, Symmetrie der Nanokristalle und ultraschnelle Relaxationsmechanismen, zu untersuchen. Im Falle der Femtosekunden-Spektroskopiemessungen erfolgte die optische Anregung der Ladungsträger durch zirkular polarisierte Laserpulse, wobei besondere Aufmerksamkeit den Nicht-Phonon-Relaxationsmechanismen gewidmet wurde.

Im Kapitel 2 sind die Grundeigenschaften räumlich eingeschränkter Systeme zusammengefasst worden. Die optischen und elektronischen Eigenschaften der QDs sind unter Verwendung einfacher Modelle, wie z. B. "Teilchen im Kasten" oder "effektive Masse-Näherung" dargestellt. Die Bandstruktur räumlich eingeschränkter Systeme verändert sich wegen der starken Coulomb-Wechselwirkung zwischen den Ladungsträgern und führt zu einer atom-ähnlichen Anordnung der energetischen



Niveaus. Folglich ändern sich entsprechend die Auswahlregeln für Übergänge zwischen den diskreten Niveaus. Die Änderung der Polarisationsauswahlregeln und deren Ursache wird in den nächsten Kapiteln im Detail untersucht.

Kapitel 3 ist linearen optischen Studien an in einer Glasmatrix eingebetteten  $CdS_xSe_{1-x}$  Quantenpunkten verschiedener Größe gewidmet. Die Proben wurden von Schott GmbH in Mainz hergestellt und sind als sehr effiziente optische Filter bekannt. Die Anordnung der Energieniveaus in einer atom-ähnlichen Struktur hat die Verstärkung der Intensität akustischer Phononen zur Folge, welche im Bulk nicht nachgewiesen werden können. In Nanokristallen sind nur zwei Sorten akustischer Vibrationen Raman-aktiv: Die kugelsymmetrischen ( $l = 0$ ) und die quadrupolaren ( $l=2$ ) Vibrationen, die durch linear polarisierte Laserpulse selektiv angeregt werden können. Die in diesem Kapitel dargestellten Versuche stimmen sehr gut mit diesen Voraussagen überein. Die  $l = 0$  Vibrationen sind symmetrisch und deshalb sind sie nur in den VV Spektren erkennbar (VV Polarisationsgeometrie heißt, dass der anregende Laserstrahl senkrecht zu der Streuebene polarisiert ist und das gestreute Ramansignal auch senkrecht zur Streuebene analysiert wird). Die quadrupolaren  $l = 2$  Vibrationen sind depolarisiert und deshalb sind sie in beiden VV und HV Polarisationsgeometrien erkennbar (HV Polarisationsgeometrie heißt, dass der anregende Laserstrahl parallel zu der Streuebene polarisiert ist und das gestreute Ramansignal senkrecht dazu analysiert wird). Die Raman-Messungen wurden im "off"-resonanten Regime durchgeführt. Daher tragen alle QDs verschiedener Größen zu dem Streuprozess bei. Die Größe der QDs wurde durch Berücksichtigen der Abhängigkeit der Vibrationsfrequenz akustischer Phononen von dem Durchmesser des Nanokristalls berechnet. Die Größenverteilung der QDs ist aus dem normalisierten FWHM ("full width half maximum") der symmetrischen Vibration bestimmt worden.

Die Relaxationsprozesse in Quantenpunkten finden auf einer Pikosekundenskala statt. Deshalb sind ultraschnelle Spektroskopiemethoden mit Laserpulsen im Femtosekundenbereich notwendig, um genaue Informationen über die stattfindenden Prozesse zu erhalten. Die Femtosekundenlaserpulse (Fs-Laserpulse), die für die

VWM- und PPT-Messungen eingesetzt werden, wurden auf Basis der im Kapitel 4 dargestellten theoretischen Grundlagen mit Hilfe der im Kapitel 5 beschriebenen Fs-Anlage erzeugt. Die Vorteile des verwendeten experimentellen Aufbaus liegen in der individuellen Kontrolle der Polarisation aller vier Laserpulse, welche die Auswahl vielfacher Polarisationsgeometrien im Rahmen des Versuchs ermöglicht. Das Verwenden der Drei-Puls VWM-Geometrie gegenüber den Zwei-Puls VWM Experimenten ist vorteilhaft, da im Falle der Drei-Puls VWM die  $k_1$  und  $k_2$  Pump-pulse auch entgegengesetzt polarisiert werden können, wobei im Falle der Zwei-Puls VWM diese  $k_1$  und  $k_2$  Pump-pulse durch einen einzigen Laserpuls vertreten werden ( $k_1 = k_2$ ) und dadurch den Aufbau einer Polarisationsgeometrie mit entgegengesetzt polarisierten  $k_1$  und  $k_2$  Pulsen unmöglich gemacht wird. Eine solche Polarisationsgeometrie hat sich für die in dieser Arbeit geschilderten Untersuchungen von äußerster Wichtigkeit bewiesen.

Im Kapitel 6 wurden in einer Glasmatrix eingebettete  $CdS_{0.6}Se_{0.4}$  QDs von 9.1 nm Durchmesser mittels Fs-VWM- und Fs-PPT-Spektroskopie untersucht. In beiden Fällen wurden zirkular polarisierte Fs-Laserpulse eingesetzt. In diesem Kapitel ist gezeigt worden, dass die Auswahlregeln für die Polarisation sehr stark von der Symmetrie der Nanokristalle abhängig sind. Die Fs-Laserpulse regen in den VWM- und PPT-Versuchen Nanokristalle an, die der Symmetriegruppe  $C_{2v}$  oder niedriger angehören. Dadurch wird der Nachweis einer hexagonalen Struktur der Nanokristalle erbracht. Das Entstehen schwacher ZI-VWM- und DTS-Signale in den verbotenen Polarisationsgeometrien  $I^{+--+}$ ,  $I^{+++-}$  und  $I^{++-+}$  stimmt mit den theoretischen aufgrund von Orientierungsunordnung erwarteten Intensitäten gut überein. Im Gegensatz dazu konnte die gemessene schwache Intensität der  $I^{++--}$ - und  $I^{+-}$ -Signale durch die Orientierungsunordnung nicht erklärt werden.

Diese Diskrepanz zwischen den hohen gemessenen Intensitäten und den aufgrund der Orientierungsunordnung vorhergesagten eher niedrigen Intensitäten der  $I^{++--}$ - und  $I^{+-}$ -Signale wurde in der vorliegenden Arbeit durch die starken Wechselwirkungen zwischen Exzitonen, die sich in demselben QD befinden, erklärt. Um das

Entstehen der ZI-VWM- und DTS-Signale in verbotenen Polarisationsgeometrien zu klären, wurde das Modell des Vier-Niveau-Systems verwendet, bestehend aus einem Grundzustand, zwei entgegengesetzt polarisierten Exzitonenzuständen und einem Singlet-Zwei-Exzitonenzustand. Durch unvermeidliche Annäherung der räumlich eingeschränkten Exzitonen bilden sich Biexzitonen. Das Depolarisationsverhältnis der ZI-VWM- und DTS-Signale kann berechnet werden, indem man die Absorption/Brechung als direkt proportional zur Populationsdichte eines Zustands gleicher Polarisation wie der des Anregungslaserstrahls annimmt. In beiden Fällen der ZI-VWM- und DTS-Spektren ergab sich im Experiment ein viel höheres Depolarisationsgrundverhältnis als erwartet, was allein durch Orientierungsunordnung nicht erklärt werden konnte. Daraus konnte geschlossen werden, dass die Exziton-Exziton Kopplung in räumlich eingeschränkten Systemen eine sehr wichtige Rolle spielt. Die Existenz der Biexzitonstrukturen und die Gültigkeit des Vier-Niveau-Modells wurde durch die experimentellen ZI-VWM und DTS Spektren eindeutig nachgewiesen.

Als sehr interessant erwies sich der zeitliche Verlauf der  $I^{+++-}$  und  $I^{++--}$ -Signale, die laut dem Modell der nicht-wechselwirkenden Oszillatoren in verbotenen Polarisationsgeometrien aufgenommen worden sind. Während erstere schon nach  $t_{31} = 400$  fs um fast zwei Größenordnungen abgefallen ist, erreicht letztere bei diesen Verzögerungszeiten erst ihr Maximum. Dieses qualitativ unterschiedliche Verhalten beruht auf dem verschiedenen Ursprung der durch die Pumppulse erzeugten optischen Gitter. Der Ursprung des Gitters hängt vom Ursprung der angeregten Populationsdichte ab. Die ersten zwei zeitlich zusammentreffenden Pulse zeugen ein Dichtegitter und der zeitlich dritte Puls wird auf diesem Gitter gemäß der Bragg-Bedingung gestreut. Die Polarisation der ersten zwei so genannten Pumppulse, denen die Wellenvektoren  $k_1$  und  $k_2$  zugeordnet werden, ist für den Aufbau des Dichtegitters entscheidend. Durch Interferenz zweier Pumppulse derselben Polarisation (z. B.  $\sigma^+$ ) wird in der Probe ein Populationsgitter aufgebaut, wohingegen das durch Interferenz zweier entgegengesetzt polarisierter Pumppulse (z. B.  $\sigma^+$  und  $\sigma^-$ ) entstandene Gitter zu einer ganz anderen Art von Gittern gehört. Das zweite

ist ein Polarisationsgitter, das viel schneller als das Populationsgitter zerfällt. Der Polarisationsvektor eines solchen Polarisationsgitters führt eine Präzession um die Symmetrieachse herum aus, deren Rate proportional zu der Aufspaltung  $\Delta$  der untersten Exziton-niveaus ist. Diese Präzession des Polarisationsvektors ähnelt einem Spindephasierungsprozess. Es sei angemerkt, dass der Spindephasierungsprozess, der hier diskutiert wird, kein "echter Spindephasierungsmechanismus" ist, sondern ein Prozess, der mit der Exziton-aufspaltung zusammenhängt und ein Maß der Quantenpunktasymmetrie darstellt. Der Spindephasierungsprozess erklärt das unterschiedliche Verhalten der  $I^{++--}$  – gegenüber der  $I^{++++}$  – Intensität bei frühen Verfallszeiten  $t_{31}$ , da die Bragg–Streuung auf dem Populationsgitter durch Wechsel der Polarisationsrichtung von  $\sigma^+$  zu  $\sigma^-$  geschieht. Nach einiger Zeit ( $t_{31} \approx 5$  ps) kann angenommen werden, dass das Populationsgitter schon spindephasiert ist, und somit verschwindet der Unterschied zwischen den Intensitäten  $I^{++++}$  und  $I^{++--}$ . Nach dieser Spindephasierungszeit ( $t_{31} > 5$  ps), zerfallen beide  $I^{++++}$  und  $I^{++--}$  Signale mit der gleichen Zeitkonstante, die auf die Populationslebensdauer ( $\approx 160$  ps) hinweist. Aus der inversen Proportionalität zwischen der Spindephasierungszeit und dem Bandoffset ( $\Delta$ ) lässt sich auf die Energiestruktur und auf die Symmetrie der Nanokristalle schließen.

Abweichungen von der sphärischen Symmetrie sind entscheidende Faktoren, die bei der Charakterisierung der Struktur der Quantum-Energieniveaus unbedingt beachtet werden müssen. Gehört der Nanokristall zu  $C_{2v}$  oder zu einer niedrigeren Symmetriegruppe, spaltet sich das niedrigste optisch-aktive Exziton Spindublett  $J = \pm 1$  auf in zwei weitere Zustände ( $|X \rangle = \frac{|+1\rangle + |-1\rangle}{\sqrt{2}}$  und  $|Y \rangle = \frac{|+1\rangle - |-1\rangle}{\sqrt{2}}$ ), die in aufeinander orthogonalen linearen Polarisierungen der Laserpulse optisch aktiv sind. Daher hat die niedrige Quantenpunktsymmetrie eine direkte Auswirkung auf die Verteilung der Energieniveaus und folglich auf die nicht-linearen optischen Eigenschaften der Quantenpunkte.

Im Kapitel 7 hat sich die Effizienz der Methode der zirkular polarisierten Fs-VWM-Spektroskopie bei der Untersuchung von in einer Glasmatrix eingebetteten

wärmebehandelten *CdSe* Quantenpunkten noch einmal bestätigt. Hier wurde die Aufmerksamkeit auf Nicht-Phonon-Relaxationsmechanismen des Grund- und angeregten Zustands des Exzitons gerichtet. Außerdem konnte die Abhängigkeit der Kristallasymmetrie von der Nanopartikelgröße und von den Wachstumsbedingungen abgeschätzt werden. Es zeigte sich, dass qualitativ hochwertige Quantenpunkte am effizientesten durch lange Wachstumszeiten bei niedrigen Temperaturen hergestellt werden können. Dabei haben die Partikel während des Wachstums genügend Zeit für die "Nukleation" und können somit eine "symmetrischere" Form annehmen.

Im letzten Teil dieser Arbeit ist nachgewiesen worden, dass die Exzitonrelaxation ein komplexer Mechanismus ist. Die Intrabanddynamik der Elektronen hängt stark von den Coulomb-Wechselwirkungen zwischen den Ladungsträgern ab. Sogar bei niedriger Anregungsdichte und kurzen Verzögerungszeiten ( $t_{31} < 400$  fs) spielen die Auger Prozesse eine wichtige Rolle. Die Relaxationsprozesse der Exzitonen werden sowohl durch die Auger Selbstionisation, als auch durch den anschließenden Einfang der Ladungsträger in tiefen Fallen (die sich an der Quantenpunktoberfläche und/oder in der dielektrischen Matrix befinden) deutlich verlangsamt. Dadurch wird die Lebensdauer der Exzitonen deutlich verkürzt und liegt im Pikosekundenbereich. Die Relaxation der Exzitonen von höheren Energieniveaus in den Grundzustand erfolgt auch auf zwei Wegen: Am Anfang des Relaxationsprozesses ( $t_{31} \approx 200$  fs) ist Auger-Thermalisierung der Ladungsträger für die Relaxation des Elektrons von seinem angeregten  $1p_e$  Zustand auf sein niedrigeres  $1s_e$  Energieniveau verantwortlich. Währenddessen erfolgt die Relaxation des Lochs sehr schnell über sein dichtes Spektrum von Valenzbandzuständen. Diesem Prozess folgt unmittelbar der Einfang der Ladungsträger in tiefen Fallen, die sich an der Nanokristall-Glasmatrix-Grenzfläche befinden. Diese Fallen sind eine direkte Konsequenz der Asymmetrie des Nanokristalls: je zahlreicher und je tiefer die Fallen, desto höher ist die Asymmetrie des Kristalls (der Bandoffset  $\Delta$  ist größer).

Im Rahmen dieser Arbeit ist eine komplette Charakterisierung der in einer Glasmatrix eingebetteten *CdSSe*-Quantenpunkte gelungen. Die wichtigsten Eigen-

schaften, wie z.B. die Größe und die Größenverteilung der Quantenpunkte, sind durch polarisierte Raman-Messungen bestimmt worden. Um ein komplettes Bild über die Nanokristalle zu bekommen, sind weitere nicht-lineare Spektroskopiemethoden eingesetzt worden. Polarisierte ZI-VWM Spektroskopie wurde zur Untersuchung verschiedener Quantenpunktensembles erfolgreich eingesetzt und daraus sind wertvolle Informationen über die Symmetrie der Nanokristalle gewonnen worden. Weiterhin sind die Exzitonrelaxationsmechanismen beschrieben worden, die teilweise die Verstärkung der optischen nicht-linearen Eigenschaften durch "Quantum Confinement" und starke Coulomb-Wechselwirkungen zwischen den demselben QD zugeordneten Exzitonen erklären. Durch die Untersuchung der Auswirkung verschiedener Wachstumsbedingungen auf die Symmetrie der QDs stellt diese Arbeit einen ergänzenden Beitrag zu Herstellungsverfahren qualitativ hochwertiger Quantenpunkte dar.

# Bibliography

- [1] Al. L. Efros.  
*Phys. Rev. B*, **46**:7448, 1992.
- [2] Al. L. Efros and A. V. Rodina.  
*Phys. Rev. B*, **47**:10005, 1993.
- [3] M. Nirmal, D. J. Norris, M. Kuno, M. G. Bawendi, Al. L. Efros, and M. Rosen.  
*Phys. Rev. Lett.*, **75**:3728, 1995.
- [4] U. Woggon, F. Gindele, O. Wind, and C. Klingshirn.  
*Phys. Rev. B*, **54**:1507, 1996.
- [5] D. Gammon et al.  
*Phys. Rev. Lett.*, **76**:3005, 1996.
- [6] V. D. Kulakovskii, G. Bacher, R. Weigand, T. Kummell, A. Forchel, E. Borovitskaya, K. Leonardi, and D. Hommel.  
*Phys. Rev. Lett.*, **82**:1780, 1999.
- [7] D. Loss and D.P. DiVincenzo.  
*Phys. Rev. A*, **57**:120, 1998.
- [8] F. Gindele.  
*PhD Thesis*.  
PhD thesis, Universität Karlsruhe, 1995.
- [9] M. Rajalakshmi, T. Sakuntala, and A. K. Arora.  
*J. Phys.: Condens. Matter*, **9**:9745, 1997.

- [10] N. F. Borelli, D. W. Hall, H. J. Holland, and D. W. Smith.  
*J. Appl. Phys.*, **61**:5399, 1987.
- [11] T. Sekikawa, H. Yao, T. Hayashi, and T. Kobayashi.  
*Solid State Commun.*, **83**:969, 1997.
- [12] K. M. Choi and K. J. Shea.  
*J. Phys. Chem.*, **98**:3207, 1994.
- [13] O. Goede and D. Henning.  
Verbindungshalbleiter.  
pages 128–200. Akademische Verlagsgesellschaft, Leipzig.
- [14] A. P. Alivisatos, T. D. Harris, P. J. Carroll, M. L. Steigerwald, and L. E. Brus.  
*J. Chem. Phys.*, **90**:3463, 1989.
- [15] M. Gandais, M. Allais, and A. Ramos.  
Preprint obtained from Schott Company.
- [16] Al. L. Efros and Al. L. Efros.  
*Sov. Phys. Semicond.*, **16**:772, 1982.
- [17] Y. Kayanuma.  
*Phys. Rev. B*, **38**:9797, 1988.
- [18] Y. Kayanuma and H. Momiji.  
*Phys. Rev. B*, **41**:10261, 1990.
- [19] Y. Wang and N. Herron.  
*J. Phys. Chem.*, **91**:257, 1987.
- [20] Y. Wang and N. Herron.  
*J. Phys. Chem.*, **92**:4988, 1988.
- [21] Y. Wang and N. Herron.  
*Phys. Rev. B*, **42**:7253, 1990.
- [22] Y. Wang and N. Herron.



- J. Phys. Chem.*, **95**:525, 1991.
- [23] P. E. Lippens and M. Lannoo.  
*Phys. Rev. B*, **39**:10935, 1989.
- [24] P. E. Lippens and M. Lannoo.  
*Phys. Rev. B*, **41**:6079, 1990.
- [25] P. E. Lippens and M. Lannoo.  
*Semicond. Sci. Technol.*, **6**:A15, 1991.
- [26] Einevoll G. T.  
*Phys. Rev. B*, **45**:3410, 1992.
- [27] L. M. Ramaniah and S. V. Nair.  
*Phys. Rev. B*, **47**:7132, 1993.
- [28] U. Woggon.  
*Optical Properties of Semiconductor Quantum Dots*.  
Springer, 1996.
- [29] L. E. Brus.  
*J. Chem. Phys.*, **90**:2555, 1986.
- [30] Y. Z. Hu, M. Lindberg, and S. W. Koch.  
*Phys. Rev. B*, **64**:1713, 1990.
- [31] S. H. Park, R. A. Morgan, Y. Z. Hu, M. Lindenberg, S. W. Koch, and  
N. Peyghambarian.  
*J. Opt. Soc. Am.*, **7**:2097, 1990.
- [32] Y. Z. Hu, S. W. Koch, M. Lindberg, N. Peyghambarian, E. L. Pollock, and  
F. Abraham.  
*Phys. Rev. Lett.*, **64**:1805, 1990.
- [33] Al. L. Efros and A. V. Rodina.  
*Solid State Comm.*, **72**:645, 1989.

- [34] E. L. Pollock and S. W. Koch.  
*J. Chem. Phys.*, **94**:6766, 1991.
- [35] F. Henneberger, U. Woggon, J. Puls, and Ch. Spiegelberg.  
*Appl. Phys. B*, **46**:19, 1988.
- [36] L. Belleguie and L. Banyai.  
*Phys. Rev. B*, **44**:8785, 1991.
- [37] M. Ivanda, K. Babocsi, C. Dem, M. Schmitt, M. Montagna, and W. Kiefer.  
*Phys. Rev. B*, **67**:235329, 2003.
- [38] M. Montagna and R. Dusi.  
*Phys. Rev. B*, **52**:10080, 1995.
- [39] E. Duval.  
*Phys. Rev. B*, **46**:5795, 1992.
- [40] edited by M. Schulz and Landolt-Börnstein.  
*Semiconductors*, volume New Series, Volume 4.  
Springer, 1998.
- [41] R. Shuker and R. W. Gammon.  
*Phys. Rev. Lett.*, **25**:222, 1970.
- [42] M. Ivanda.  
*Phys. Rev. B*, **46**:14893, 1992.
- [43] G. Irmer, J. Monecke, P. Verma, G. Goerigk, and H. Herms.  
*J. Appl. Phys.*, **88**:1873, 2000.
- [44] J. L. Martin, A. Migus, G. A. Mourou, and A. H. Zewail.  
*Ultrafast Phenomena VIII*, volume Vol.55.  
Springer Ser. Chem. Phys.
- [45] P. F. Barbara, W. H. Knox, G. A. Mourou, and A. H. Zewail.  
*Ultrafast Phenomena IX*, volume 60.

- Springer Ser. Chem. Phys., 1995.
- [46] W. Kaiser.  
*Ultrashort Laser Pulses*, volume Topics Appl. Phys., Vol. 60.  
2nd edn. edition.
- [47] C. Rulliere.  
*Femtosecond Laser Pulses*.  
Springer Verlag, 1998.
- [48] J. Shah.  
*Ultrafast Spectroscopy of Semiconductors and Semiconductor Nanostructures*.  
Springer Verlag, 1996.
- [49] R. Fausto.  
*Semiconductor Science and Technology*, **13**:147, 1998.
- [50] W. M. Axt and T. Kuhn.  
*Rep. Progr. Phys.*, **67**:433, 2004.
- [51] Z. Haichao, L. Deng, J. Wen, R. Liao, T. Lai, and W. Lin.  
*Science in China A*, **44**:1340, 2001.
- [52] K. Komori, G. R. Hayes, B. Deveaud, X. L. Wang, M. Ogura, and M. Watanabe.  
*Physica Status Solidi A: Applied Research*, **190**:855, 2002.
- [53] M. C. Netti, C. Gadaleta, N. Del Fatti, and R. Tommasi.  
*Phys. Rev. B*, **60**:4902, 1999.
- [54] H. Haug and S. W. Koch.  
*Quantum Theory of the Optical and Electronic Properties of Semiconductors*.  
World Scientific, 1993.
- [55] R. P. Feynman.  
*Quantum Electrodynamics*.  
Benjamin Inc., 1961.

- [56] Y. Prior.  
*IEEE*, **QE**–**20**:37, 1984.
- [57] M-D. Levenson.  
*Introduction to Nonlinear Laser Spectroscopy*.  
Academic Press, 1982.
- [58] M. Weissbluth.  
*Photon–Atom Interactions*.  
Academic Press, 1989.
- [59] S. Mukamel.  
*Principles of Nonlinear Optical Spectroscopy*.  
Oxford University Press, 1995.
- [60] T. U. Siebert.  
*Four-wave-mixing Technics Applied to the Investigation of Non–Adiabatic Dynamics in Polyatomic Molecules*.  
PhD thesis, Universität Würzburg, 2002.  
Dissertation.
- [61] M. Schmitt.  
*Femtosekunden-zeitaufgelöste kohärente Vierwellenmisch-Spektroskopie zur zustandselektiven Untersuchung molekularer Dynamik einfacher Systeme*.  
PhD thesis, Universität Würzburg, 1998.  
Dissertation.
- [62] P. N. Butcher and D. Cotter.  
*The elements of nonlinear optics*.  
Cambridge University Press, 1990.
- [63] C. H. Brito-Cruz, J. P. Gordon, P. C. Becker, R. L. Fork, and C. V. Shank.  
*IEE J. Quant. Electr.*, **QE** **24**:261, 1988.
- [64] J.-P. Foing.

- 
- Etude d'un distribution de porteurs hors d'équilibre dans des puits quantiques en arseniure de gallium.*  
PhD thesis, Ecole Polytechnique, 1991.  
PhD Thesis.
- [65] J.-P. Likforman.  
*Saturation selective d'excitons et effets de coherence dans l'arseniure de gallium par spectroscopie femtoseconde.*  
PhD thesis, Ecole Polytechnique, 1994.  
PhD Thesis.
- [66] R. G. Brewer and R. L. Schoemaker.  
*Phys. Rev. A*, **6**:2001, 1972.
- [67] H. J. Eichler, P. Günter, and D. W. Pohl.  
*Laser-Induced Dynamic Gratings.*  
Springer Verlag, 1985.
- [68] M. Joffre, D. Hulin, A. Migus, A. Antonetti, C. Benoit a la Guillaume, N. Peyghambarian, and S. W. Koch.  
*Opt. Lett.*, **13**:2505, 1988.
- [69] E. T. J. Nibbering.  
*Femtosecond Optical Dynamics in Liquids.*  
PhD thesis, Groningen University, 1993.  
PhD Thesis.
- [70] R. Leonhardt, W. Holzappel, W. Zinth, and W. Kaiser.  
*Rev. Phys. Appl.*, **22**:1735, 1987.
- [71] J. C. Diels and W. Rudolph.  
*Ultrashort laser pulse phenomena.*  
Academic Press, 1996.
- [72] R. W. Boyd.
-

- Nonlinear Optics.*  
Academic Press, 1992.
- [73] T. Joo, M. A. Dugan, and A. C. Albrecht.  
*Chem. Phys. Lett.*, **177**:4, 1991.
- [74] J. A. Shirley, R. J. Hall, and A. C. Eckbreth.  
*Opt. Lett.*, **5**:380, 1980.
- [75] Y. Prior.  
*Appl. Opt.*, **19**:1741, 1980.
- [76] S. Maeda, T. Kamisuki, and Y. Adachi.  
*Advances in Non-Linear Spectroscopy.*  
j. Wiley & Sons, 1988.
- [77] Al. L. Efros, M. Rosen, M. Kuno, M. Nirmal, D. J. Norris, and M. Bawendi.  
*Phys. Rev. B*, **54**:4843, 1996.
- [78] Y. Z. Hu, R. Binder, S. W. Koch, S. T. Cundiff, H. Wang, and D. G. Steel.  
*Phys. Rev. B.*, **49**:14382, 1994.
- [79] H. Nickolaus, H.-J. Wunsche, and F. Henneberger.  
*Phys. Rev. Lett.*, **81**:2586, 1998.
- [80] H. Yukselici.  
*PhD Thesis.*  
PhD thesis, Rensselaer Polytechnic Institute, Troy, NY, 1996.
- [81] A. L. Efros, D. J. Lockwood, and L. Tsybeskov.  
*Semiconductor Nanocrystals, From Basic Principles to Applications.*  
Kluwer Academic/Plenum Publishers, 2003.
- [82] A. L. Barabasi and H. E. Stanley.  
*Fractal Concepts of Surface Growth.*  
Cambridge Univ. Press, 1995.

- [83] H. Yukselici, P. D. Persans, and T. M. Hayes.  
*Phys. Rev. B*, **52**:11763, 1995.
- [84] E. D. Jones, N. M. Stewart, and V. Thambipillai.  
*J. Cryst. Growth*, **96**:453, 1989.
- [85] D. M. Mittleman, R. W. Schoenlein, J. J. Shiang, V. L. Colvin, and A. P. Alivisatos C. V. Shank.  
*Phys. Rev. B*, **49**:14435, 1994.
- [86] P. Roussignol, D. Ricard, K. C. Rustagi, and C. Flytzanis.  
*Optics Communications*, **55**:143, 1985.
- [87] D. I. Chepic, Al. L. Efros, A. I. Ekimov, M. G. Ivanov, V. A. Kharchenko, I. A. Kudriavtsev, and T. V. Yazeva.  
*Journal of Luminescence*, **47**:113, 1990.
- [88] T. Flissikowski, A. Hundt, M. Lowisch, M. Rabe, and F. Henneberger.  
*Phys. Rev. Lett.*, **86**:3172, 2001.
- [89] T. Takagahara.  
*Phys. Rev. B*, **47**:4569, 1993.
- [90] B. Patton, W. Langbein, and U. Woggon.  
*Phys. Rev. B*, **68**:125316, 2003.
- [91] T. Inoshita and H. Sakaki.  
*Phys. Rev. B*, **46**:7260, 1992.
- [92] U. Bockelmann and T. Egler.  
*Phys. Rev. B*, **46**:15574, 1992.
- [93] Al. L. Efros, V. A. Kharchenko, and M. Rosen.  
*Solid State Comm.*, 93:281, 1995.
- [94] P. C. Sercel.  
*Phys. Rev. B*, **51**:14532, 1995.

- [95] V. I. Klimov and D. W. McBranch.  
*Phys. Rev. Lett.*, **80**:4028, 1998.
- [96] V. I. Klimov, A. A. Mikhailovsky, D. W. McBranch, C. A. Leatherdale, and  
M. G. Bawendi.  
*Phys. Rev. B.*, **61**:13349, 2000.
- [97] A. L. Efros.  
*Phonons in Semiconductor Nanostructures*.  
ed. J. P. Leburton, J. Pascual, C. Sotomayor Torres, 1993.
- [98] H. Benisty.  
*Phys. Rev. B*, **44**:10945, 1991.



## 9 Acknowledgements

In awareness that this work could not be accomplished without the help of many people, hereby I would like to express my gratitude to everybody who brought his contribution in a way or another to this thesis. Here I mean on first place scientific support, but as well the moral support, whose role and necessity is evident.

First of all, I would like to thank Prof. Dr. Dr. hc Wolfgang Kiefer for providing me with a very interesting theme for my thesis. He is an excellent tutor and I want to thank him for his support. His attitude of supporting and encouraging me and in the same time the freedom he offered me in the progress of my work were very motivating.

Special thanks to Dr. Michael Schmitt, who introduced me in the subject of my work. He was during my PhD studies always my central contact person, who provided me with excellent ideas concerning my research. Due to his professional competence and his cooperativeness, it was possible for me to gather a lot of experience concerning the spectroscopic techniques, which I applied in my investigations. Sincere thanks to Prof. Dr. Kulakovskii, without whom I couldn't have accomplished this work. He introduced me into the physics of miniaturized semiconductor structures by giving me valuable advice and instructions. His optimism and perseverance were impressive and also from this point of view I learnt very much from him. I would also like to thank Dr. Alex Filin for support and for helping me in continuing the ideas of Prof. Kulakovskii. His guidance allowed me to make rapid progress in my work. His professional skills helped me by finding solutions in numerous complicated experimental issues.

I would like to express my special thanks to Frau Ursula Müller for all her efforts in organizational aspects especially at the beginning of my PhD studies in Germany. Her continuous presence and her good-intentioned advice saved me many times from difficulties provided by lack of German language knowledge. I would like to express my gratitude towards Belinda Leimeister for technical assistance and unconditional help concerning the laser setup. For technical support I would like to thank Rainer Eck and Jürgen Zimmermann in the electronic workshop and Peter Lang, Ralf Kohrmann, Gerhard Bömmel, Wolfgang Liebler, Thomas Schreckling in the mechanics workshop, who provided me with high quality electronic and technical devices necessary for the experiments. To Peter Popp I would like to thank for the hints he gave me concerning computer specific problems. I would like to thank Melanie Grom for technical assistance and funny moments she provided with her way of always being in a good temper. RIP.

I would like to thank Dr. Thorsten Siebert for his efforts to introduce me in the "secrets" of femtosecond spectroscopy. I learned a lot from him and I want to thank him for the hints and the tricks he shared with me from his former experience. I would like to thank Raman Maksimenka for the relaxed atmosphere due to his presence in the lab. He made me laugh many times in difficult situations. I had a lot of fun by the discussions and double-meaning on various topics with Benjamin Dietzek. He will be probably be happy about the free place next to the telephone.

I would like to thank all my colleagues for the agreeable atmosphere at work. My special gratitude goes to Cristina Dem, who always believed in me and has always been a real friend of mine. Thanks her initiation I could go on the way to fulfil my dreams. I wish her and her whole family all the best. Further I would like to thank Nicolae Tarcea for being "the most duteous child in the world", to Adriana Szeghalmi for her care concerning my health and for the delicious meals she shared with me, to Niculina Peica for her "soul-Röntgen-eyes". I wish them all the best in their future.

I would like to thank my family, my mother who helped me - or at least she thought

---

she was helping -, my sisters Rita and Anamaria and their families for moral support. I would like to thank to a very close friend of mine, Mihaela Padurean for numerous and fructuous discussions on the subject "human psychology". Special thanks to Alina Toca and Romulus Matisan for their support, though so many kilometers which separate us. Many thanks go to my ex-hostel colleague Dana Hangan for unconditioned help and moral support.

I would like to thank Sonderforschungsbereich 410, subproject C3 "Raman Spectroscopy on II-VI Semiconductor Nanostructures" for financial support.

At last, but not the least, I would like to cordially thank to Dr. Oliver Sbanski. Without him and his support I wouldn't have been able to achieve all I have had achieved. He always supported and encouraged me, giving me faith and strength to continue, when things were going out of control. He obviously brought his contributions to improve my knowledge of German language by explaining language-finesses and making clear the real sense of word-plays. I want to thank him for his patience especially concerning car driving lessons. His care led to invaluable discussions with mostly constructive character. I thank the "chemistry" for making her presence palpable. Special thanks go also to his grandma, who is an excellent woman I respect from all my heart, to his parents Gerd and Ursula, his brothers Jörg and Thorsten and their families as well as his sister Anja. They are excellent people and they were like a real family for me.

*Würzburg, January 26, 2005*





# Curriculum Vitae

## Personal Data

Name	Krisztina Babocsi
Date/Place of birth	13.01.1978/ Tasnad
Family Status	single
Citizenship	romanian

---

## Education

08.2001–currently	Institution: Bayerische Julius Maximilians University of Wuerzburg, Department: Institute of Physical Chemistry Address: Am Hubland, D-97074 Wuerzburg, Germany. Anticipated ending: February 2005 Research topic: Femtosecond Spectroscopy on II-VI Semiconductor Nanostructures. Degree sought: PhD
10.2000-07.2001	Institution: Babes-Bolyai University Department: Faculty of Physics, Address: 1 Kogalniceanu, R-400084 Cluj Napoca, Romania Field: Solid State Physics Degree: MSc.
10.1996-07.2000	Institution: Babes-Bolyai University Department: Faculty of Physics, Address: 1 Kogalniceanu, R-400084 Cluj Napoca, Romania Field: Physics Degree: Bachelor of Physics
09.1992-06.1996	Institution: Theoretical High School, Address: Tasnad, Romania Speciality: Mathematics and Physics, Degree: High School Diploma

---

## Work experience

08.2001-currently	research associate at the physical chemistry department of University of Wuerzburg in the special research project SFB410; supervision and support of students;
04.2001-07.2001	<b>Socrates Fellowship</b> at the Vrije University, Amsterdam, the Netherlands
09.2000-03.2001	English and French teacher at the Primary and Secondary School Craidorolt, Romania

---

## Special Skills

Foreign Languages	Romanian – mother language Hungarian – mother language German – fluent in spoken and written English – fluent in spoken and written French – sure in spoken and written Spanish– basic knowledge Italian- basic knowledge
Computer knowledge	MS Office, different text- and graphic editing programs, Microcal Origin, basic knowledge of programming language C/C++.
Private Interests	foreign languages, foreign language literature, contact to other (foreign) cultures and civilizations the 7th art: cinema sports: society dances, swimming, rollerblading

January 26, 2005

